SAPIENZA
UNIVERSITÀ DI ROMA

PhD in Clinical/Experimental Neuroscience and Psychiatry

XXXVII cycle

Exploring the role of gut microbiota and ketogenic diet on glioma growth and tumor microenvironment

PhD student

Javeria Maqbool

Matricola 2028255

Supervisor
Prof. Cristina Limatola

Tutor
Dr. Maria Rosito

A.A. 2021-2024

Index

General overview of my thesis

Glioblastoma (GBM) stands as the most frequent and aggressive form of malignant primary tumor affecting the central nervous system (CNS). It is distinguished by its rapid growth, extreme invasiveness, molecular heterogeneity[1], limited therapeutic options, and overall poor prognosis. As per the 2021 World Health Organization (WHO) grading system, GBM is classified as a grade 4 glioma. This categorization highlights its highly aggressive nature and dire clinical outcomes. GBM tumors are thought to arise from cells of the astrocytic lineage, although their precise origins remain under debate. What makes GBM particularly lethal is its ability to grow rapidly and infiltrate surrounding brain tissue, rendering complete surgical resection a significant challenge, as tumor cells often extend beyond the visible tumor margins into healthy brain areas. This aggressive invasiveness significantly heightens the risk of recurrence, presenting a major challenge in effective management [2].

One of the hallmarks of GBM recurrence is the immunosuppressive tumor microenvironment. Tumor cells secrete diverse signaling molecules and chemokines that actively recruit innate immune cells, including macrophages and monocytes. These tumor-associated macrophages (TAMs), constituting up to 30% of the tumor mass, play a dual role in GBM progression. While they are essential to the immune response, their polarization into an anti-inflammatory phenotype favors tumor growth and suppresses host defense mechanisms. Notably, the presence of TAMs negatively correlates with patient survival [3]. Given this immunosuppressive landscape, the standard of care remains focused on surgical resection. The success of surgical interventions directly impacts patient outcomes, with the extent of tumor removal strongly associated with improved prognosis. However, the localization and size of the tumor bulk often complicate achieving complete resection [4]. The approach involving chemo-radiotherapy has significantly improved the outcome of the treatment and over the last three decades numerous diagnostic or predictive response biomarkers have been identified, still few patients survive beyond five years, suggesting the absolute need for radical innovation in the therapeutic field [1].

GBM's heterogeneity is one of its defining features (fig. 1), Tumor cells exhibit a wide range of genetic and phenotypic diversity, fueling its adaptability and resistance to conventional therapies. Evidence suggests that GBM may originate from a single multipotent progenitor cell, and among the diverse populations of tumor cells within GBM, cancer stem cells (CSCs) are particularly significant, as they play a crucial role in both tumor initiation and progression.

These CSCs possess the ability to self-renew and differentiate, driving tumor growth and contributing to its aggressive nature and resistance to therapy [5].

Recent studies have identified a subpopulation of GBM cells expressing neural progenitor cell markers such as Nestin, CD133, and CD163. These markers are linked to tumorigenic potential, further emphasizing their role in sustaining glioblastoma growth and invasion. This small but aggressive subset of glioblastoma stem cells (GSCs) possesses the unique capabilities of self-renewal and multipotency, driving tumor progression even in the face of treatment [6]. The pathogenic progression of GBM involves a complex interplay of genetic, epigenetic, and environmental factors. These disruptions lead to dysregulated cell division, immune evasion, angiogenesis, and parenchymal invasion. This cascade of events forms a supportive tumor microenvironment that fosters carcinogenesis and progression.

Moreover, GSCs have been implicated in shaping the tumor microenvironment by interacting with stromal cells and modifying their phenotype. This intricate cross-talk creates a niche conducive to tumor growth and resistance to therapy, presenting a significant challenge for researchers and clinicians alike [7]. GBM's ability to exploit its microenvironment, particularly through its interactions with GSCs and TAMs, underscores the need for therapies that target these interactions. Despite the progress made, the multifaceted nature of GBM demands a holistic approach that integrates surgical, pharmacological, and immunological strategies. Advances in understanding the tumor microenvironment and cancer stem cell biology provide promising avenues for developing innovative treatments that can ultimately improve patient outcomes.

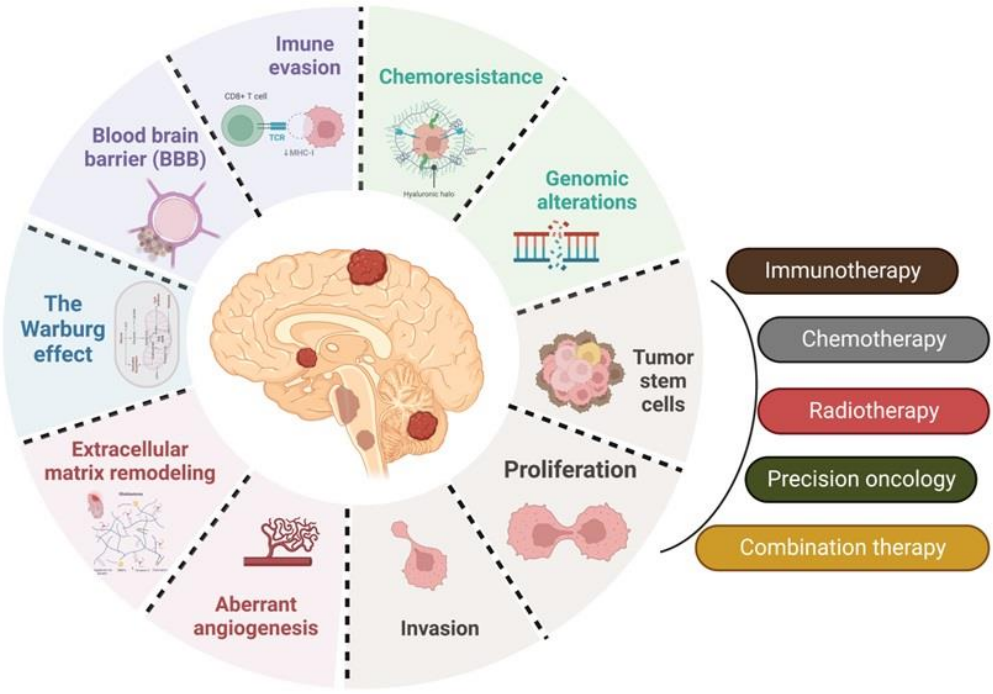

Figure 1: Characteristics of Glioblastoma and possible therapeutic options, S.S Yalamarty et al "Mechanisms of Resistance and Current Treatment Options for GlioblastomaMultiforme (GBM)" ***MDPI Cancers (2023).***

Recent research has revealed a compelling association between gut microbiota and the pathogenesis of GBM [8]. The human gut microbiota is a diverse ecosystem of microorganisms with a wide array of physiological roles, including immune modulation, nutrient metabolism, and signaling to distant organs like the brain. Dysbiosis an imbalance in the microbial composition has been implicated in numerous diseases, including GBM [9]. Dysbiosis occurs when the delicate balance of microbial communities is disrupted, often due to infections, delivery mode at birth, antibiotic (ABX) usage, dietary habits, environmental stressors, host genetics, and aging. Such disturbances can compromise the gut's ability to maintain homeostasis, thereby influencing disease susceptibility [10]. In recent years, significant attention has been given to the role of gut-derived metabolites in mediating communication between neuronal and glial cells under both physiological and pathological conditions. Although the exact metabolites that influence cerebral tumor growth remain unidentified, evidence suggests that gut dysbiosis may exacerbate glioma progression [11]. Notably, prior studies demonstrated that ABX-induced dysbiosis in glioma-bearing mice promotes tumor growth, alters the tumor microenvironment, and impairs the effector functions of natural killer (NK) cells, key players in anti-tumor immunity [3]. These findings highlight the potential of the gut-brain axis as a novel avenue for therapeutic intervention in GBM.

The emerging connections between gut microbiota, GBM pathogenesis, and glioma's unique metabolic dependencies present promising avenues for innovative therapeutic strategies. Dysbiosis-induced disruptions in the gut-brain axis highlight how systemic factors can influence glioma progression and immune responses, while the metabolic vulnerabilities of glioma cells offer an opportunity for targeted dietary interventions like the ketogenic diet (KD). Glioma cells are known for their unique metabolic reliance on glucose as a primary energy source, a phenomenon often referred to as the "Warburg effect." Unlike normal brain cells, which can metabolize alternative substrates like ketone bodies, glioma cells show a diminished ability to adapt to glucose restriction. This has spurred interest in dietary interventions such as carbohydrate-restricted KD as a potential therapeutic strategy [12]. KD is characterized by high fat and low carbohydrate content, designed to mimic the metabolic state of fasting, during which ketones become the predominant energy source [12]. Emerging evidence suggests that KD may inhibit glioma growth by inducing ketosis and increasing lipolysis, thereby depriving tumor cells of their preferred substrate while sparing normal brain cells [13]. Preclinical studies

have shown that KD can enhance the effectiveness of standard GBM therapies by inducing metabolic stress in tumor cells. Furthermore, KD has been associated with modulation of the tumor microenvironment, particularly through its impact on the activity of microglia and astrocytes [14]. This interplay between tumor metabolic reprogramming and the surrounding stromal cells may contribute to tumor progression or regression. While preliminary data support the potential benefits of KD in GBM treatment, further clinical studies are needed to validate its efficacy and safety. KD may offer multiple advantages, including enhancing patient survival, reducing tumor progression, and possibly improving quality of life when used alongside standard treatments such as surgery, radiation, and chemotherapy. It also represents a novel approach to targeting glioma metabolism without affecting healthy brain tissue.

In summary, gut microbiota and dietary interventions such as KD present promising areas for therapeutic innovation in GBM. However, more extensive research and clinical trials are necessary to elucidate the underlying mechanisms and establish these approaches as standard care options. The interplay between gut dysbiosis, metabolic reprogramming, and tumor microenvironment modulation underscores the complexity and potential of these strategies in improving GBM outcomes.

In my thesis, I discussed the dual impact of gut dysbiosis and dietary intervention on GBM progression and tumor microenvironment modulation. Specifically, In part 1 which is a published work of our group, I made substantial contributions to all the experiments of this work. Here I discussed the effects of dysbiosis induced by the administration of non-absorbable antibiotics on the metabolomic profile and tumor microenvironment in glioma-bearing mice. This work aimed to elucidate how alterations in gut microbiota influence brain tumor biology, with a focus on metabolic reprogramming and immune landscape changes within the tumor.

Additionally, In part 2 I studied the effects of a KD on tumor growth, tumor microenvironment, and survival rates in glioma-bearing mice. By analyzing the metabolic shifts associated with KD-induced ketosis, I aimed to assess its potential as an adjunct therapeutic strategy for glioma treatment. This comprehensive approach sheds light on the intricate interplay between gut microbiota, metabolism, and GBM progression, offering insights into novel avenues for therapeutic interventions.

Aims of the thesis

This thesis aims to investigate the intricate relationship between gut microbiota, dietary interventions, and their impact on GBM growth, tumor microenvironment, and glial cell cross-talk. Specifically, the research explores two distinct but interrelated approaches to understanding and potentially mitigating glioblastoma progression.

The first part of this work focuses on how dysbiosis, induced by the administration of non-absorbable antibiotics, influences glioblastoma progression. Key areas of investigation include the alterations in gut and brain metabolomic profiles resulting from dysbiosis, modulation of the tumor microenvironment, including glioma cell heterogeneity and tumor vascularization, and the role of dysbiosis-driven changes in metabolites in shaping glioma progression.

In light of the limited success of current glioblastoma treatments in significantly improving patient survival, novel therapeutic strategies are being explored. The second part of this thesis examines KD as a potential adjuvant therapy, with a focus on: The metabolic shift induced by KD, particularly the production of ketone bodies, such as β-hydroxybutyrate (β-HB), and their effects on glioma cells and the surrounding microenvironment, the role of glial cells as potential mediators of KD-induced changes in tumor growth and survival rates in glioma-bearing mice, Mechanistic insights into how β-HB and KD modulate glioma progression, with an emphasis on glial cell interactions and the tumor microenvironment.

By addressing these research areas, this thesis seeks to elucidate the roles of gut microbiota, dysbiosis, and dietary interventions in glioblastoma biology and provide novel perspectives on therapeutic strategies.

Author contributions

The research questions explored in this thesis have been addressed over the years, thanks to the valuable collaborators. To provide readers with a comprehensive understanding of the background and scope of these projects, certain experiments or analyses, not personally conducted by me, have been integrated into this thesis. To clarify my specific contribution, each section is accompanied by a dedicated paragraph titled "Personal Contribution to the Project." Within these sections, I aim to provide a concise summary of my involvement in the various aspects of the project

Part 1: Antibiotics treatment promotes vasculogenesis in the brain of glioma-bearing mice

Introduction

Recently, several studies demonstrated that the gut microbiota and microbiota-derived metabolites have a significant impact on brain function both in physiological and pathological conditions [15,16] (fig.2). The gut-brain axis, a bidirectional communication network between the gut microbiota and the central nervous system (CNS), plays a critical role in maintaining homeostasis, regulating immune responses, and modulating neurological processes [17].

Dysbiosis of gut microbiota in response to antibiotic treatment has been recently linked to pathological alteration of brain function moreover, a close relationship between the gut microbiome and microglial functions has been reported [18]. In the context of brain tumors, previous studies have shown that ABX-induced gut dysbiosis in glioma-bearing mice promotes tumor growth and progression. This phenomenon is mediated through multiple mechanisms, including the impairment of natural killer (NK) cells' effector functions, modulation of the gut-immune-brain axis, and alterations in microglial phenotype. These findings suggest that dysbiosis drives the development of a tumor-tolerant CNS microenvironment, favoring glioma growth and immune evasion [3]. The effects of ABX treatment are primarily mediated by the selective elimination of microbiota within the intestinal tract and the resulting disruption of microbiota-derived metabolites [19]. Notably, changes in the production of SCFAs, polyamines, and lipopolysaccharides (LPS) can profoundly impact systemic immune responses and CNS inflammation. For example, SCFAs have been shown to modulate T cell and microglial activity, whereas LPS can trigger pro-inflammatory cascades that facilitate tumor progression [20].

Given these findings, it becomes increasingly relevant to identify the signature molecules and pathways orchestrating the complex crosstalk between the enteric system, the brain, and brain tumors under normal conditions and during ABX administration. Understanding this interaction may provide novel insights into the development of microbiota-targeted therapeutic strategies to combat gliomas and modulate the tumor microenvironment.

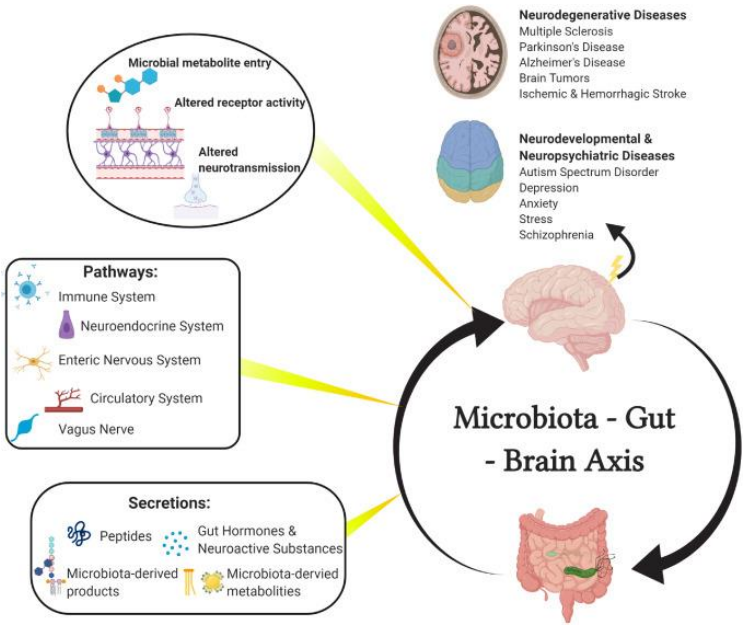

Figure 2: The microbiota-gut-brain axis, L.liu et al ; "Microbiota and the gut-brain-axis: Implications for new therapeutic design in the CNS" *eBioMedicine (2022).*

Recently, mass spectrometry-based metabolomics has emerged as a powerful tool for the identification and characterization of the diverse array of molecules produced by the human microbiota [21]. This approach has significantly advanced our understanding of microbiota-derived metabolites and their functional impact on human health. Microbe-derived factors such as bacterial structural proteins, molecules associated with microbes, short-chain fatty acids, and neurotransmitters play both local and systemic functions in various processes. These include the maintenance of the blood-brain barrier, gut epithelial integrity [22], activation and the maturation of microglia, regulation of the immune response and inflammation in different neurodegenerative diseases, and growth of brain tumors [23].

Microglia, the CNS resident macrophages constitute a prime partnership with the gut microbiota due to their immune nature and dynamic responsiveness to environmental signals [24]. These cells play an essential role in CNS homeostasis by executing multiple functions: maintaining neuronal homeostasis and synaptic plasticity through pruning of synapses and secretion of trophic factors, safeguarding CNS integrity by engulfing exogenous molecules, cellular debris, and apoptotic cells, defending against inflammatory insults by initiating and coordinating immune responses and influencing the pathogenic progression of various neurological disorders, including neurodegenerative diseases, neuroinflammation, and brain tumors [24,25]. Gut dysbiosis, characterized by an imbalance in microbial populations, has been shown to interfere with microglial functions. In healthy mice, microbial dysbiosis disrupts

microglial-synapse interactions, impairing neuronal connectivity and cognitive processes [26,15], Under pathological conditions, dysbiosis alters the cross-talk between microglia and astrocytes, which further exacerbates CNS inflammation and neuronal damage [27]. This demonstrates that gut-derived signals are crucial for preserving microglial homeostasis and functional integrity.

In the context of gliomas, the most common and aggressive primary brain tumors, microglia and tumor-associated macrophages (TAMs) constitute up to 30% of the glioma tumor mass [28]. Microglia within the glioma microenvironment secrete a range of factors, including matrix metalloproteinases (MMPs) and cytokines, which degrade the extracellular matrix, promote tumor cell motility, and suppress effective anti-tumor immune responses. microglia are highly sensitive to changes in the microenvironment and rapidly respond by releasing immune signaling molecules, including cytokines, chemokines, and reactive oxygen species (ROS). These signals not only contribute to glioma progression but also reshape the tumor microenvironment, creating a feedback loop that sustains tumor growth and immune evasion [29]. Understanding how gut microbiota-driven microglial alterations influence glioma pathogenesis may uncover novel therapeutic targets aimed at re-establishing immune homeostasis and impeding glioma progression.

As already mentioned, glioblastoma (GBM) and microglia engage in an intricate and dynamic exchange of molecular signals, mutually conditioning one another and shaping the tumor microenvironment. One well-characterized mediator of this tumor-microglia cross-talk is transforming growth factor-beta (TGF-β). GBM cells secrete TGF-β, which exerts potent chemo-attractive and immune-suppressive effects on tumor-associated microglia, facilitating their recruitment to the tumor site. Once recruited, microglia themselves become active contributors to this signaling network by releasing additional TGF-β1 and matrix metalloproteinase-9 (MMP-9). These factors enhance GBM cell migration and invasion, thereby promoting oncogenesis and tumor progression [30]. Moreover, microglia contribute to the creation of a pro-inflammatory microenvironment enriched with cytokines and chemokines, such as interleukin-1β (IL-1β) and tumor necrosis factor-alpha (TNF-α), which paradoxically aid in carcinogenesis by enhancing tumor cell proliferation, angiogenesis, and immune evasion. This inflammatory milieu creates a positive feedback loop that sustains tumor growth and reprograms microglia toward a tumor-supportive phenotype.

A striking example of the mutual interdependence between GBM and microglia is highlighted in the work of Arcuri et al., who demonstrated the role of interleukin-6 (IL-6) in shaping microglial behavior. GBM cells produce high levels of IL-6, which polarizes microglia toward an anti-inflammatory (M2-like) phenotype, effectively dampening their anti-tumor immune

functions. In response, these polarized microglia secrete additional IL-6, which further reinforces this immunosuppressive state. Notably, microglia-derived IL-6 upregulates the expression of MMP-2 in GBM cells, a key enzyme involved in extracellular matrix remodeling, tumor invasion, and metastasis [31].

Hallmarks of glioblastoma biology include high invasiveness of tumor cells and the presence of abundant and aberrant vasculature. In the context of brain tumors, glioma-associated macrophages (GAMs) establish close interactions with tumor cells, playing a pivotal role in tumor growth and progression (fig.3). In addition to exerting an immunosuppressive role, it has been reported that GAMs are actively involved in tumor angiogenesis processes [32]. Angiogenesis in glioblastoma is a complex and multifaceted process that involves several sophisticated biological mechanisms. One of the primary strategies relies on the proliferation and migration of endothelial cells from the host endothelium, which form new blood vessels to supply the growing tumor with oxygen and nutrients [33]. Another mechanism involves the mobilization and integration of endothelial progenitor cells (EPCs), which are recruited from the bone marrow and show elevated circulating levels in glioblastoma patients. Once mobilized, EPCs infiltrate the tumor mass, differentiate into endothelial cells, and secrete a range of angiogenic factors, promoting vascularization and further enhancing tumor growth [34]. In addition to these traditional angiogenesis mechanisms, glioma stem cells (GSCs) have emerged as critical contributors to the formation of tumor vasculature. GSCs, like neural stem cells, possess the ability to self-renew and differentiate into multiple cell lineages. Through their interaction with the vascular niche, GSCs can differentiate into endothelial-like tumor cells, directly contributing to the formation of the vascular network within the tumor microenvironment (TME) [35]. This ability to transdifferentiate enables GSCs to actively reshape the TME and sustain tumor growth, further complicating therapeutic approaches targeting glioblastoma vasculature.

The process of blood vessel formation in the glioblastoma TME occurs under unique and challenging conditions. Endothelial cells in the TME are exposed to a milieu of extracellular signals, including hypoxia, fluctuating blood flow, low pH, and tumor-derived growth factors and cytokines. These signals not only regulate endothelial cell behavior but also facilitate a bidirectional interaction between tumor cells and endothelial cells. Tumor cells release cytokines that recruit EPCs and induce their migration into the tumor mass, while endothelial cells secrete factors that enhance tumor cell adhesion, proliferation, and invasion. This reciprocal relationship reinforces the tumor's ability to grow, invade surrounding tissues, and metastasize [36]. The amount of circulating EPCs in the body is strongly correlated with cancer

progression, highlighting their pivotal role in tumor angiogenesis and as a potential biomarker for glioblastoma progression. Targeting the complex interplay between tumor cells, GSCs, GAMs, and endothelial cells in glioblastoma represents a promising avenue for disrupting the vascular support required for tumor growth and improving therapeutic outcomes.

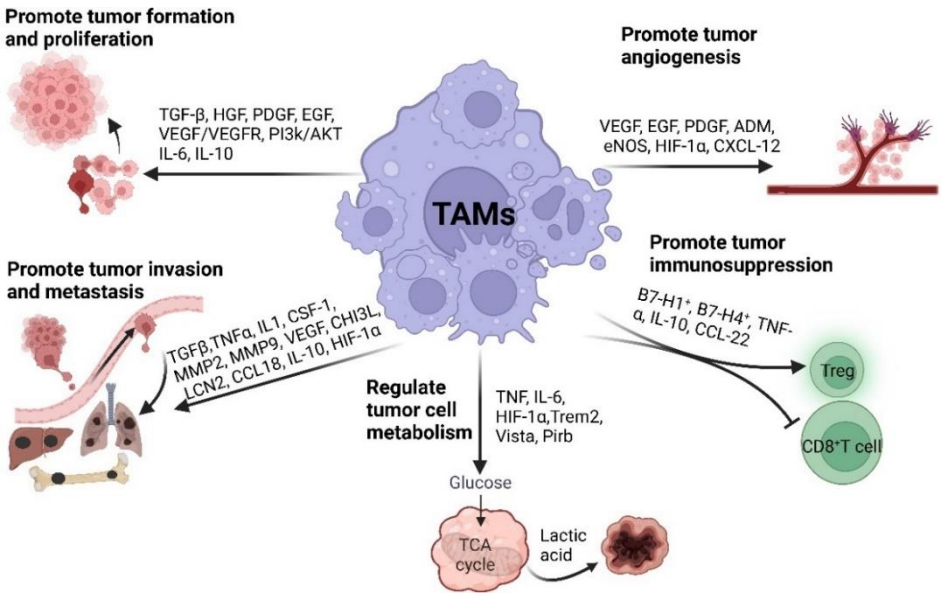

Figure 3: The roles of TAMs in tumor progression, Yuqian Li et al; 2The Roles and Targeting of Tumor-Associated Macrophages" *IMR Press (2023).*

In this study, that is already a published article [37] we demonstrated that chronic treatment with non-absorbable antibiotics significantly alters the behavior of GAMs in a syngeneic GL261 mouse model, thereby reshaping the tumor microenvironment. The treatment induced profound changes in the metabolomic profile of the brain, which were associated with enhanced tumor vascularization and an increased frequency of CD133+CD34+ cells within the tumor core. These CD133+CD34+ cells represent a subpopulation with stem-like properties and potential roles in promoting tumor progression and resistance mechanisms.

Among the metabolites modulated by ABX treatment, we identified glycine as a putative mediator of the observed phenotypic changes. Glycine appears to drive the pro-phagocytic and angiogenic activation of microglia, suggesting a reprogramming of GAMs toward a phenotype that supports tumor growth and vascular remodeling. Additionally, glycine was implicated in the trans-differentiation of tumor cells, fostering their shift toward a CD133+CD34+ phenotype, which is associated with enhanced stemness, invasiveness, and angiogenesis.

Our findings highlight a novel axis involving gut microbiota-derived metabolites and their influence on brain tumor biology, particularly through the modulation of immune cells and

tumor stem-like populations. These results suggest that targeting microbiota-driven metabolic pathways, such as glycine signaling, could represent a promising therapeutic approach to disrupt the tumor-promoting effects of ABX-induced dysbiosis and improve glioblastoma outcomes.

Results

ABX treatment affects GAMs phenotype and impairs ATP-induced response:

Gut dysbiosis may impact microglia function [26] and tumor growth [3]. To investigate how gut dysbiosis affects microglial cells in the context of glioma, mice were treated with two not orally absorbable ABX (Vancomycine and Gentamycine) for 2 weeks and then brain transplanted with GL261 glioma cells (GM). Three weeks later, upon continuous ABX administration, $CD11b^+$ cells (microglia) were isolated from the ipsilateral tumoral hemisphere and analyzed for gene expression by RT-PCR. ABX treatment increases the expression of the pro-angiogenic genes VEGFa and MMP9 and of the phagocytic marker CD68 (Fig. 4A) while reducing the expression of genes involved in inflammation (IL1b, TNFa, Arg1, and CD206) (Fig. 4B, C). The increased expression of CD68 was also confirmed by confocal immunofluorescence staining in ABX-treated GL261-bearing $Cx3cr1^{+/gfp}$ mice (Fig. 4D, E).

To further investigate the effect of ABX treatment on microglia function, we analyzed microglia patrolling activity in the peritumoral area in response to a focal ATP source [38] (Fig.4F). Microglial ability to extend processes towards ATP was assessed by time-lapse acquisition in GM and GM/ABX brain slices from $Cx3cr1^{+/gfp}$ mice. With this procedure, we visualized the displacement of microglia processes towards the ATP source through increased fluorescence around the tip of the ATP-releasing pipet. Data shown in Fig.4G demonstrate that ABX treatment reduces the speed of process movement toward ATP, indicative of an ABX-dependent impairment of microglial function as previously observed in mice treated with ABX[18],

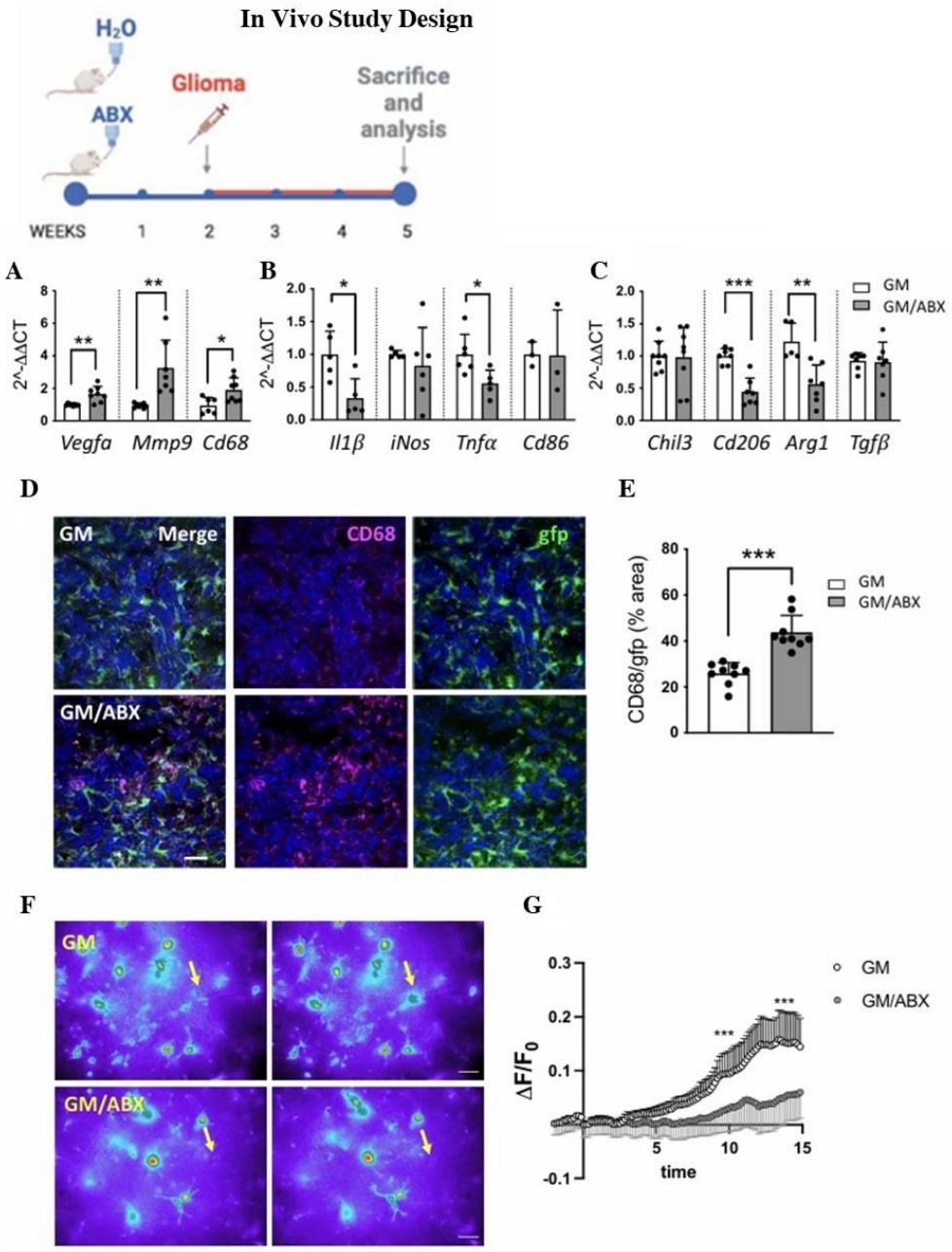

Figure 4: (A) RT-qPCR from CD11b^{+} cells isolated from GM and GM/ABX tumoral hemisphere reveals expression of pro-angiogenic genes; **(B)** pro-inflammatory genes and **(C)** anti-inflammatory genes. Gene expression is normalized to the housekeeping gene Gapdh. Data are presented as the mean ± SD $n = 3–8$ mice pulled from 3 independent experiments. ***$p < 0.001$; **$p < 0.01$; *$p < 0.05$, Student's t test. **(D)** Representative z-projection confocal images of microglia/macrophages cells in the tumoral core area from GM and GM/ABX Cx3cr1$^{+/gfp}$ mice (green) and CD68 (magenta). Hoechst staining (blu) for nuclei visualization. 60x objective (Scale bar: 25 μm). **(E)** Scatter dot plots showing quantification of CD68/gfp signals (from Cx3cr1$^{+/gfp}$ mice) expressed as the percentual area occupied in GM ($n = 33/9/3$ FOV/slices/mice) and GM/ABX ($n = 38/9/3$ FOV/slices/mice) mice versus total field of view (FOV). Data are presented as the mean ± SD ***$p < 0.001$, Student's t test. **(F)** Representative fields of GFP fluorescence measurements in slices from GM and GM/ABX Cx3cr1$^{+/gfp}$ mice

at minute 0 (left) and after 15 min (right) of ATP. The arrows refer to the tip of the puff pipette. After 5 min of basal motility recordings, ATP is applied for 15 min (Mg-ATP 2 mM, 8 psi, 100 ms). Note the fluorescence increase in the area around the pipette tip only in control slices. Scale bar: 10 µm. **(G)** Time course of fluorescence ratio signal ($\Delta F/F0$) measured in an ROI of 10 µm radius, centered on the tip of the ATP-containing pipette, from slices of GM and GM/ABX-treated Cx3cr1$^{+/gfp}$ mice. (GM $n = 8/4$ fields/mice GM/ABX $n = 11/4$ fields/mice; Data are presented as the mean ± SD ***$p < 0.001$, Mann–Whitney test at minutes 10 and 15).

According to our previous results [3], we validated the impact on glioma growth, thus confirming a significant increase of tumor volume in GM/ABX treated mice in comparison with GM mice (GM 9.57 ± 6,7, GM/ABX 16.74 ± 9,4 mm^3 *p=0.031) (Fig. 5A) and confirmed an increased tumor volume upon ABX treatment also in Cx3cr1$^{+/gfp}$ mice (GM 5.48 ± 3.0, GM/ABX 8.79 ± 3.7 mm^3 *p=0.025) (Fig. 5B). We also confirmed that there are no differences in the frequency of microglia (CD45$^+$CD11b$^+$TMEM119$^+$) between the tumor-bearing hemisphere of control and ABX-treated mice (Fig. 5C).

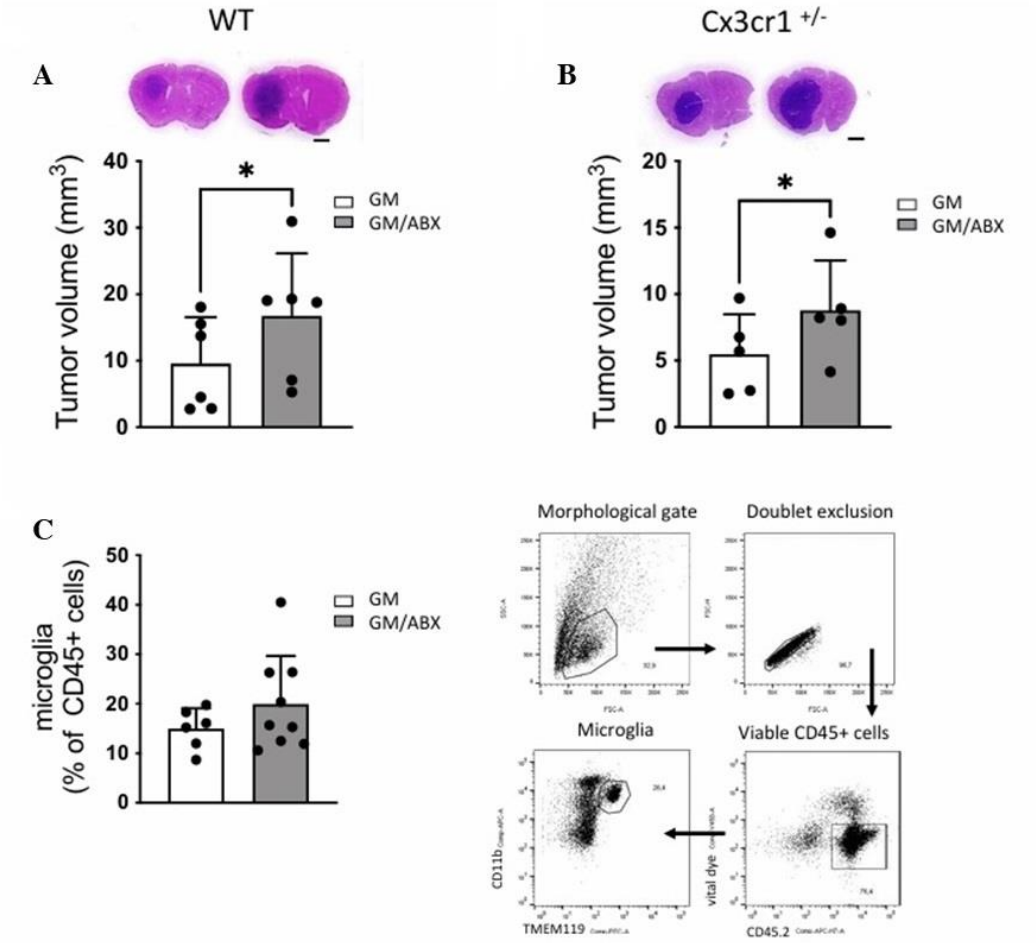

Figure 5: (A) Tumor size in GM and GM/ABX WT mice, $n = 6$, pooled from two experiments, three animals per group. Data are presented as the mean ± SD *p <0.05, Student's t-test. Upper pictures: Representative images of brain coronal slices, scale bar = 1 mm. **(B)** Tumor size in GM and GM/ABX mice, n = 5 animals per group. Data are presented as the mean ± SD *p <0.05, Student's t-test. Upper pictures: Representative images of brain coronal slices, scale bar = 1 mm **(C)** Left panel: Flow cytometry quantification of microglia identified as $CD45^+CD11b^+TMEM119^+$cells in GM and GM/ABX tumoral hemisphere. n=5 mice per group. Data are presented as the mean ± SD. Right panel: Representative gating strategy used to identify microglia by flow cytometry in brain-processed samples. First, debris was gated out in the FSC (forward scatter) versus SSC (side scatter) plot; then, singlets, live and $CD45^+$ cells were considered; microglia was defined as $CD45^+$ $CD11b^+$ $TMEM119^+$ and shown as a percentage among $CD45^+$ cells. Numbers in the plots indicate the percentage of gated cells in respect to parent cells.

ABX-induced dysbiosis enhances glioma vasculogenesis:

Since in our experimental condition, ABX treatment induced a pro-angiogenic and tissue remodeling phenotype in CD11b+ cells, we analyzed the effect of ABX on glioma vascularization.

At this aim we characterized the expression of $CD34^+$ in GL261-bearing mice; this endothelial marker plays a pivotal role in the development of glioma and influences tumor progression[39] Immunofluorescence staining revealed that ABX-treated mice exhibit higher reactivity for CD34 in the tumoral hemisphere (Fig. 6A, B top) and increased expression of $CD34^+$ vessel-like structures compared to control mice (GM 78.05 ± 33; GM/ABX 116.4 ± 53, number of structure/FOV; **p=0.0071) (Fig. 6B bottom) thus suggesting increased vasculogenesis. Double immunofluorescence staining revealed that the $CD34^+$ vessel-like structures are also positive for the endothelial marker CD31 (Fig. 6C). ABX-treated mice exhibit an increased signal density for CD31 (Fig. 6D, left), and an increased number of $CD31^+$ vascular structures (GM/ABX 5.4 ± 2.0, GM 3.7 ± 1.9 number of structure/FOV; $*p = 0.05$) (Fig. 6D, right).

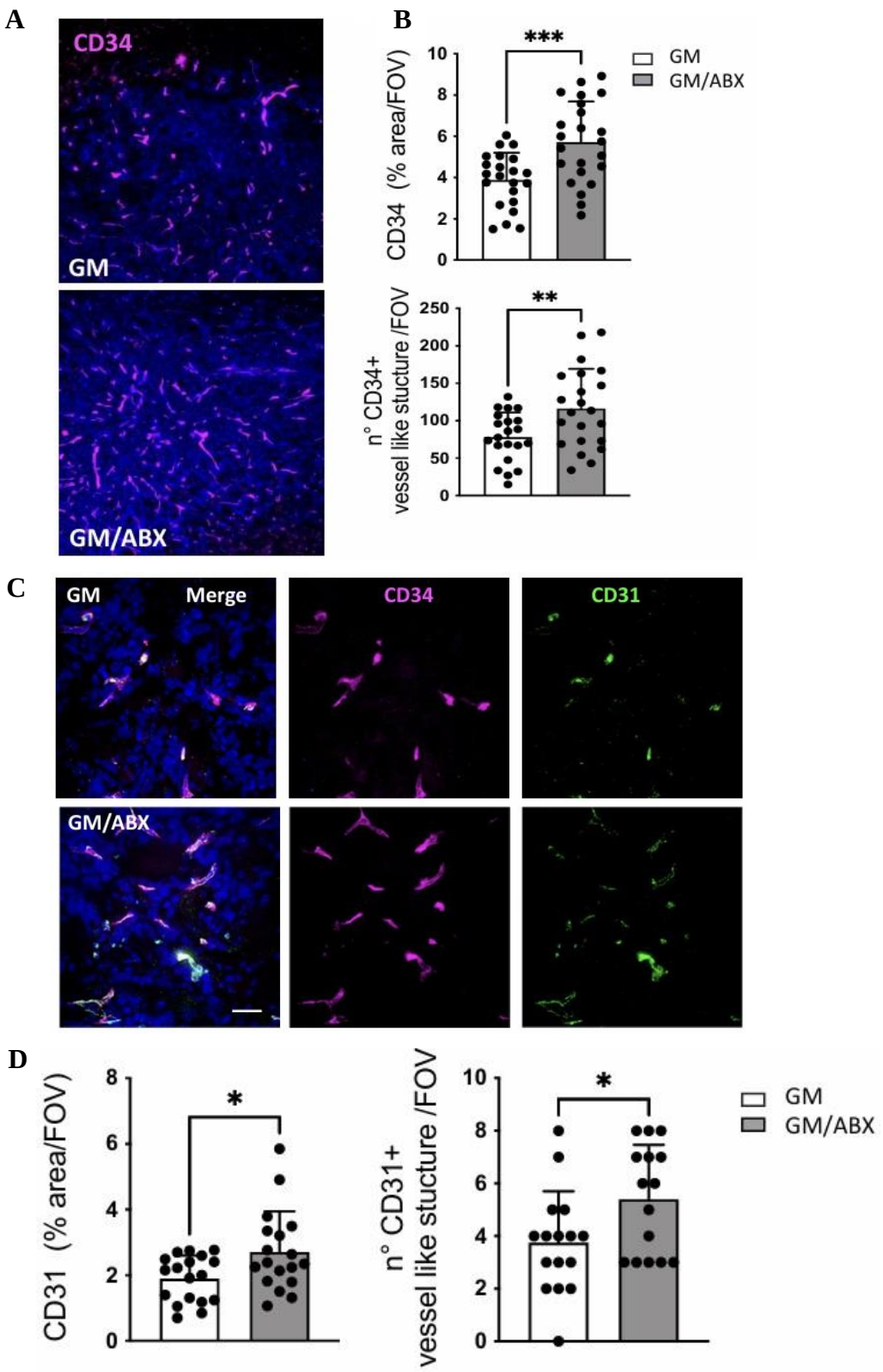
A
CD34
GM
GM/ABX
B
***
GM
GM/ABX
CD34 (% area/FOV)
10
8
6
4
2
0
**
n° CD34+
vessel like stucture /FOV
250
200
150
100
50
0
C
GM
Merge
CD34
CD31
GM/ABX
D
*
CD31 (% area/FOV)
8
6
4
2
0
*
n° CD31+
vessel like stucture /FOV
10
8
6
4
2
0
GM
GM/ABX

Figure 6: (A) Representative z-projection confocal images of CD34 (magenta) in GM and GM/ABX tumor core area. Hoechst staining (blu) for nuclei visualization Scale bar: 50 μm. (**B)** Scatter dot plots showing quantification of CD34 signal expressed as the percentual area occupied by fluorescent CD34 staining in GM ($n = 22/5$ slices/mice) and GM/ABX ($n = 23/5$ slices/mice) mice versus total FOV (top) and number of $CD34^+$ vessel-like structure versus total field of view (bottom) GM ($n = 22/5$ slices/mice) and GM/ABX ($n = 23/5$ slices/mice). Data are presented as the mean ± SD $***p < 0.001$; $**p < 0.01$, Student's *t* test. (**C)** Representative z-projection confocal images of CD34 (magenta) and CD31 (green) colocalization in GM and GM/ABX tumor core area. Hoechst staining (blu) for nuclei visualization Scale bar: 20 μm. (**D)** Scatter dot plots showing quantification of CD31 signal expressed as the percentual area occupied by fluorescent CD34 staining in GM ($n = 18/3$ slices/mice) and GM/ABX ($n = 18/3$ slices/mice) mice versus total field of view (left) and number of $CD31^+$ vessel-like structure versus total field of view (GM $n = 18/3$ slices/mice; GM/ABX $n = 15/3$ slices/mice) (right). Data are presented as the mean ± SD $*p < 0.05$, Student's *t* test.

Similar results were obtained with mice transplanted with a different glioma cell line, CT-2A; also in this syngeneic murine glioma model, ABX treatment induced an increase in tumor volume (GM 49.6 ± 11.7, GM/ABX 62.5 ± 8.8 mm^3; *p=0.033) (Fig. 7A) and increased tumor vasculogenesis compared to vehicle-treated mice (GM 6.88 ± 1.6, GM/ABX 8.125 ± 1.4 % of area/FOV; *p=0.03) (Fig. 7B, C).

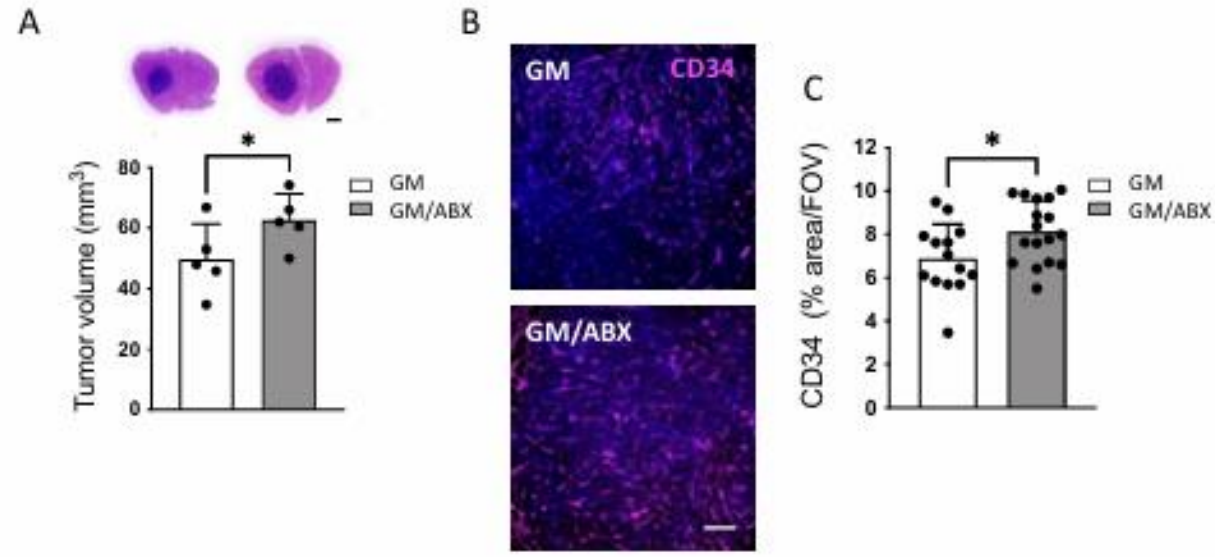

Figure 7: (A) Tumor size in GM and GM/ABX mice (CT-2A cell line), n = 5 animals per group, pooled from two experiments. Data are presented as the mean ± SD *p <0.05, Student's t-test. Upper pictures: Representative images of brain coronal slices, scale bar = 1 mm. **(B)** Representative z-projection confocal images of CD34 (magenta) in GM and

GM/ABX tumor core area. Hoechst staining (blu) for nuclei visualization; scale bar: 50 µm. **(C)** Scatter dot plots showing quantification of CD34 signal expressed as the percentual area occupied by fluorescent CD34 staining in GM (n= 14/3 slices/mice) and GM/ABX (n= 17/3 slices/mice) mice versus total field of view (FOV). Data are presented as the mean ± SD * p <0.05, Student's t-test.

ABX treatment increases the expression of the CD34 endothelial marker on glioma cells:

Several mechanisms have been described to drive the process of vasculogenesis in glioma[40] : both GSCs or cells of hematopoietic origin display the ability to undergo endothelial cell differentiation [41]. We therefore investigated the effect of ABX administration on the expression of CD133 marker in the mice tumor-bearing hemisphere. The quantification of $CD133^+$ cells revealed that GM/ABX mice exhibit a higher number of GSCs in the tumoral core (Fig. 8A, B) (GM 18.67 ± 7.2, GM/ABX 24.24 ± 7.1 cells $x10^3$ /mm^3; *p=0.028). Double immunofluorescence staining shows that the $CD133^+$ cells exhibit an endothelial differentiation profile as revealed by the co-expression of the CD34 endothelial marker (Fig. 8A); and that GM/ABX mice display a higher number of $CD133^+CD34^+$ cells compared to GM mice (Fig. 8C) (GM 13.41 ± 7.7, GM/ABX 19.57 ± 6.8 cells $x10^3$ /mm^3; *p=0.014). These results suggest that ABX treatment increases the abundance of the $CD133^+CD34^+$ cells population in the tumoral area.

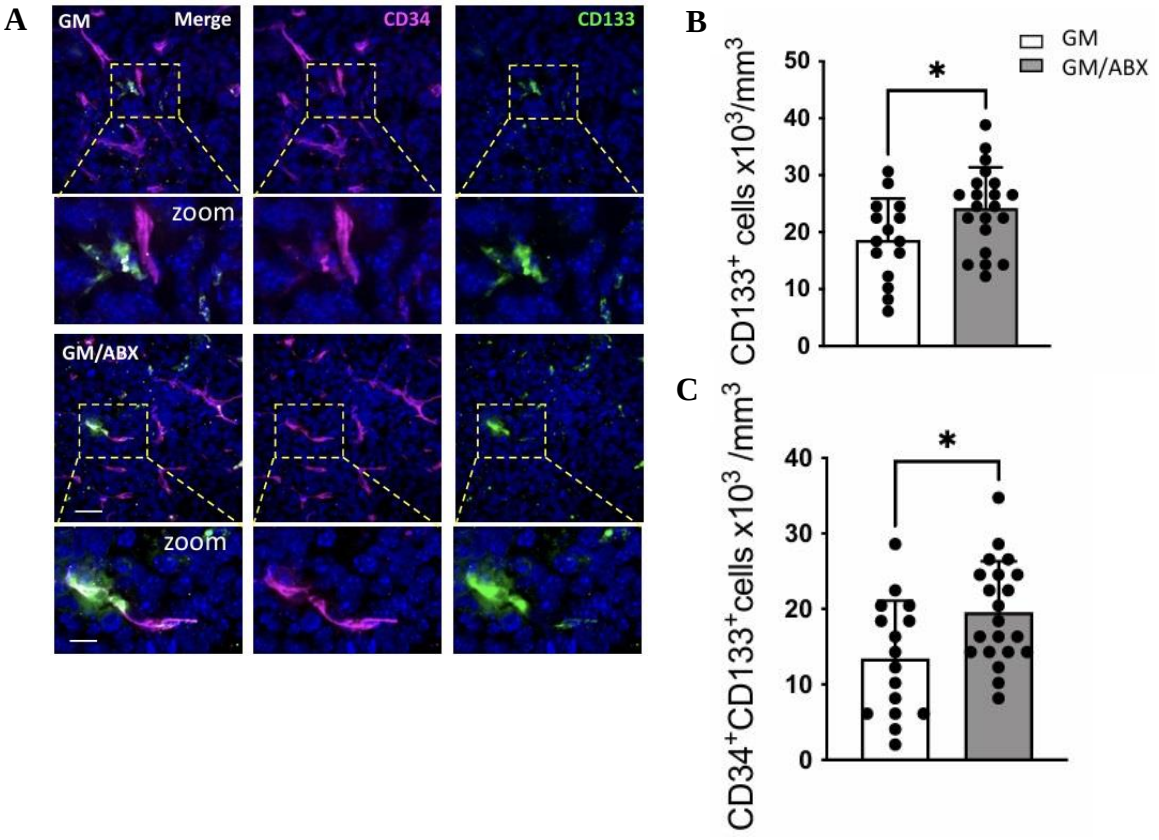

Figure 8: (A) Representative z-projection confocal images of CD34 (magenta) and CD133 (green) in GM and GM/ABX tumor core area. Hoechst staining (blu) for nuclei visualization Scale bar: 25 μm; zoom 10 μm. **(B)** Scatter dot plots showing quantification of $CD133^+$ positive cells (GM: n=16/7/3 FOV/slices/mice; GM/ABX: n=21/8/3 FOV/slices/mice. Data are presented as the mean ± SD *p <0.05; Student's t-test). **(C)** Scatter dot plots showing quantification of $CD133^+$ $CD34^+$ double-positive cells (GM: n=16/7/3 FOV/slices/mice; GM/ABX: n=21/8/3 FOV/slices/mice. Data are presented as the mean ± SD *p <0.05; Student's t-test).

In order to investigate the origin of these vessel-like structures, mice were inoculated with $GL261^{rfp}$ cells, and tissue sections from GM-transplanted mice were stained for CD34 to identify GL261 cells expressing the endothelial marker. Confocal immunofluorescence analysis describes that GM/ABX mice exhibit higher $GL261^{rfp+}$ $CD34^+$ colocalization signals with respect to GM mice in the tumor core area (Fig. 9A, B) (GM 2.5 ± 0.5, GM/ABX 5.33 ± 1.2 colocalization efficiency %; *** p< 0.001). These data demonstrate that ABX treatment promotes the GL261 trans-differentiation towards the endothelial phenotype.

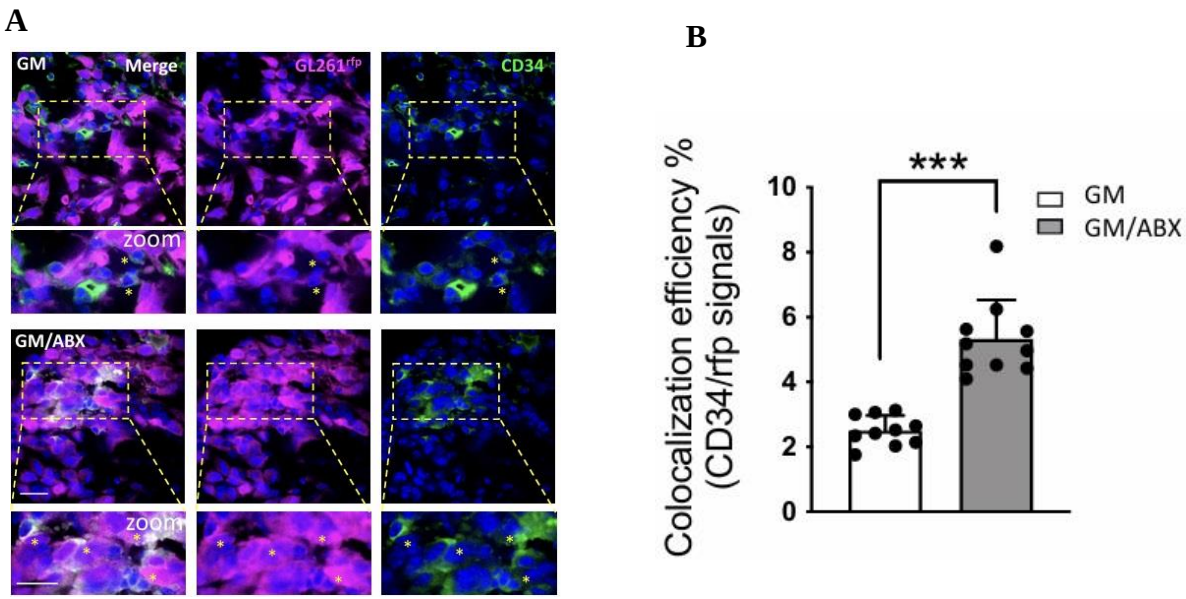

Figure 9: (A) Representative single plane confocal images of $GL261^{rfp}$ (magenta) and CD34 (green) in GM and GM/ABX tumor core area. Hoechst staining (blu) for nuclei visualization. 60x objective (Scale bar: 20 μm; zoom 20 μm). Yellow stars indicate the colocalizing signals. **(B)** Scatter dot plots showing the percentage of rfp-CD34 colocalizing signals (GM n=40/10/3 FOV/slices/mice; GM/ABX n=40/10/3 FOV/slices/mice). Data are presented as the mean ± SD *** p <0.001 Student's t-test.

Endothelial progenitor cells infiltration is not modulated by ABX treatment:

Since the formation of new vessels in tumors can be supported by the mobilization and the integration of circulating endothelial progenitor cells that are present in glioma[34], we investigated the presence of $CD45^+CD34^+$ hematopoietic progenitors in the tumoral brain hemisphere. By immunofluorescence, we detected the presence of $CD45^+CD34^+$ double-positive cells (Fig. 10A) that can be identified in the tumoral core as a cell population distinct from the $CD45^-CD34^+$ vessel-like structure. We then investigated, by flow cytometry analysis, the frequency of $CD34^+$ cells among the total $CD45^+$ cells (GM 16.04 ± 5.3, GM/ABX 11.41 ± 4.4 % of cells; p=0.17; n=5 animals per group; (Fig. 10B), discriminating the peripheral infiltrating ($CD45^{high}$) (GM: 5.91 ± 2.9; GM/ABX: 4.67 ± 4.3 % of cells; p=0.38; n=5 animals per group; Fig. 10C) from the resident ($CD45^{int}$) cells (GM: 19.24 ± 6.7; GM/ABX: 13.84 ± 4.5% of cells; p=0.17; n=5 animals per group; Fig. 10D). Our data demonstrated that ABX treatment does not affect the abundance of $CD45^+CD34^+$ cells.

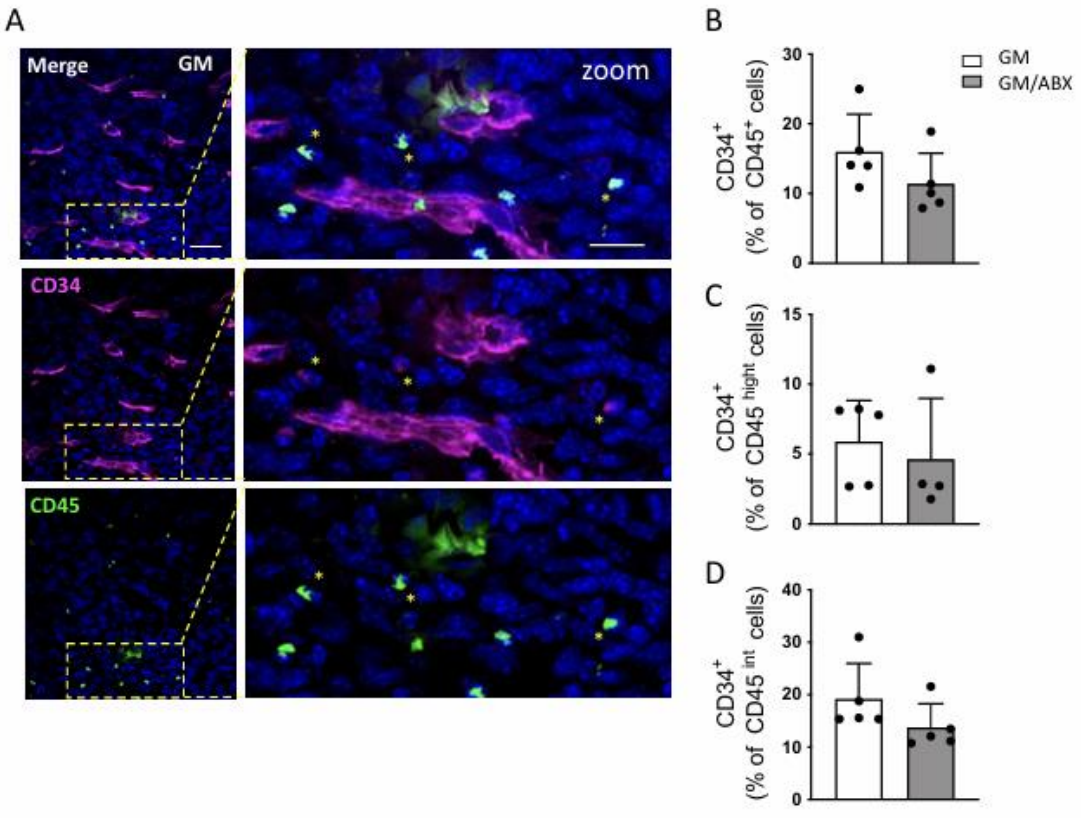

Figure 10: (A) Representative z-projection confocal images of CD34 (magenta) and CD45 (green) in the GM tumor core area. Hoechst staining (blu) for nuclei visualization. 60x objective (Scale bar: 25 µm; zoom 20 µm). Yellow stars indicate the $CD45^+CD34^+$ cells. (**B)** Flow cytometry quantification of $CD45^+CD34^+$ cells in GM and GM/ABX tumoral hemisphere. (**C)** $CD45^{high}CD34^+$ population identifying the peripheral

infiltrating hematopoietic endothelial progenitor cells and (**D**) $CD45^{int}CD34^{+}$ identifying the resident brain population expressing the CD34 marker (mostly likely microglia/macrophages). $n = 5$ mice per group. Data are presented as the mean ± SD.

Glycine induces TME and glioma cells to adopt a pro-angiogenic phenotype:

It has been demonstrated that long-term ABX treatment compromises the composition and functions of the gut microbiota inducing long-lasting detrimental effects on the host. To evaluate the perturbations induced by 2 weeks ABX treatment, ^{1}H NMR metabolomic analysis has been carried out on fecal waters and brain extracts of these mice. In Fig. 11A, spectrum of fecal water is reported and total of thirty-three metabolites have been quantified by NMR spectroscopy (table 1). From the comparison of Ctrl and ABX spectra (Fig. 11B), we observed that the ABX treatment has determined the almost total disappearance of the shorth chain fatty acids (butyrate, propionate, acetate) signals, while signals of choline and molecule attributed to a glycine derivative (Gly-derivative) based on HSQC and HMBC experiments, were much more intense in ABX, with a 32-fold and 83-fold average increase respectively. Furthermore, the fecal water spectra of ABX-treated mice exhibited a series of broad, unresolved bands between 3 ppm and 5.5 ppm, signals attributed to gentamicin and vancomycin metabolites and therefore not included in the quantitative analysis and statistical discussion.

A

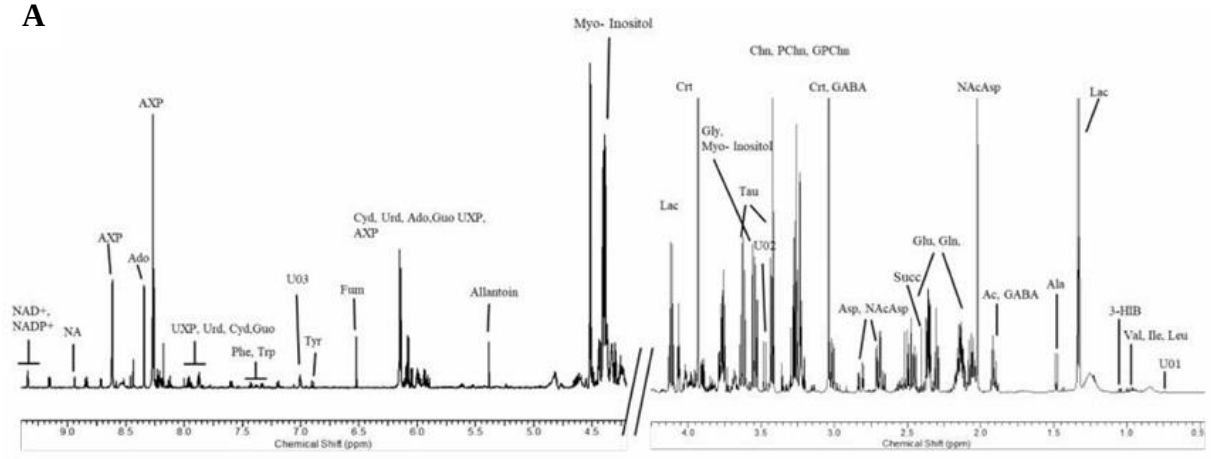

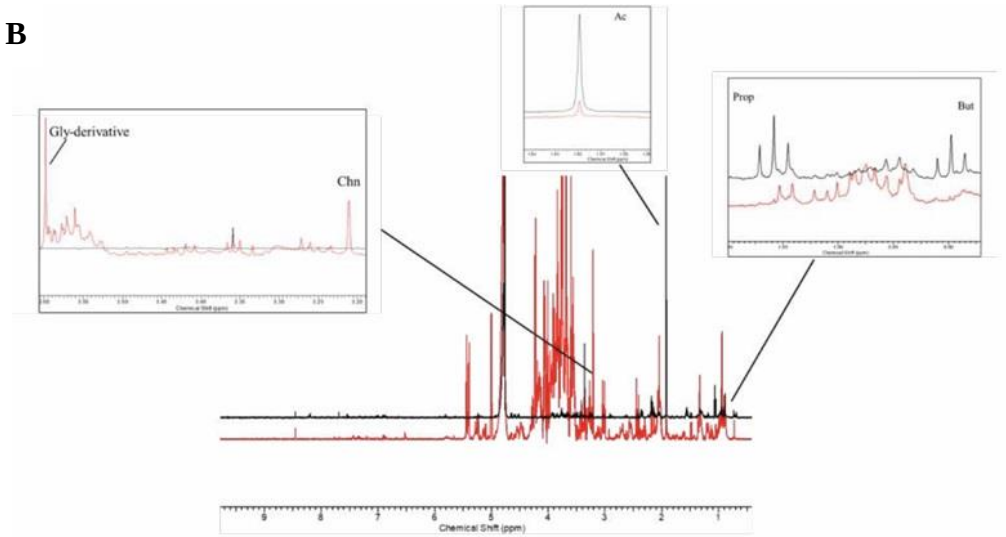

Figure 11: (A) ^{1}H NMR spectrum of fecal water from a control mouse. **(B)** Superimposed fecal water spectra from control (black) and ABX-treated (red) mice. In the insets are highlighted the spectra of Gly-derivative, choline, and SCFA.

Table 1. ^{1}H NMR assignment of mice's fecal water

Supplementary Table 1: ^{1}H NMR assignment of mice's fecal waters.				
Metabolites	**^{1}H δ (ppm)**	**Moiety**	**Multiplicity**	**Level of Assignment***
2-Oxoglutarate (2-Oxoglut)	2.44	β-CH_2	T	3
	3.02	α-CH_2	T	
2-Oxoisovalerate (2-OxoIV)	1.13§	CH_3, CH_3'	D	2
Acetate (Ac)	1.92§	CH_3	S	2
Alanine (Ala)	1.48§	β-CH_3	D	2
	3.77	α-CH	Q	
Bile salts 1 (BS1)	0.68§	CH_3	Bs	3
Bile salts 2 (BS2)	0.70§	CH_3	Bs	3
Bile salts 3 (BS3)	0.72§	CH_3	Bs	3
Butyrate (But)	0.88	γ-CH_3	T	
	1.56§	β-CH_2	M	1
	2.16	α-CH_2	T	
Caproate (Cap)	0.86§	ε-CH_3	T	2
	1.28	γ-CH, δ-CH_2'	M	
	1.54	β-CH_2	M	
	2.16	α-CH_2	T	
Choline (Chn)	3.20§	CH_3, CH_3', CH_3''	Bs	3
Ethanol (EtOH)	1.18§	CH_3	T	2
	3.65	CH_2	Q	
Formate (For)	8.46§	CH	S	2
Fumarate (Fum)	6,52§	CH=CH	S	2

Glutamate (Glu)	2.04	β-CH	M	
	2.11	β-CH’	M	
	2.35§	γ-CH_2	Pt	2
Glycine-derivative (Gly-derivative)	3.60§	CH_2	S	3
Hypoxanthine (Hyp)	8.19	CH	S	
	8.21§	CH	S	2
Isoleucine (Ile)	0.95	CH_3	T	
	1.01§	CH_3’	D	2
	1.26	γ-CH	M	
	1.48	γ-CH’	M	
	1.96	β-CH	M	
Lactate (Lac)	1.33	CH_3	D	
	4.11§	CH	Q	2
Leucine (Leu)	0.97§	CH_3, CH_3’	Pt	2
	1.70	β-CH_2, γ-CH	M	
Lysine (Lys)	1.46	γ-CH_2	M	
	1.70§	δ-CH_2	M	3
	1.90	β-CH_2	M	
	3.02	ε-CH_2	Pt	
	3.75	α-CH	M	
Methanol (MeOH)	3.36§	CH_3	S	2
Nicotinate (NA)	7.52	CH	T	
	8.25	CH	D	
	8.61	CH	D	
	8.94§	CH	Bs	2
Phenylalanine (Phe)	7.33-7.43§	1-5 CH	M	3
Propionate (Prop)	1.05	β-CH_3	T	
	2.17§	α-CH_2	Q	1
Succinate (Succ)	2.41§	α-CH_2, β-CH_2	S	3
Trymethylamine (TMA)	2.91§	CH_3, CH_3’, CH_3’’	S	3
Tyrosine (Tyr)	6.90	2-CH, 6-CH	D	
	7.20§	3-CH, 5-CH	D	3
Uracil (U)	5.80	CH	D	2
	7.55§	CH	D	
Valine (Val)	0.99§	CH_3	D	2
	1.04	CH_3’	D	
	2.26	β-CH	M	
	3.60	α-CH	D	
α-Glucose (α-Glc)	3.52		M	
	3.66		M	
	5,24§	1-CH	D	2
β-Arabinose (β-Ara)	3.53			

	3.65 3.92 4.53§	1-CH	D	3
β-Galactose (β-Gal)	3.50 3.65 3.95 4.59§	1-CH	D	3
β-Xylose (β-Xyl)	3.24 3.44 3.62 4.57§	1-CH	D	3

Keynotes:

- Integrated moiety §

s: singlet; d: doublet; pd: pseudo-doublet; t: triplet; bs: broad singlet, m: multiplet; dd: doublet of doublets; pt: pseudo-triplet; q: quartet.

* Level 1: identified metabolites; level 2: putatively annotated compounds; level 3: putatively characterized compound classes; level 4: unknown compounds. The level of assignment has been reported according to Salek M. R. et al. doi: 10.1186/2047-217X-2-13

We then applied the PLS model to the data matrix. The optimal complexity of the PLS model, as assessed by full cross-validation, was found to be three LVs, which explained the 99.39% and 74.47% of the total variance on x and y, respectively. The validation results were R2= 1, Q2=0.97 and ROC =1 (Fig 12A, left) for correctly classifying ABX from CTRL. Seventeen metabolites were mostly responsible for the discrimination, in particular Gly-derivative, Choline (Chn), Leucine (Leu), Valine (Val), Lactate (Lac) were higher and Hypoxanthine (Hyp), Acetate (Ac), beta-Xylose (beta-Xyl), Trimethylamine (TMA), Uracil (Ura), alpha-Glucose (alpha-Glc), Nicotinate (NA), beta-Galactose (beta-Gal), Propionate (Prop), Bile salts 1, Glutamate (Glu) and Butyrate (But) were significantly lower after ABX treatment (Fig. 12A, right).

NMR-based metabolomics of murine cerebral tissue showed a different profile after ABX treatment compared to the CTRL group. As depicted by the PLS score plot in Fig. 12B left, the first three LVs explained the 92.82% on x and 57.29% on y of the total variance, showing a R2=0.68, Q2=0.89 and ROC=0.97. Thirteen variables were significantly involved in the separation of the groups as indicated by the VIP scores > 1 (Fig. 12B, right). In particular, Glu, Guanosine (Gua), γ-aminobutyric acid (GABA), Chn, Glycine (Gly), Unknow 01 (U01) and

Unknow 03 (U03) were higher in ABX, while the levels of valine (Val), tyrosine (Tyr), Lac, histidine (His), tryptophan (Trp), phenylalanine (Phe) were lower in ABX compared to CTRL.

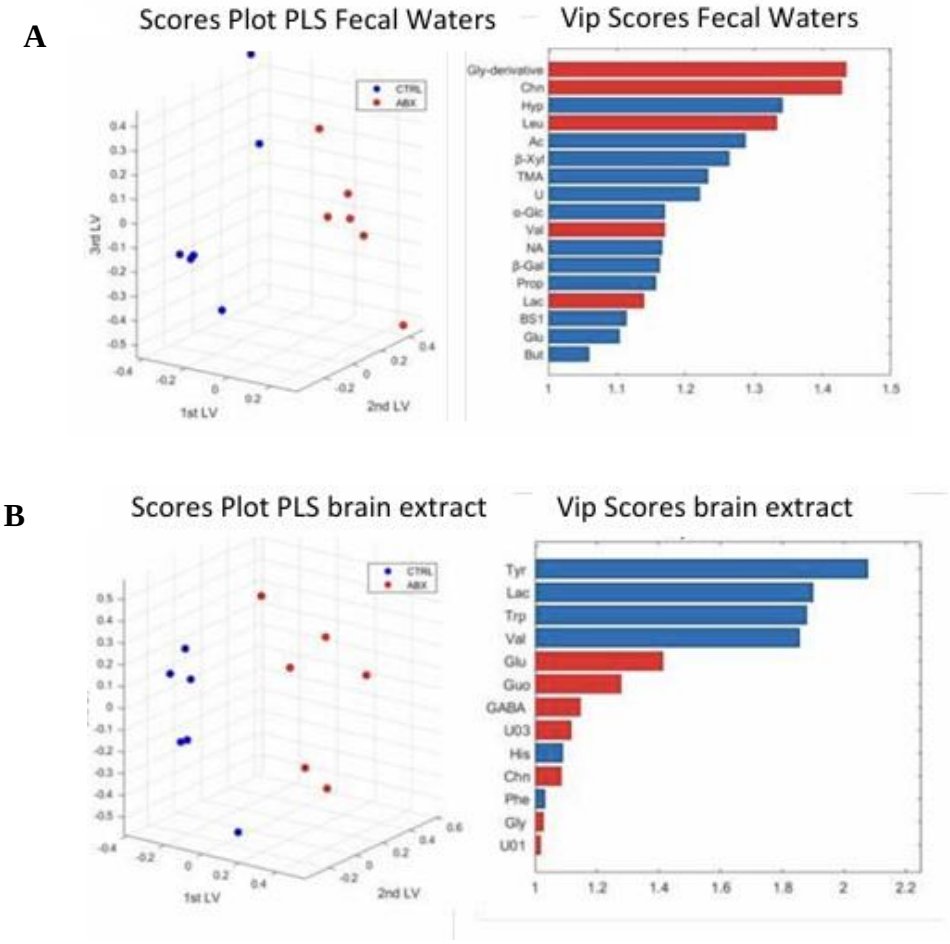

Figure 12: (A) PLS scores plot (left) and VIP scores (right) of fecal waters from CTRL (blue) and ABX-treated mice (red). **(B)** PLS scores plot (left) and VIP scores (right) of brain extracts from CTRL (blue) and ABX-treated mice (red). VIP values are reported in horizontal histograms and values of VIP higher than 1 are statistically significant. The metabolite that is higher in ABX is reported in red, while the metabolite that is lower in ABX is reported in blue.

In brain extracts, thirty-nine molecules have been identified and quantified by 1H-NMR and were also included for six CTRL and six ABX-treated mice (table 2). A representative spectrum of the brain is also reported in Fig. 13.

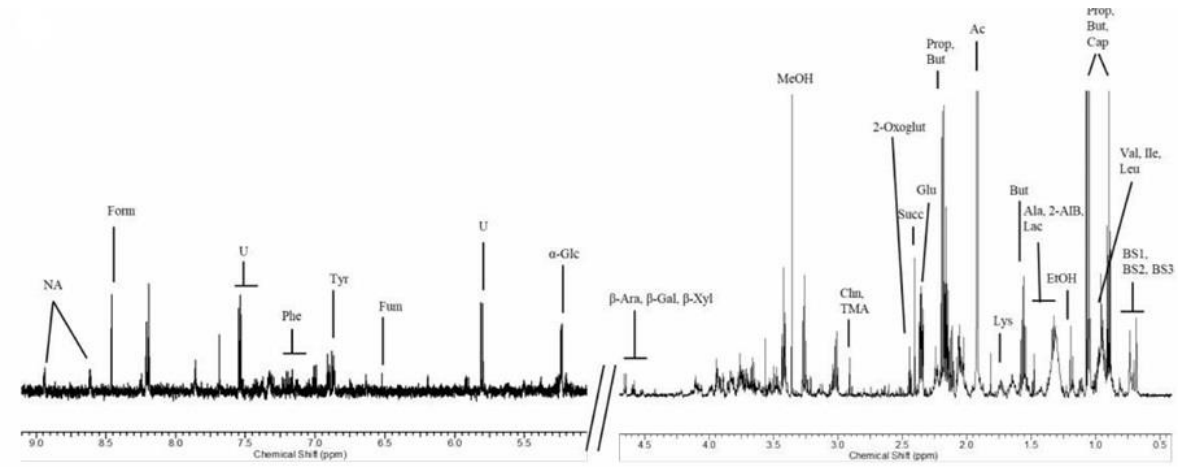

Figure 13: [1]H NMR spectrum of brain extract from a control mouse.

Table 2. [1]H NMR assignment of mice's brain extracts

Supplementary Table 2: [1]H NMR assignment of brain exctracts.				
Metabolites	**^{1}H δ (ppm)**	**Moiety**	**Multiplicity**	**Level of Assignment***
3-Hydroxyisobutyrate (3-HIB)	1,07§	CH_3	d	3
	2,52			
	3,55			
	3,72			
Acetate (Ac)	1,92§	CH_3	s	2
Adenosine (Ado)	8,18	CH	s	
	8,34§	CH	s	3
Alanine (Ala)	1.48§	β-CH_3	d	2
	3.77	α-CH	q	
Allantoin (All)	5.38		s	
Aspartate (Asp)	2.65	β-CH	dd	
	2.80§	β-CH'	dd	2
	3.98	α-CH	dd	
Adenosine phosphate (AXP)	8.27	CH	s	
	8.61§	CH	s	3
Choline (Chn)	3.20§	CH_3, CH_3', CH_3''	s	3
Creatine (Crt)	3.04	CH_3	s	
	3.93§	CH_3	s	
Cytidine (Cyd)	6.12	CH	d	
	7.84§	CH	d	3
Formate (Form)	8.46§	CH	s	3
Fumarate (Fum)	6.53§	CH=CH	s	3
γ-aminobutyrate (GABA)	1.90§	β-CH_2	m	2

	2.30	α-CH_2	t	
	3.02	γ-CH_2	t	
Glutamine (Gln)	2.13	β-CH_2	m	
	2.46§	γ-CH_2	m	2
	3.78	α-CH	m	
Glutamate (Glu)	2.04	β-CH	m	
	2.11	β-CH’	m	
	2.35§	γ-CH_2	pt	2
	3.75	α-CH	m	
Glycine (Gly)	3.56§	CH_2	s	2
Glycerophosphocholine (GPChn)	3,24§	CH_3, CH_3’, CH_3’’	s	3
Guanosine (Guo)	8.00§	CH	s	3
Histidine (His)	7.05	CH	s	
	7,78§	CH	s	3
Isoleucine (Ile)	0.95	CH_3	t	
	1.01§	CH_3’	d	2
	1.26	γ-CH	m	
	1.48	γ-CH’	m	
	1.96	β-CH	m	
Lactate (Lac)	1.33	CH_3	d	
	4.11§	CH	q	2
Leucine (Leu)	0.97§	CH_3, CH_3’	pt	2
	1.70	β-CH_2, γ-CH	m	
Myo-Inositol (Myo-Ino)	3.27	4-CH	t	
	3.52§	2-CH, 6-CH	dd	2
	3.60	3-CH,5-CH'	t	
	4.05	1-CH	pt	
N-Acetyl Aspartate (NAcAsp)	2.03§	CH_3	s	2
	2.50	α'-CH	dd	
	2.70	α'-CH'	dd	
	4.40	α-CH	dd	
Nicotinamide adenine dinucleotide+ (NAD+)	8.83	CH	d	
	9.14	CH	d	
	9,33§	CH	bs	3
Nicotinamide adenine dinucleotide phosphate+ (NADP+)	8,82	CH	d	
	9,11	CH	d	
	9,3	CH	bs	3
Nicotinate (NA)	7.52	CH	t	
	8.25	CH	d	
	8.61	CH	d	
	8.94§	CH	bs	2

Phenylalanine (Phe)	7.33-7.43§	1-5 CH	m	3
Phosphocholine (PChn)	3,22§	CH_3, CH_3', CH_3''	s	3
Succinate (Succ)	2.41§	α-CH_2, β-CH_2	s	3
Taurine (Tau)	3,26	CH_3	t	
	3,42§	CH_3	t	3
Tryptophan (Trp)	7.19	5-CH	t	
	7.27	6-CH	t	
	7.53	7-CH	d	
	7.73§	4-CH	d	
Tyrosine (Tyr)	6.90	2-CH, 6-CH	d	
	7.20§	3-CH, 5-CH	d	3
U01	0,75§		s	4
U02	3,47§		d	4
U03	7.00§		bs	4
Uridine (Urd)	5.90	CH	d	
	7.88§	CH	d	3
Uridine phosphate (UXP)	5.93-5.97	CH	d	
	8.11§	CH	d	
Valine (Val)	0.99	CH_3	d	2
	1.04§	CH_3'	d	
	2.26	β-CH	m	
	3.60	α-CH	d	

Keynotes:

- Integrated moiety §

s: singlet; d: doublet; pd: pseudo-doublet; t: triplet; bs: broad singlet, m: multiplet; dd: doublet of doublets; pt: pseudo-triplet; q: quartet.

* Level 1: identified metabolites; level 2: putatively annotated compounds; level 3: putatively characterized compound classes; level 4: unknown compounds. The level of assignment has been reported according to Salek M. R. et al. doi: 10.1186/2047-217X-2-13

We focused our attention on glycine since previous studies demonstrated that this aminoacid has pro-angiogenic activities [42] and that GL261 cells express the intracellular glycine receptor GlyRa1[43]. We first investigated whether glycine could affect microglial cell phenotype in the context of glioma. To this aim, RT-PCR analysis was performed on primary microglial cells cultured in GL261 conditioned medium (GCM) in the presence or in the absence of glycine (300 mM), for 72h. Data reported in Fig 14A, show that glycine-treated microglia have an increased expression of P2y6r, Cd68, Mmp9, and Vegfa, all genes related to phagocytosis and angiogenesis (** p< 0.01; *** p< 0.001). Moreover, we analyzed the effect of glycine on cultured GL261 cells and observed an increased expression of stemness-related genes such as Cd133, Nestin, Cd34, Olig2, and Cd44 (Fig. 14B) (* p< 0.05; ** p< 0.01). No variation of Sox2 transcripts was observed. Glycine administration did not affect GL261 cell viability (MTT assay) and proliferation (BrdU assay) as reported in Fig. 14C, D.

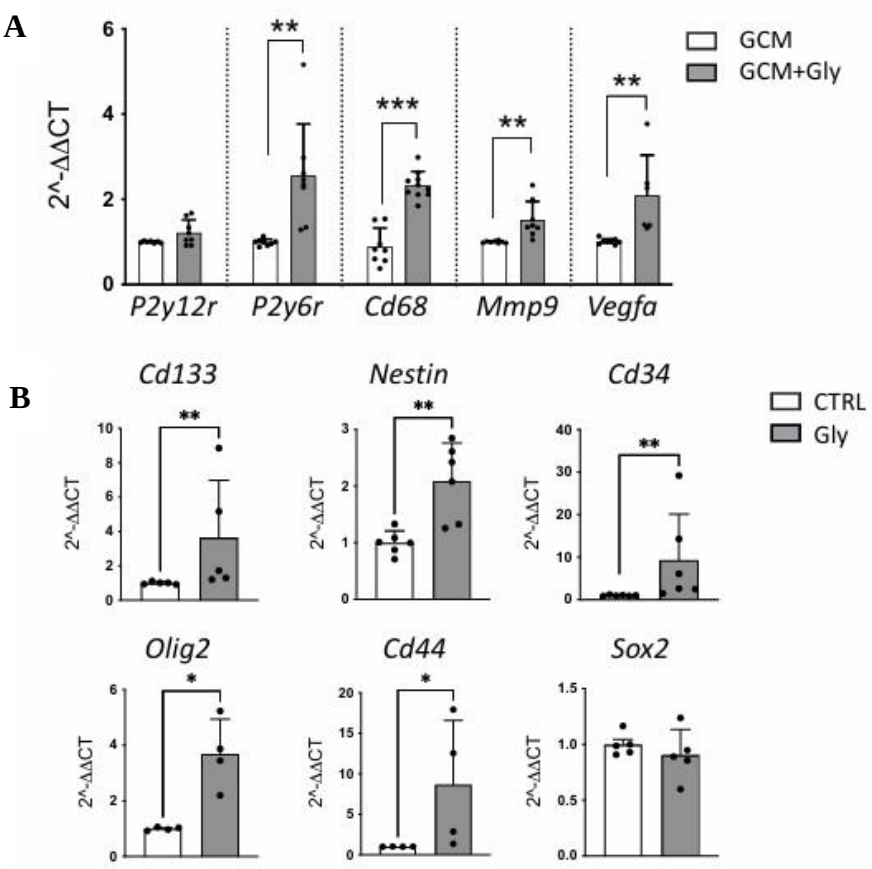

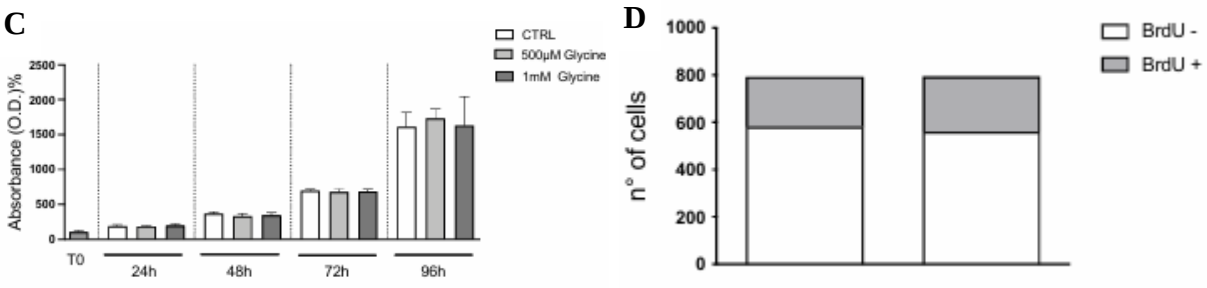

Figure 14: (A) RT-qPCR from microglia mRNA. Gene expression is normalized to the housekeeping gene Gapdh, $n = 4–6$ independent experiments. Data are presented as the mean ± SD ***$p < 0.001$; **$p < 0.01$; Student's *t-test*. **(B)** RT-qPCR from GL261 mRNA. Gene expression is normalized to the housekeeping gene Gapdh, $n = 4–6$ independent experiments. Data are presented as the mean ± SD **$p < 0.01$; *$p < 0.05$, Student's *t-test*. **(C)** GL261 proliferation analysis by MTT assay after treatment with Glycine at the indicated concentrations and time points. **(D)** GL261 analysis of BrdU positive cells after Glycine treatment. Data are expressed as the number of BrdU+ cells (gray bars) within the total counted cells (white bars).

Co-option of the pre-existing vessels in the neighboring tissue is one of the most critical steps utilized by the tumor to support the metabolic and nutrient needs [44]. We thus investigated if glycine treatment can establish an angiogenic-like model in endothelial cells and reported that bEND3 cells treated with glycine show increased cell proliferation, cell sprouting, and connections as shown by the formation of a complex mesh of cells that generate polygon structures [45] (Fig 15A, B). All these data show that ABX treatment results in the increased level of several factors in the brain including glycine. The latter, acting on different cellular targets, promotes stemness and angiogenesis.

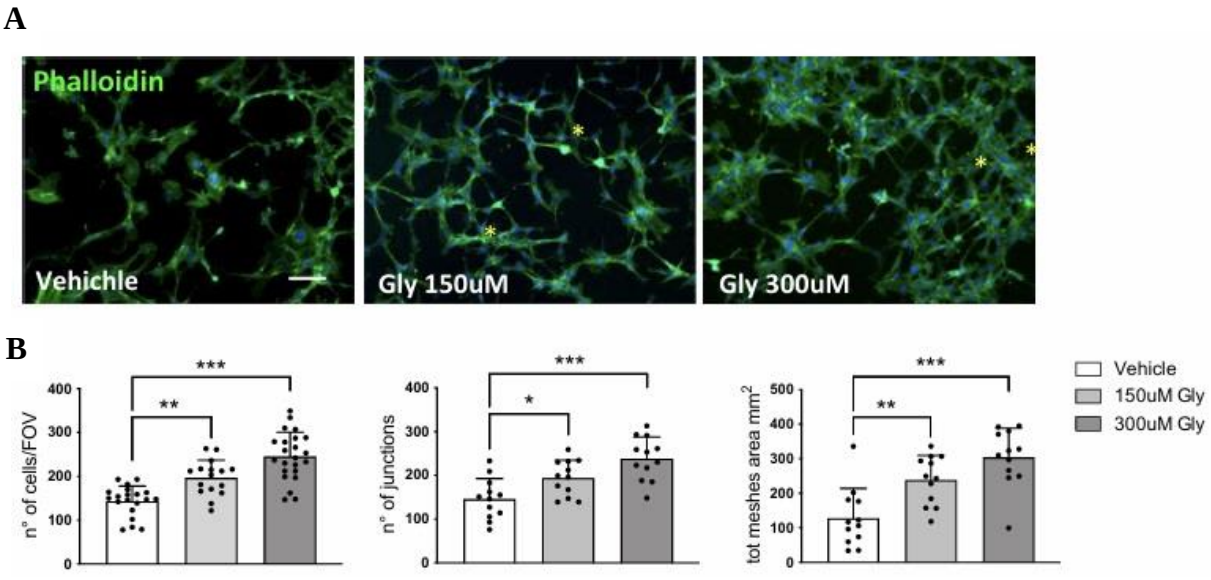

Figure 15: (A) Representative images of bEnd.3 cells labeled with Alexa Fluor 488-conjugated phalloidin (green) and Hoechst for nuclei visualization (blue). Yellow asterisk indicates junctions and meshes wall generated in cell culture upon glycine treatment. Scale bar: 25 μm. **(B)** Plot showing the number of cells counted per field of view (FOV) (Left), the number of junctions (middle), and total meshes area (right) in the *in vitro* cell angiogenesis assay. (Vehicle n = 20, 150 μM glycine n = 16, and 300 μM n = 23 FOV from 3 independent experiments). Data are presented as the mean ± SD *** p <0.001; ** p <0.01; * p <0.05. One-way ANOVA - Dunnett's multiple comparison test.

Glycine promotes glioma growth and vasculogenesis in ABX-treated mice:

To validate the *in vivo* effect of glycine in promoting tumor growth and vasculogenesis, we tested the effect of a selective and orally active glycine transporter 1 (GlyT1) inhibitor. It has been demonstrated that GlyT1 inhibitor is able to increase the plasma and cerebrospinal fluid glycine concentration in rats and humans [46].

We analyzed the tumor volume in GM and GM/ABX mice treated or not with GlyT1 inhibitor: the treatment can significantly increase the tumor volume in GM/ABX mice versus GM mice (GM + GlyT1 inh. 5.68 ± 2.8, GM/ABX+ GlyT1 inh. 19.14 ± 5.14 mm^3 ***p < 0.001) and further increases the ABX effect on tumor growth (GM/ABX 10.39 ± 1.9, GM/ABX + GlyT1 inh. 19.14 ± 5.14 mm^3 **p < 0.01) (Fig 16A, B). Moreover the immunofluorescence staining for vessel-like structure characterization revealed that GM/ABX mice treated with the GlyT1 inhibitor exhibit a higher reactivity for CD34 in the tumoral core versus GM mice (GM + GlyT1 inh. 3.1 ± 0.1, GM/ABX + GlyT1 inh. 7.06 ± 0.2 % of area/FOV; ***p < 0.001) and that GlyT1 inhibitor treatment boost the vasculogenic effect mediated by ABX administration (GM/ABX 4.3 ± 0.2, GM/ABX + GlyT1 inh 7.06 ± 0.2 % of area/FOV; ***p < 0.001) (Fig 16C, D).

Altogether these results show that glycine mediates glioma growth and vasculogenesis in ABX-treated mice.

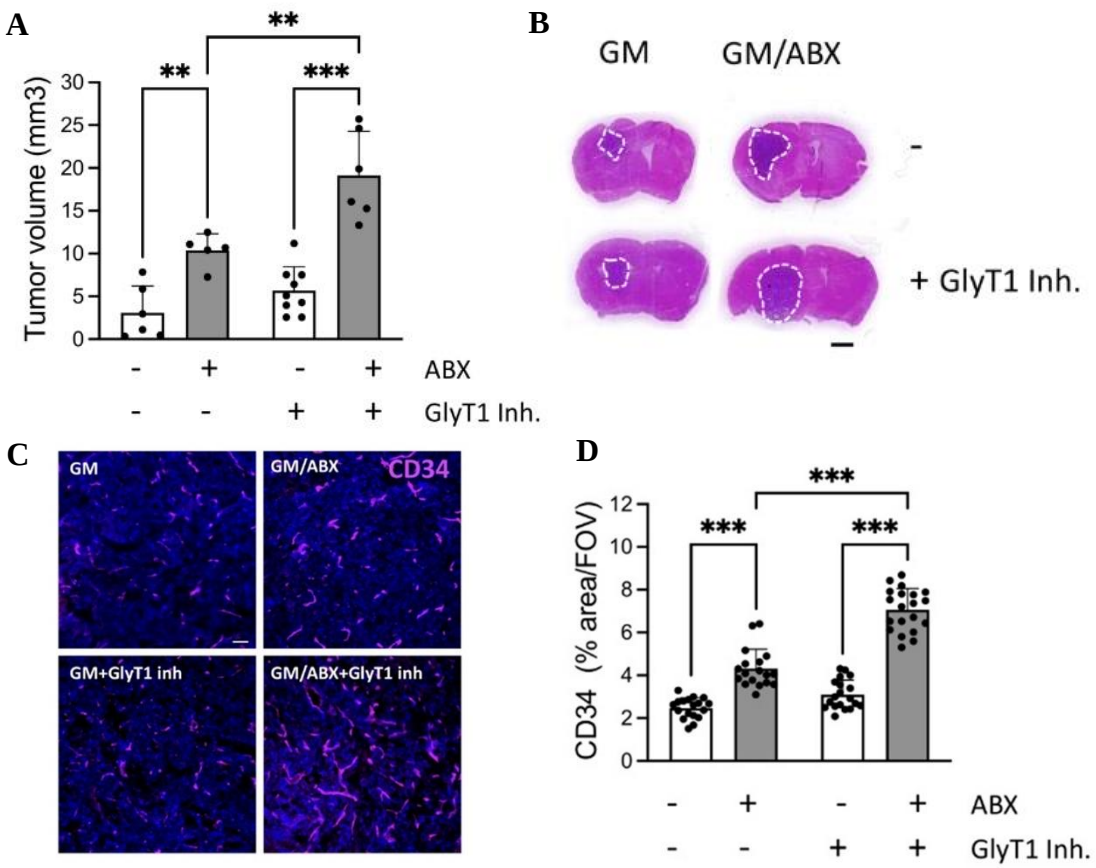

Figure 16: (A) Tumor size in GM and GM/ABX mice with or without GlyT1 inhibitor, $n = 5–9$, pooled from two experiments. Data are presented as the mean ± SD $^{**}p < 0.01$, $^{***}p < 0.001$, one-way ANOVA followed by Tukey's multiple comparison test. **(B)** Representative images of brain coronal slices, scale bar = 1 mm. **(C)** Representative confocal images of CD34 (magenta) in GM and GM/ABX tumor core area. Hoechst staining (blu) for nuclei visualization Scale bar: 50 μm. **(D)** Scatter dot plots showing quantification of CD34 signal expressed as the percentual area occupied by fluorescent CD34 staining in GM ($n = 18/3$ slices/mice), GM/ABX ($n = 18/3$ slices/mice), GM + GlyT1 inh ($n = 19/3$ slices/mice), GM/ABX + GlyT1 inh ($n = 20/3$ slices/mice) mice versus total field of view (FOV) Data are presented as the mean ± SD $^{***}p < 0.001$; one-way ANOVA followed by Tukey's multiple comparison test.

Discussion

The gut microbiota and metabolome are increasingly recognized as critical regulators of brain functions and host disease pathogenesis [47]. The intricate communication between the gut microbiota and the CNS, often referred to as the gut-brain axis, involves a variety of mechanisms, including neural, immune, and metabolic pathways. Disruptions in this relationship, commonly termed gut dysbiosis, can result from various factors such as poor diet, infections, environmental stressors, and drug exposure. Dysbiosis leads to reduced microbial diversity and alterations in metabolite production, which may predispose the host to several pathologies, including neurodegenerative diseases and cancer. Specifically, a strong association between the gut microbiome and microglial functions has been reported in recent years. Consistent with this, our earlier work demonstrated that prolonged antibiotic administration disrupts gut microbial composition and exacerbates glioma growth in mice [3]. In this study, we investigated the metabolic and phenotypic changes induced by long-term treatment with non-absorbable antibiotics, gentamicin, and vancomycin, in glioma-bearing mice. We focused on the impact of these changes on the glioma TME, with a particular emphasis on tumor angiogenesis and tumor progression. Notably, we identified glycine as a putative mediator of the pro-angiogenic phenotype induced by ABX treatment in glioma-bearing mice.

Glioma-associated macrophages, which include resident microglia and peripheral macrophages, are a prominent immune cell population within glioma tumors and play pivotal roles in tumor progression. Previous studies have shown that GAMs contribute to angiogenesis, immunosuppression, and tissue remodeling. While we did not differentiate between microglia and peripheral macrophages in this study, our findings revealed that CD11b+ cells isolated from the tumor-bearing hemispheres of ABX-treated mice exhibited a pro-angiogenic and phagocytic phenotype. This was evidenced by the increased transcriptional expression of key markers such as Vegfa, Mmp9, and Cd68. These markers are directly associated with vasculogenesis, extracellular matrix remodeling, and phagocytic activity, respectively [48]. The pro-angiogenic activity of GAMs observed in our study aligns with their known role in promoting tumor progression and establishing a supportive TME.

Additionally, we observed that ABX treatment impaired the functional phenotype of microglia, as evidenced by decreased expression of both pro-inflammatory and anti-inflammatory genes. This indicates a dysregulated immune state, which is further supported by impaired microglial responses to ATP a common indicator of homeostatic disturbances in the brain. These

observations are consistent with prior studies showing that germ-free and antibiotic-treated mice exhibit altered microglial phenotypes, including changes in morphology and functionality [49].

Glioblastoma, like other solid tumors, relies on blood supply by specialized vascular structures to meet the increased metabolic demands [50], and vasculature, in brain tumors, correlates with their aggressive phenotype. In the complex glioblastoma landscape, several mechanisms drive vasculogenesis: i) the recruitment of circulating endothelial progenitor cells into the vascular architecture of brain tumor [51]; ii) the lining of tumor vessels and tumor cells; iii) a process of transdifferentiation where cancer stem-like cells differentiate into endothelial cells [52]. Here we reported that GM/ABX-treated mice exhibit increased $CD34^{+}CD31^{+}$ vascular-like structure in the tumor core. Moreover, the increased abundance of $CD133^{+}CD34^{+}$ cell population suggests that the process of vasculogenesis may rely on one or more stem cell populations inside the tumor area. In addition, we found that ABX treatment increases the expression of the CD34 marker on $GL261^{rfp}$ cells, suggesting glioma cell transdifferentiation into an endothelial progenitor phenotype.

The increased vasculogenesis could also depend on infiltrating hematopoietic $CD34^{+}$ stem cells [51]; upon ABX treatment, however, we found no significant changes in the abundance of $CD45^{+}CD34^{+}$ hematopoietic stem cells, indicating that blood-derived EPCs do not contribute to this process in our experimental conditions. These findings suggest that vasculogenesis in ABX-treated mice primarily relies on local tumor-resident cells, including glioma stem-like cells and endothelial progenitor-like cells, rather than systemic contributions.

In order to identify putative mediators that can contribute to ABX-induced glioma growth and tumor vasculogenesis, we took advantage of the metabolomic analysis of brain extracts by ^{1}H NMR, and identified glycine and its derivatives as metabolites associated with ABX treatment in glioma-bearing mice.

Glycine is an amino acid that plays essential roles in many biological processes, including immunomodulation, neurotransmission, and angiogenesis, both in physiological and pathological conditions. Glycine affects microglial phenotype in an in vivo model of brain ischemia and modulates phagocytosis in the BV2 microglial cell line. We described that primary cultures of microglial cells respond to glycine treatment increasing the expression of P2y6 receptor and Cd68, both associated with phagocytosis, and increasing the expression of Mmm9 and Vegfa, involved in tissue remodeling and angiogenesis.

The role of glycine has been investigated in different tumors. In glioma, glycine facilitates tumor progression by acting on its intracellular receptor GlyRa1, and GlyRa1 silencing reduces

glioma volume in mice[43]. More recently, glycine has been proposed as a biomarker of glioma subtypes and grades, being abundant in IDH mutants and glioblastoma.

We demonstrate that glycine administration to GL261 cells increases the expression of the stemness-related gene CD133, without affecting cell proliferation. Cancer stem cells have been characterized in glioma and play important roles in driving tumor growth. CD133+ GL261 cells generate gliomaspheres with high proliferative index [53].

Glycine also increased the frequency of CD34+ CD133+ GL261 cells, indicative of an effect on glioma cell transdifferentiation toward an endothelial phenotype. Moreover, the increased transcriptional level of oligodendrocyte transcription factor 2 (OLIG2) suggests that GL261 trans-differentiation is linked to multiple strategies of tumor vasculature production and remodeling. It has been shown that Olig2+ oligodendrocyte precursor-like glioma cells are involved in the process of tumor vasculogenesis[54]. Additional GSCs markers increased upon glycine treatment are CD44, a large cell adhesion molecule that interacts with the extracellular matrix components and is positively correlated with tumor invasion and progression and nestin. The high expression of nestin has been correlated to increased glioma proliferation and is a bona fide marker of angiogenesis [55]. Glycine function in the angiogenesis process has been also described by Guo and colleagues, in a mouse model of hindlimb ischemia, where glycine administration promoted neovascularization and recovery of vascular flow. In accordance, here we also found that glycine improves the endothelial cells network in the bEnd3 cell line.

We have studied the role of glycine in ABX treated mice, taking advantage of a GlyT1 selective inhibitor. Our results show that increased levels of glycine in the brain further boost the ABX effect on glioma growth and vascularization. The effect on glioma growth is in line with what reported by Förstera and colleagues [43], which showed how the knockdown of the intracellular glycine receptor (GlyR1) in GL261 impairs tumor progression. In ABX-induced dysbiosis, the brain metabolic profile is altered and, in this specific brain microenvironment, glycine is fueling glioma growth.

In conclusion, this study demonstrates that ABX-induced gut dysbiosis profoundly impacts the glioma TME. Among the metabolites identified, glycine plays a central role in promoting angiogenesis and tumor progression by acting on microglial, glioma, and endothelial cells (fig 17). These findings emphasize the importance of gut-brain communication in glioblastoma pathophysiology and highlight the potential of targeting the gut microbiota and metabolome as a therapeutic strategy for glioma treatment. Future research should focus on elucidating the precise molecular pathways linking gut dysbiosis, metabolomic alterations, and glioma

progression, as well as exploring potential interventions to modulate the gut-brain axis in glioblastoma patients.

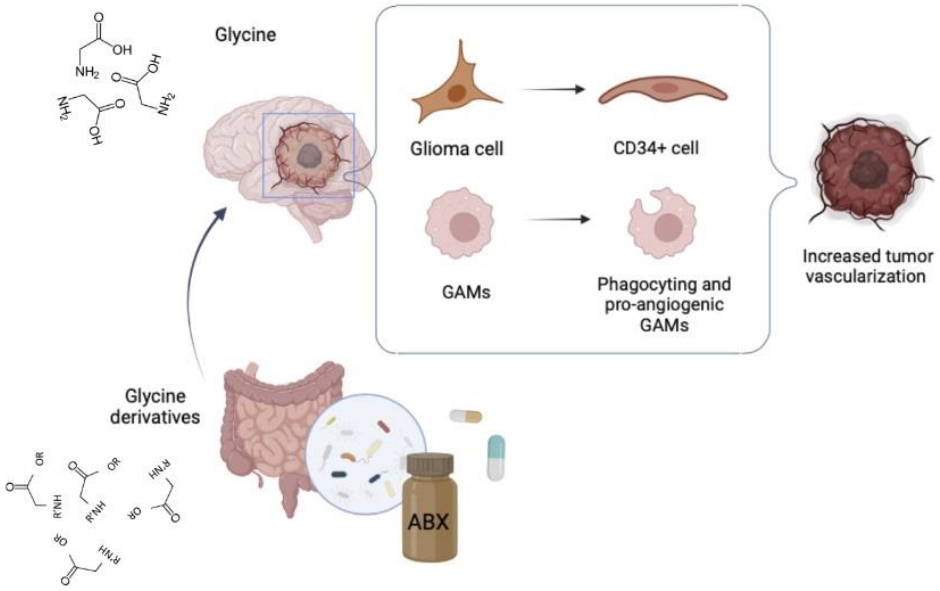

Figure 17: Mechanism of action; Dysbiosis induced by ABX promote tumor vascularization

Materials and methods

Animal husbandry

C57BL/6N mice were housed (two to four animals per cage) under a 12-h light cycle in standard cages, in autoclaved bedding and drinking water, and with sterilized standard chow ad libitum, and were randomly assigned to the different experimental groups. For CD68 immunofluorescence analysis and time-lapse imaging, $Cx3cr1^{+/gfp}$ mice were used (crossing B6.129P2(Cg)-Cx3cr1tm1Litt/J from Jackson Laboratory with C57BL6J). All the experiments in this study were conducted following the ARRIVE guidelines (Kilkenny et al., 2010), and were approved by the local animal welfare body and by the Italian Ministry of Health (authorization No. 231/2015PR) by the EC Council Directive 2010/63/EU and the Italian d.lgs.26/2014. All the efforts were done to minimize animal suffering, and to reduce the number of animals, calculating the necessary sample size before starting the experiments.

Tumor cells transplantation and ABX treatment

The glioma syngeneic mouse model (GM) are obtained by injecting glioma cells (GL261; CT2-a and GL261-rfp) as previously described (10). Mice were treated with not-absorbable ABX (0.5g/L vancomycin, AppliChem; [0.5g/L], gentamicin, Aurogene) and sucralose (0.5%) to improve palatability or with sucralose alone (control solution) in autoclaved water. ABX and control solutions were changed every 2 days and continuously administrated for two weeks before and three weeks after tumor injection.

Drug administration

GlyT1 inhibitor (BI-425809, Iclepertin) is administered by oral gavage to the mice (2.5mg/Kg, 0,3% DMSO), the drug is sonicated for 2 minutes soon before the oral gavage. Mice are treated every 4 days starting from the beginning of ABX administration and throughout the experimental setup. Mice that didn't receive the pharmacological treatment were subjected to oral gavage with the same volume of vehicle solution.

Tumor volume evaluation

Serial 20 μm coronal brain slices (one every 100 μm of the entire tumor length) were collected and stained by standard H&E protocol. Tumor volume was calculated according to the formula (volume = $t \times \sum A$), where A is the tumor area/slice and t is the thickness by ImageTool3.0 software.

Isolation of CD11b $^{+}$ cells and extraction of total RNA

Glioma bearing mice were anesthetized and perfused with PBS. Brains were removed, the ipsilateral brain hemisphere was cut into small pieces and single-cell suspension was achieved in Hank's balanced salt solution (HBSS). The tissue was further mechanically dissociated using a glass wide-tipped pipette and the suspension was applied to a 30 μm cell strainer (Miltenyi Biotec). Cells were processed immediately for MACS MicroBead separation. $CD11b^{+}$ cells were magnetically labeled with CD11b MicroBeads. The cell suspension was loaded onto a MACS Column placed in the magnetic field of a MACS Separator and the negative fraction was collected. After removing the magnetic field, $CD11b^{+}$ cells (which contain resident microglial cells but also infiltrating monocytes/macrophages, granulocytes, and natural killer cells) were eluted as a positive fraction. Total RNA was isolated with Tri-Reagent (Merck), and processed for real-time PCR. The quality and yield of RNAs were verified using the NANODROP One system (Thermo Scientific).

Slice preparation

Acute coronal brain slices were prepared from CTRL and ABX-treated $Cx3cr1^{+/gfp}$ mice (34) injected with GL261 cells, in chilled artificial cerebrospinal fluid (ACSF). The ACSF composition included the following concentrations in millimolar (mM): NaCl 125, KCl 2.3, $CaCl_2$ 2, $MgCl_2$ 1, $NaHPO_4$ 1, $NaHCO_3$ 26 and glucose 10. To maintain physiological pH, the ACSF was continuously oxygenated with a mixture of 95% O_2 and 5% CO_2. Using a slicer (7000 smz-2 Vibratome, Campden Instruments, UK), coronal slices with a thickness of 250 μm were cut at 4°C. Slices were then placed in a chamber filled with oxygenated ACSF and allowed to recover at room temperature (24–25°C) for at least 2 hours. All time-lapse recordings were conducted at room temperature on the submerged slices in ACSF. The recording chamber was perfused with the same ACSF solution at a rate of 1 ml/min while being observed under a microscope.

Time-lapse imaging in acute brain slices.

Microglia process rearrangement in acute striatal slices was assessed using time-lapse fluorescence imaging [56]. Throughout the experiment, the slices were continuously maintained in oxygenated ACSF at room temperature. Images were captured every 10 seconds for a duration of 50 minutes, with an exposure time of 200 ms, using an Olympus BX51WI microscope equipped with a LUMPlanF N 40×/0.80 (water immersion) objective (Olympus Corporation, Tokyo, JP). To excite the GFP signal at 488 nm, an Optoscan monochromator

(Cairn Research, Faversham, UK) was utilized. The light source was a xenon lamp Optosource (Cairn Research). A borosilicate glass micropipette filled with ACSF supplemented with 2 mM Mg-ATP (Merck) was positioned at the core of the recording field, within the peritumoral area, using a Sutter Instruments micromanipulator MP-225 (Novato, CA, USA). The pipette was placed approximately 50 µm beneath the surface of the slice to avoid reactive microglia.
The basal fluorescence was assessed for 5 min, then a small volume of Mg-ATP solution was applied to the recording field core using a pneumatic pico-pump (PV820; World Precision Instruments, Inc., Sarasota, FL, USA) with a brief pressure (8 psi; 100 ms). Images were acquired using a Photometrics CCD CoolSnap MYO camera (Tucson, AZ, USA) and analyzed using MetaFluor software. Fluorescence variations were measured in five concentric circular regions of interest (ROIs) positioned from the tip of the ATP pipette, with diameters of 10, 20, 40, 80, and 120 µm. The fluorescence signal was determined using the formula $(F-F_0)/F_0$, where F_0 represents the average fluorescence before ATP application.

Immunofluorescence staining on brain tissue and image acquisition

Mice were anesthetized with isofluorane 3% and transcardially perfused with cold PBS and 4% PFA in 0.1 M PB. Brains were rapidly removed, postfixed overnight in PFA 4%, washed with PB, and cryoprotected in PB 30% sucrose solution. We then collected 20 µm thick coronal sections with a cryostat microtome (Leica Microsystems) at 20°C. Briefly, slices were immersed for 30 min in a boiling citrate buffer solution for antigen retrieval, then incubated with blocking solution (0.5% Triton X-100, 5% BSA) for 1 h at RT. Sections were incubated with primary antibodies (CD34, RAM-34 ThermoFisher, 1:100; CD31, 28364 Abcam, 1:100; CD133, PA538014 ThermoFisher, 1:100; CD45 PA585429 ThermoFisher 1:100; GFAP MAB30060 Millipore 1:300; CD68 FA-11 eBioscience 1:100; Ki67 M3063 SP6 clone Spring Bioscience 1:50) in diluted blocking solution overnight at 4 °C and 1 h at RT with fluorophore-conjugated secondary antibodies (Alexa Fluor 488 goat anti-rabbit, 594 goat anti-mouse; Alexa Fluor 488 goat anti-rat; Alexa Fluor 594 goat anti-rat) and Hoechst for nuclei visualization. The sections were mounted with a fluorescence mounting medium (DAKO) or with ProLong Glass Antifade Mountant (Thermo Fisher).
Images were collected with spinning disk confocal microscopy on an Olympus IX73 microscope equipped with X-Light V3 spinning disk (CrestOptics), LDI laser source and a Prime BSI Scientific CMOS (sCMOS), 6.5 µm pixels (Photometrics) with a 60x/1.4 PlanApo l oil objective and 10x objectives. The used Z step size was 1 µm and 0.5 µm respectively for

10X and 60X objectives. All the images were acquired by using Metamorph software version 7.10.2. (Molecular Devices, Wokingham, UK) and then analyzed with ImageJ or Metamorph software (see Image preparation and analysis).

Image preparation and analysis

For image preparation, we used the open-source software ImageJ for adjustments of levels and contrast, maximum intensity projections, and thresholding signals for fluorescence intensity analysis. For vessel-like structure analysis, stack images were flattened in a maximum intensity 10um z-projection, and after removing the background noise, images were binarized allowing the count of the vessel-like structure identified considering a threshold of 100 um^2. For angiogenesis analysis, we used the angiogenesis analyzer plugin from image J.

For $GL261^{rfp}$ - $CD34^+$ colocalization study, after image thresholding, the single-plane confocal acquisition was analyzed by quantifying the percentage of colocalizing regions using Metamorph software.

Cell isolation and flow cytometric analysis

The study was conducted in accordance with the reported flow cytometry guidelines. Single-cell suspensions were obtained from GM and GM/ABX tumoral hemispheres. Mice were intracardially perfused with PBS and brains were rapidly removed, hemispheres separated, and placed into ice-cold HBSS. The hemispheres were disrupted in a glass-Teflon homogenizer and passed through a 100 μm nylon cell strainer (Becton- Dickinson). The suspension was centrifuged (800 *g*, 10 min, RT), and the pellet was resuspended in 8 mL of 30% Percoll (Sigma) and overlaid on the top of HBSS. The suspension was centrifuged (14 000 *g*, 15 min, RT), the pellet was washed with 10% FBS in HBSS, and cells used for flow cytometry or labeled with $CD11b^+$ microbeads and passed through MACS Columns (Miltenyi Biotec). For flow cytometry, cells were washed and suspended in a staining buffer (PBS with 0.5% BSA, 2mM EDTA, 0.025% NaN3). Zombie Violet™ Fixable Viability Dye from BioLegend was used to exclude dead cells and anti-CD16/32 (clone 2.4G2) was used to prevent nonspecific and Fc-mediated binding. Cells were stained with the following fluorochrome-conjugated mAbs (clone name indicated in parentheses) for 20 min at 4°C: CD45.2-APC-eFluor 780 (104), CD11b-APC (M1/70), Tmem119-Alexa Fluor™ 488 (V3RT1GOsz) from eBioscience TM - Invitrogen (ThermoFisher), CD34-PE (RAM-34) from eBioscience™. Samples were analyzed by a FACS-CantoII (BD Biosciences), and data was elaborated using FlowJo software v.10.7.1 (TreeStar, Ashland, OR, USA).

Sample Preparation for NMR analysis

Brain samples were rapidly frozen in liquid nitrogen, weighted and immediately extracted with a modified Bligh-Dyer protocol, using 2:2:1 ratio of chloroform, methanol and water, respectively. After 24 hours at 4°C, the samples were centrifuged at 11000 x g for 25 minutes. The top hydrophilic fraction (methanol-water) was then collected to a scintillation vial and then dried under nitrogen flux. Each sample have been subsequently resuspended in 0.7 mL of D_2O solution containing the internal standard 3-(trimethylsilyl)-propionic-2,2,3,3-d_4 acid sodium salt (TSP, 2 mM).

Frozen stools were combined with 1,2 mL of phosphate buffer (PBS)-D_2O-NaN_3 (0.5% v/v). Samples were thawed for 30 min at 25 °C and then vortexed to achieve a homogenous solution. The supernatant was separated from the solid phase through a first centrifugation at 10,000× g for 25 min at 4 °C, filtered on a 40 µm pores filter. After adding 200 µL of PBS-D_2O with 0.3% of NaN_3, the samples were centrifuged again at 10,000× g for 25 min at 4 °C. 600 µL of supernatants were added to 60 µL of PBS-D_2O-TSP (2 mM, final concentration).

NMR acquirement and processing

^1H experiments:

The NMR ^1H monodimensional spectra were recorded at 25°C on a JEOL ECZR JNM spectrometer operating at the proton frequency of 600.13 MHz. Spectra were acquired collecting 128 scansions for each sample using a calibrated 90° detection pulse length of 8.3 µs, 64k data points and a spectral width of 15 ppm. Presaturation has been employed for water signal suppression and the relaxation delay have been set to 7.723 s, in order to achieve a 15 s of total acquisition time, guaranteeing complete resonance relaxation between following scansions.

Spectra have been processed by applying an exponential window function with a line broadening factor LB=0.3 Hz. After applying the Fourier transformation, spectra have been manually phased and base corrected by applying the BCFR protocol. Metabolites quantitation has been carried out by comparing the integrals of specific resonances with the one of the internal standards and normalized by the number of protons. Data from brain and liver have been expressed as µmol/g, for fecal water metabolites concentration as nmol/g.

Bidimensional experiments:

To univocally identify the metabolites in the biological samples, bidimensional experiments ^1H-^1H Total Correlation Spectroscopy (TOCSY) and ^1H-^{13}C Heteronuclear Single Quantum

Correlation (HSQC) and Heteronuclear Multiple Bond Correlation (HMBC) were performed on selected samples. TOCSY experiments were conducted with a spectral width of 9,025 Hz in both dimensions, a data matrix of 8,192 × 256 points, a mixing time of 80 ms, and a relaxation delay of 2 s. HSQC experiments were performed with spectral widths of 9,025 KHz and 37,764 KHz for the proton and carbon, respectively, a data matrix of 8,192 × 256 points and a recycle delay of 2 s. HMBC experiments have been acquired with a spectral width of 9,025 KHz and 37,764 KHz for the proton and carbon, respectively, with a data matrix of 8 K × 256 points, long-range constants nJC–H of 4, 8, and 12 Hz, and a recycle delay of 3 s.

Microglia primary cultures and cell treatment

Microglia cells are obtained as previously described. In detail, cortical glial cells were prepared from 0- to 2-d-old mice: cerebral cortices were chopped and digested in 30 U/ml papain for 40 min at 37°C followed by gentle trituration. The dissociated cells were washed, suspended in DMEM with 10% FBS (Invitrogen) and 2 mM L-glutamine, and plated at a density of 9–10 x 10^5 in 175 cm2 cell culture flasks. At confluence (10 –14 DIV), glial cells were shaken for 2 h at 37°C to detach and collect microglial cells. After seeding, cells were treated for 48h with Glycine (300μM) in the presence of glioma glioma-conditioned medium (GCM). GCM is collected from GL261 ($1x10^6$ cells in 1 ml of DMEM -FBS).

Cell lines and treatments

The GL261 murine glioma cells (provided by Dr. Michela Matteoli Humanitas Milan) were cultured in DMEM supplemented with 20% FBS. Glycine was purchased from MERCK, and treatment (300μM) was provided in Minimum Essential Medium (w/o FBS) for 72 h. After stimulation cells were harvested and total RNA was isolated with Tri-Reagent (Merck) and processed for real-time PCR. The quality and yield of RNAs were verified as above. bEnd.3 cells were seeded in DMEM 10% FBS at the density of 10^4cells/cm^2, stimulated with glycine (150-300 μM) and after 8 h treatment cells were fixed and stained with phalloidin for vessel-like structure analysis (see image analysis section).

MTT assay

After glycine treatments, MTT (dissolved in PBS with a final density of 0.5 mg/ml) was added to the medium culture. After 2h incubation, the MTT solution was extracted, mixed with DMSO, and shaken for 20 min. Finally, the absorption of the samples was read by regulating

the 570-nanometer filter as the main wavelength and the 630-nanometer filter as the referenced wavelength. Blank was subtracted from all samples to obtain pure cellular absorption.

BrdU Cell Immunostaining

GL261 cells were grown on glass coverslips at a density of 5 x 10^4 cells/cm^2 and treated for 6 days with Glycine 300 µm or vehicle. Cells were then incubated with 10 µg/ml BrdU for 30 min, washed with PBS, and fixed in 4% paraformaldehyde for 15 min. Fixed cells underwent immunostaining protocols as described for brain sections. Hoechst was used for nuclear staining. BrdU-positive cells were counted out of 800 cells for condition.

Real time PCR

Samples were lysed in TRYzol reagent for isolation of total RNA. The quality and yield of RNAs were verified using NANODROP One (Thermo Scientific). For RT-PCR one microgram of total RNA was reverse transcribed using ThermoScript RT-PCR System. RT-PCR was carried out using Sybr Green (Bio-Rad) according to the manufacturer's instructions. The PCR protocol consisted of 40 cycles of denaturation at 95 ◦C for 30 s and annealing/extension at 60 ◦C for 30 s. For quantification, the comparative Threshold Cycle (Ct) method was used. The Ct values from each gene were normalized to the Ct value of GAPDH in the same RNA samples. Relative quantification was performed using the $2^{-\Delta\Delta Ct}$ method [2] and expressed as fold change in arbitrary values. Oligos used for gene expression are listed in table 3.

Table 3- List of oligoes

Gene name	Primer Sequence 5'- 3'
GAPDH_forward	TCGTCCCGTAGACAAAATGG
GAPDH_reverse	TTGAGGTCAATGAAGGGGTC
Chil3_forward	CAGGTCTGGCAATTCTTCTGAA
Chil3_reverse	GTCTTGCTCATGTGTGTAAGTGA
Tnfα_forward	GTGGAACTGGCAGAAGAG
Tnfα_reverse	CCATAGAACTGATGAGAGG
il1β_forward	GCAACTGTTCCTGAACTCAACT
il1β_reverse	ATCTTTTGGGGTCCGTCAACT
nos2_forward	ACATCGACCCGTCCACAGTAT

nos2_reverse	CAGAGGGGTAGGCTTGTCTC
Mrc1_forward	CAAGGAAGGTTGGCATTTGT
Mrc1_reverse	CCTTTCAGTCCTTTGCAAGT
P2ry12_forward	CCTGTCGTCAGAGACTACAAG
P2ry12_reverse	GGATTTACTGCGGATCTGAAAG
P2ry6_forward	GTGAGGATTTCAAGCGACTGC
P2ry6_reverse	TCCCCTCTGGCGTAGTTATAGA
Arg1_forward	CTCCAAGCCAAAGTCCTTAGAG
Arg1_reverse	AGGAGCTGTCATTAGGGACATC
cd86_forward	AGAACTTACGGAAGCACCCA
cd86_reverse	GGCAGATATGCAGTCCCATT
Vegfa_forward	GATCATGCGGATCAAACCTC
Vegfa_reverse	AATGCTTTCTCCGCTCTGAA
Mmp9_forward	TAGCTACCTCGAGGGCTTCC
Mmp9_reverse	GTGGGACACATAGTGGGAGG
cd68_forward	GGGCCATGTTTCTCTTGCAA
cd68_reverse	AGTCAGTGGCATGGTGAAGA
cd133_forward	TGCCACCCCAACTAGAAGAG
cd133_reverse	TCGCAGAGCAACTTTTCCAC
Nestin_forward	AGGTGTCAAGGTCCAGGATG
Nestin_reverse	AAGGAAGCAGACTCAGACCC
cd34_forward	CAGGAGAAAGGCTGGGTGAA
cd34_reverse	GTTGTCTTGCTGAATGGCCG
Olig2_forward	CCCCAGAACCCGATGATCTT
Olig2_reverse	GGTGCTGGAGGAAGATGACT
cd44_forward	ACCTTGGCCACCACTCCTAA
cd44_reverse	GCAGTAGGCTGAAGGGTTGT
Sox2_forward	AGGAGAGAAGTTTGGAGCCC
Sox2_reverse	TCTGGCGGAGAATAGTTGGG

Statistical analysis

The repeat (n) for each experiment and details of statistical analyses are described in the figure legends or main text. Data are reported as mean ± SD. Statistical analysis, normality tests and non-parametric tests were performed, when appropriate, with GraphPad Prism 9 software. The exact p-values are indicated in the text where available and the multiplicity-adjusted p-values are indicated in the corresponding figures (*$p < 0.05$, **$p < 0.01$, ***$p < 0.001$). Paired T-test is used to compare tumor volume and FACS analysis; an unpaired T-test is used for immunofluorescence analysis. For real-time PCR a Mann–Whitney U test was run to determine significant differences for the considered genes.

The in vitro angiogenesis assay (number of cells, junction, and total meshes area) was analyzed by one-way ANOVA followed by Dunnett's multiple comparison test. For time-lapse imaging of microglia process rearrangement, a Mann-Whitney test is used to determine significant differences in fluorescence variation. For NMR metabolomic analysis Supervised Partial Least Square (PLS) analysis have been carried out on the auto scaled data, building the model in respect to predictors Y, in order to identify the significant variables for the categorization. For the model validation, a full-cross validation method has been applied, employing as diagnostic statistics R^2, which is a measure of data fitting, Q^2, which is the measure of predictive relevance of the model and the receiver operator characteristics (ROC) values, which measures the specificity and sensitivity of the model.

In order to identify the most significant variables for the model, the Variables Important in Projection (VIP) indexes have been inspected. Variables with a VIP score greater than 1 are considered important for the projection of the PLS regression model. Statistics was carried out employing MatLab 2023a (the MathWorks, Natick, MA) employing in house written functions

Personal contribution to the project

To provide clarity, I will summarize the details of my contribution to this project by categorizing all conceptual, experimental, and analytical tasks into three distinct levels, as follows:

I was the main contributor:

- Animal handling and feeding
- Tumor cell transplantation & ABX treatment
- Oral gavage to the mice
- Tumor volume evaluation

- RNA extraction
- MTT Assay
- Immunofluorescence staining
- Primary culture
- Cell lines and treatmemts

I collaborated on the tasks:

- Isolation of CD11b $^{+}$ cells
- Sample preparation for flow cytometric analysis
- Image preparation and analysis
- Sample Preparation for NMR analysis
- Real time PCR

Tasks performed by others:

- Time lapse imaging
- Flow cytometric analysis
- NMR acquirement and processing

Part II: Ketogenic diet induces an inflammatory reactive astrocytes phenotype reducing glioma growth

Introduction

In recent years, scientific interest in the use of the ketogenic diet (KD) as a complementary approach to standard glioma therapy has grown. Emerging preclinical and clinical evidence suggests that the KD may exert therapeutic benefits in glioma, by enhancing the sensitivity of glioma cells to conventional treatments like chemotherapy and radiotherapy, potentially prolonging survival rates. Moreover, the KD's ability to influence systemic metabolic parameters, such as reducing blood glucose levels and elevating ketone body concentrations, provides an additional therapeutic benefit. These findings highlight the KD as a multifaceted approach that not only targets the metabolic vulnerabilities of glioma cells but also works synergistically with existing therapeutic modalities [57,58].

The ketogenic diet (KD) is a category of restrictive diets distinguished by having hyper-lipid, normal-protein, and hypo-carbohydrate contents. The different types of KD can be discerned based on the macronutrient ratio [59]. This restrictive diet can reproduce what occurs during fasting, in other words, a reduction of glycemia that brings to an increase of the systemic concentration of ketone bodies (KB): when lacking glucose, the organism falls back on the β-oxidation of fatty acids to assure the production of the Acetyl-CoA needed for TCA cycle; being oxaloacetate a limited quantity, when the TCA cycle is saturated, the cytoplasmic excess of Acetyl-CoA enters a hepatic pathway that will lead to the production of ketone bodies – such as β-hydroxybutyrate (β-HB), acetoacetate and acetone that can reach the bloodstream and be useful to the CNS as energy substrates [60,59] (fig.18).

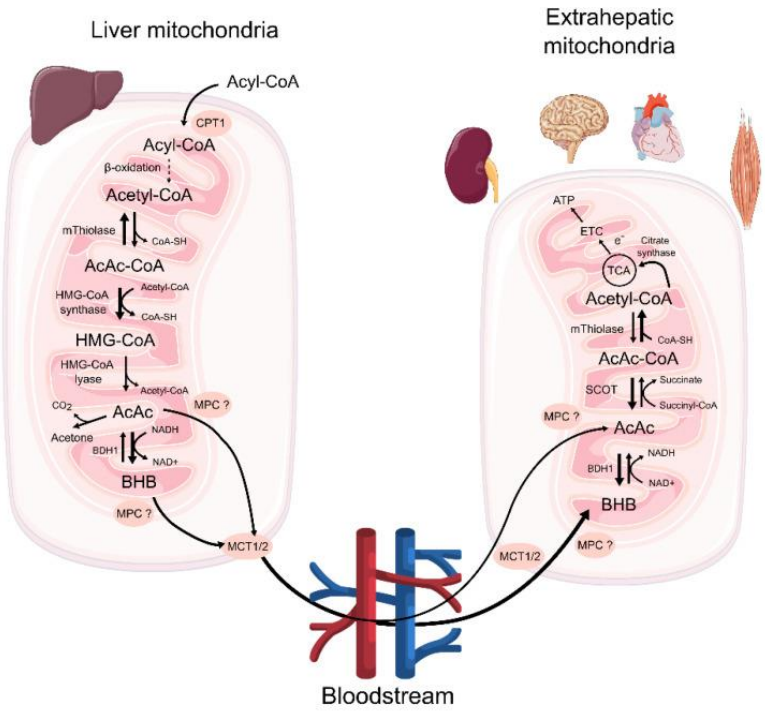

Figure 18: Ketone bodies metabolism, Makievskaya et al; "Ketogenic Diet and Ketone Bodies against Ischemic Injury: Targets, Mechanisms, and Therapeutic Potential" ***International Journal of Molecular Sciences (2023).***

Many studies suggest that GBM cells, are not able to use KB as an energy source, relying only on glucose to sustain their cellular metabolism [59,61]. Nonetheless, KB still enters inside GBM cells through the same monocarboxylate transporters (MCT) that are used to export lactate outside the cells. Therefore, it is supposed that KB can carry out a competitive action on lactate, causing its intracellular increase that affects cellular survival. In addition, since lactate has an anti-inflammatory effect on microglia, polarizing them towards an M2 phenotype related to tumor progression, the depletion of extracellular lactate may influence the stromal cells to fight cancer better [1].

Recent studies have highlighted the interplay between metabolic reprogramming in tumor cells and the surrounding microenvironment, suggesting that adjuvant treatments such as a controlled KD may also modulate the activity of microglia and astrocytes, potentially influencing glioma progression [14]. Studies have shown that the KD leads to a shift in astrocyte metabolism towards increased utilization of ketone bodies, such as β-HB, as a fuel source alternative to glucose [62]. This metabolic adaptation enhances astrocytic energy production improving the levels of mitochondrial performance in glia and neurons thereby promoting 5neuronal survival and function under conditions of metabolic stress [63]. Additionally, beyond

its metabolic effects, emerging evidence suggests that β-HB is a signaling metabolite and a powerful epigenetic molecule in the brain through direct and specific histone marks remodeling and also regulates proteostasis [64] (fig.19). It has been reported that in response to the KD, microglia may adopt an anti-inflammatory phenotype, which in principle could contribute to their pro-tumoral effect [28].

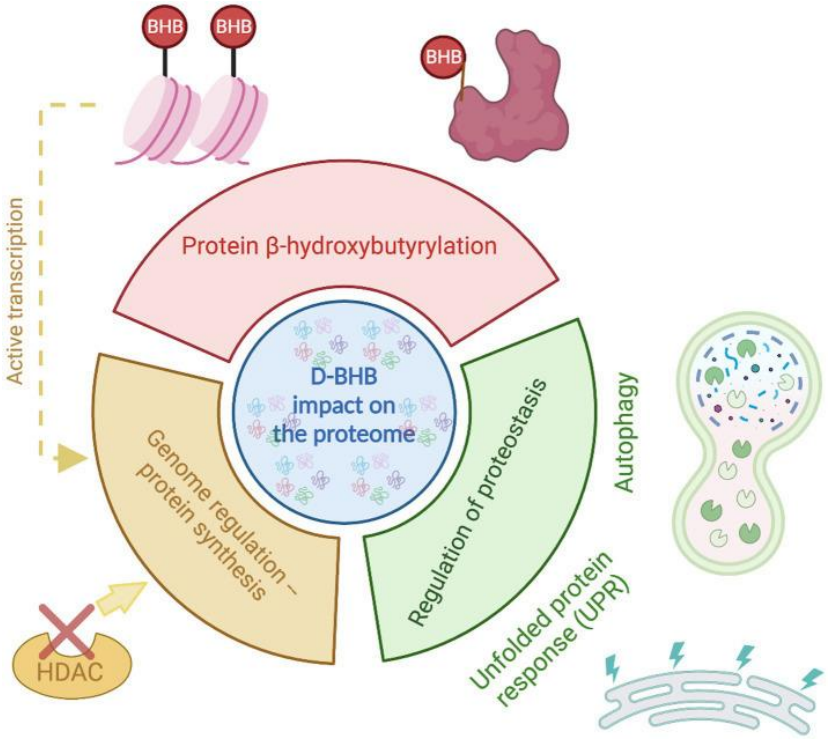

Figure 19: Beneficial effects of β-HB, Velazque t al; "The proteomic effects of ketone bodies: implications for proteostasis and brain proteinopathies" ***Frontiers in Molecular Neuroscience (2023).***

In the presence of GBM, reactive astrocytes are enriched in the peri tumor area, forming the so-called "glial scar" that has a double purpose: it contains and isolates the damage, but, in a maladaptive interplay, it also complicates repairing mechanisms and, with different strategies, preserves the tumor from the attacks of the immune system or from the effects of the treatment [65]. In this stage astrocytes are GFAP+ and Nestin+ and present a round shape body. Moreover, with the progression of cancer, astrocytes acquire a pro-tumor effect promoting cancer cells' proliferation, and their ability to maintain the BBB is undermined by GBM cells: astrocytes and pericytes are no longer connected, allowing cancer cells inside the vascular vessels, promoting tumor invasiveness. In this stage, astrocytes are still GFAP+, but there is a change in morphology, going from fibrous to star shape, with longer processes and an increase in

dimensions [66,67]. Once again Virtuoso et al. summarize in their review the changes in astrocytes' metabolism. Physiologically, astrocytes employ glycolysis to produce lactate for the neurons while engaging mitochondrial OXPHOS for ATP. Astrocytes are able to modify their mechanisms of energy production according to local environmental demands: GBM cells require more energy and, since they use glucose as their substrate of choice, the following glucose starvation determines the initiation of glycogenolysis on behalf of astrocytes; moreover, astrocytes provide GBM with ATP and glutamine, which is used within the TCA cycle to produce energy. When glucose is lacking, healthy astrocytes can fuel themselves with alternative sources of energy using glutamate for gluconeogenesis or ketone bodies (KB) for ketolysis, which seems to be related to anti-angiogenic, anti-inflammatory and pro-apoptotic effects on the tumor. Zhang et al. reported that astrocytes surrounding glioblastoma have an increased proliferation which is comparable to fetal astrocytes; however, Henrik Heiland et al. reported that it is only in the presence of GBM and microglia that astrocytes are activated and anti-inflammatory cytokines are secreted, giving GBM the typical characteristic of a cold tumor.

The most abundant ketone body in the body is β-HB [68], plays a crucial role in both energy metabolism and neuroprotection. Research has demonstrated that β-HB enhances the ability of astrocytes to uptake glutamate, mitigating excitotoxicity caused by excessive glutamate concentrations, which is a common pathological feature in neurodegenerative and neuroinflammatory conditions. Specifically, β-HB has been shown to improve astrocytic glutamate absorption, thereby partially restoring neuronal viability impaired by glutamate-induced damage. This protective mechanism highlights the metabolic adaptability and resilience fostered by β-HB [69]. Additionally, β-HB plays a pivotal role in modulating astrocytic and neuronal functions, particularly through its influence on the release of S100B, a protein with well-documented neurotrophic properties. At nanomolar concentrations, S100B supports neuronal health by promoting synaptic plasticity and regulating neuronal excitability. This neurotrophic factor is critical for maintaining neural homeostasis and adaptive responses within the CNS. β-HB has been shown to significantly enhance the release of S100B from astrocytes, independent of other cellular changes, suggesting a direct regulatory effect. Furthermore, β-HB induces pronounced alterations in astrocyte morphology, reshaping their cellular structure and potentially affecting their functional interactions with neurons. These changes in astrocytic physiology, including the increased extracellular availability of S100B, are hypothesized to contribute to the observed reductions in neuronal excitability under ketogenic conditions [70].

Here, we investigated the effect of KD and β-HB in glioma-bearing mice, showing a reduction in tumor growth and an increased median survival rate with respect to mice fed with a matched control diet (CD). To explore a possible mechanism by which KD might exert its function, we performed co-culture experiments, showing that glial cells act as mediators of the KD effect on tumor growth.

Specifically, we describe that GL261 glioma cells are not able to use β-HB as an energetic fuel, and their proliferation rate has slowed down by the presence of the pro-inflammatory astrocytes induced by the β-HB treatment. In addition, we showed that pro-inflammatory astrocytes isolated from the glioma-bearing mice or induced by the β-HB treatment, exhibit increased expression of glutamate transporters and are functionally active in reducing the extracellular glutamate level. Moreover, we described increased intracellular basal Ca^{2+} levels in GL261 treated with β-HB or co-cultured with astrocytes. All these data suggest that β-HB, triggering a pro-inflammatory astrocytes phenotype, can reduce glioma proliferation, counteract excitotoxicity, and dysregulate Ca^{2+} homeostasis of glioma cells thus proving a beneficial effect on brain parenchyma.

Results

The ketogenic diet in glioma bearing-mice reduces tumor volume and improves mice survival:

Here we investigated the effect of a restricted ketogenic diet (KD) on glioma-bearing mice (Fig. 20A). During the dietary regimen, the mice's body weight was constantly monitored showing a significant reduction in KD versus control diet (CD) treated-mice starting from the day 6 after tumor implantation. After an initial decrease in body weight of KD-treated mice, the weight stabilizes and remains constant during the experimental timeline and never falls below 12-13% of the original mice weight (Fig. 20B). Since KD induces changes in the metabolic state in mice, to test the efficacy of this special dietary regimen, we evaluated the glucose and β-HB blood levels. At day 14 after tumor implantation, KD mice exhibit a reduction in plasma glucose (Fig. 20C, left) and an increase in plasma β-HB level (Fig. 20C, right) respect to CD mice. Three weeks after tumor injection, a reduction in tumor volume was also observed in KD mice (KD: 14.88 ± 3.8, CD: 25.62 ± 6.5 mm^3 *p=0.031) (Fig. 20D), as well as an increase in KD mice survival (KD: 29, CD: 24 median survival days) (Fig. 20E). Moreover, immunofluorescence staining for Ki67 showed a reduced cellular proliferation in the tumor core of KD mice compared to control mice (KD: 3.85 ± 0.7 CD: 7.53 ± 1.26) (Fig. 20E, F). These data confirm that KD effectively reduces glioma growth and increases mice survival.

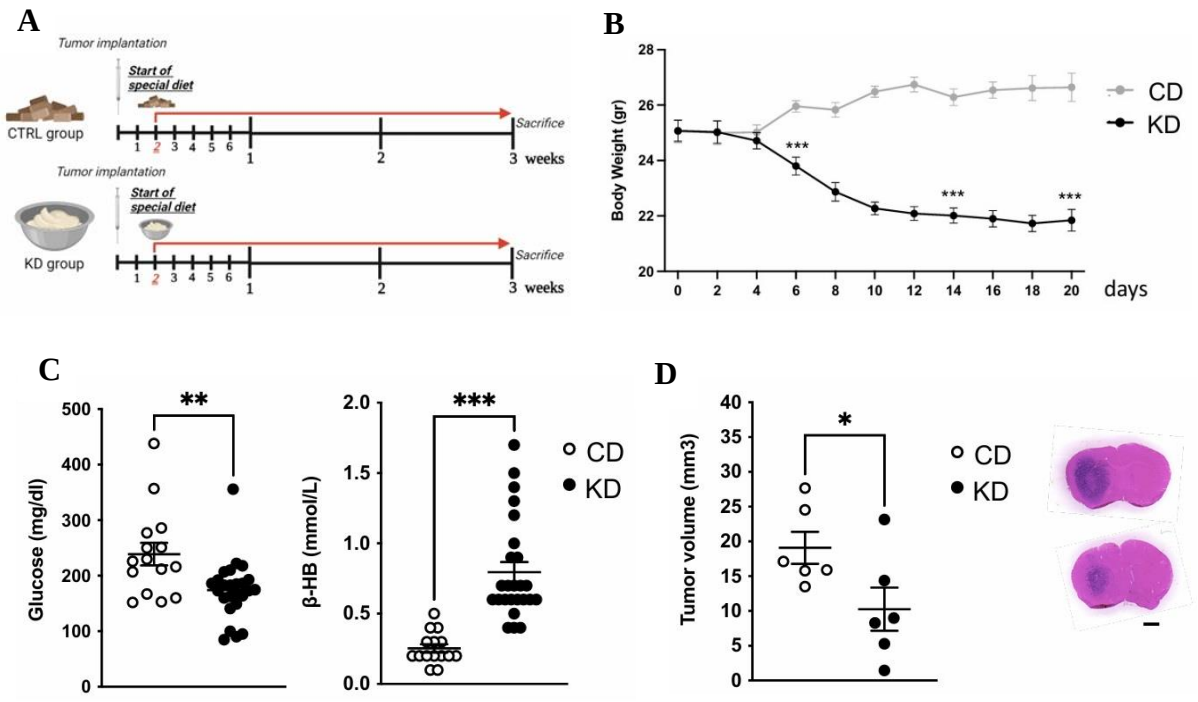

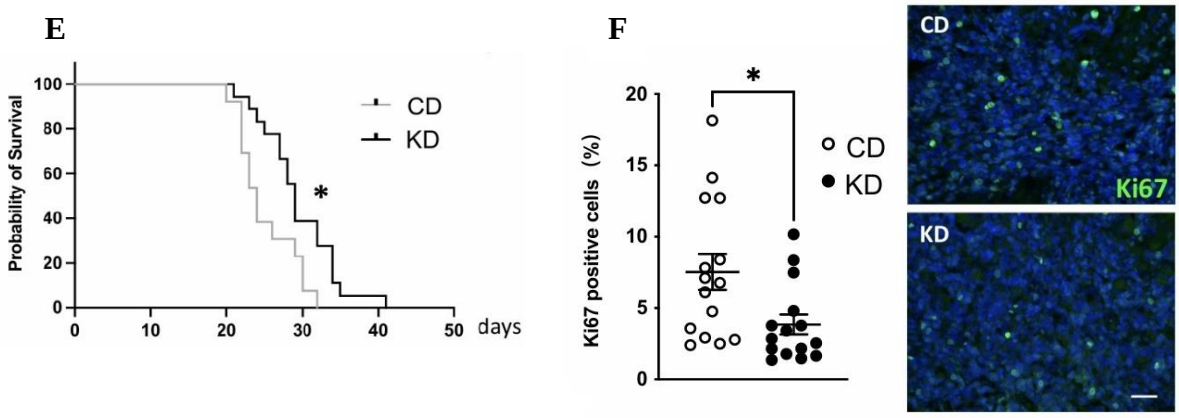

Figure 20: (A) Study design (**B)** Body weight measurements of CD and KD GL261 bearing mice. Data are presented as the mean ± SEM ***p <0.001 Student's t-test evaluated on days 6, 14, and 20. **(C)** Dot plot showing the blood glucose and β-HB level of CD and KD mice measured at day 14 after tumor injection. Data are presented as the mean ± SEM **p <0.005, ***p <0.001 Student's t-test. **(D)** Tumor size in CD and KD mice, *n* = 6, pooled from two experiments, three animals per group. Data are presented as the mean ± SEM *p <0.05, Student's t-test. Right pictures: Representative images of brain coronal slices, scale bar = 1 mm. **(E)** Kaplan–Meier survival curves of CD and KD GL261 bearing mice, *p =0.012, Log-rank test. **(F)** Dot plot showing the percentage of Ki67 positive cells in the tumor core area (CD: 15/3 slices/mice; KD: 15/3 slices/mice) Data are presented as the mean ± SEM *p <0.05, Student's t-test. (Left) Representative images of Ki67 (green) in CD and KD tumor core area. Hoechst staining (blu) for nuclei visualization; scale bar: 50 μm.

Glioma growth is not directly affected by β-HB:

Since KD results in β-HB production that can be oxidized as a brain fuel [71], we first tested the effect of this ketone body on glioma growth. We found that the intraperitoneal β-HB administration in mice can reduce tumor volume, thus mimicking the effect of the ketogenic diet (β-HB: 7.12 ± 1.18, saline: 16.72 ± 1.5mm^3) (Fig. 21A). To investigate the mechanisms involved in the β-HB-induced reduction of glioma growth, we tested its effects on glioma and non-neoplastic glial cells. We first report that *in vitro*, β-HB does not change the GL261 (Fig. 21B) viability since the proliferation rate during the in vitro culture is not affected. Similar results were obtained on a different murine glioma cell line, CT2A (Fig. 21C). We decided to use the 10mM β-HB concentration for all the in vitro experiments. Therefore, we measured the glucose and β-HB consumption of glioma cells in culture. While the glucose level is significantly reduced to the initial (time 0) concentration, without any differences between ctrl and β-HB treatment (Fig. 21D), the β-HB level remains constant (Fig. 21E). In addition, the transcriptional level of monocarboxylate transporters (Fig. 21F) and of β-HB converting

enzymes (Fig. 21G), evaluated at 72 h of β-HB treatment, are not modulated, indicating that GL261 cells are not using or converting β-HB to generate energy.

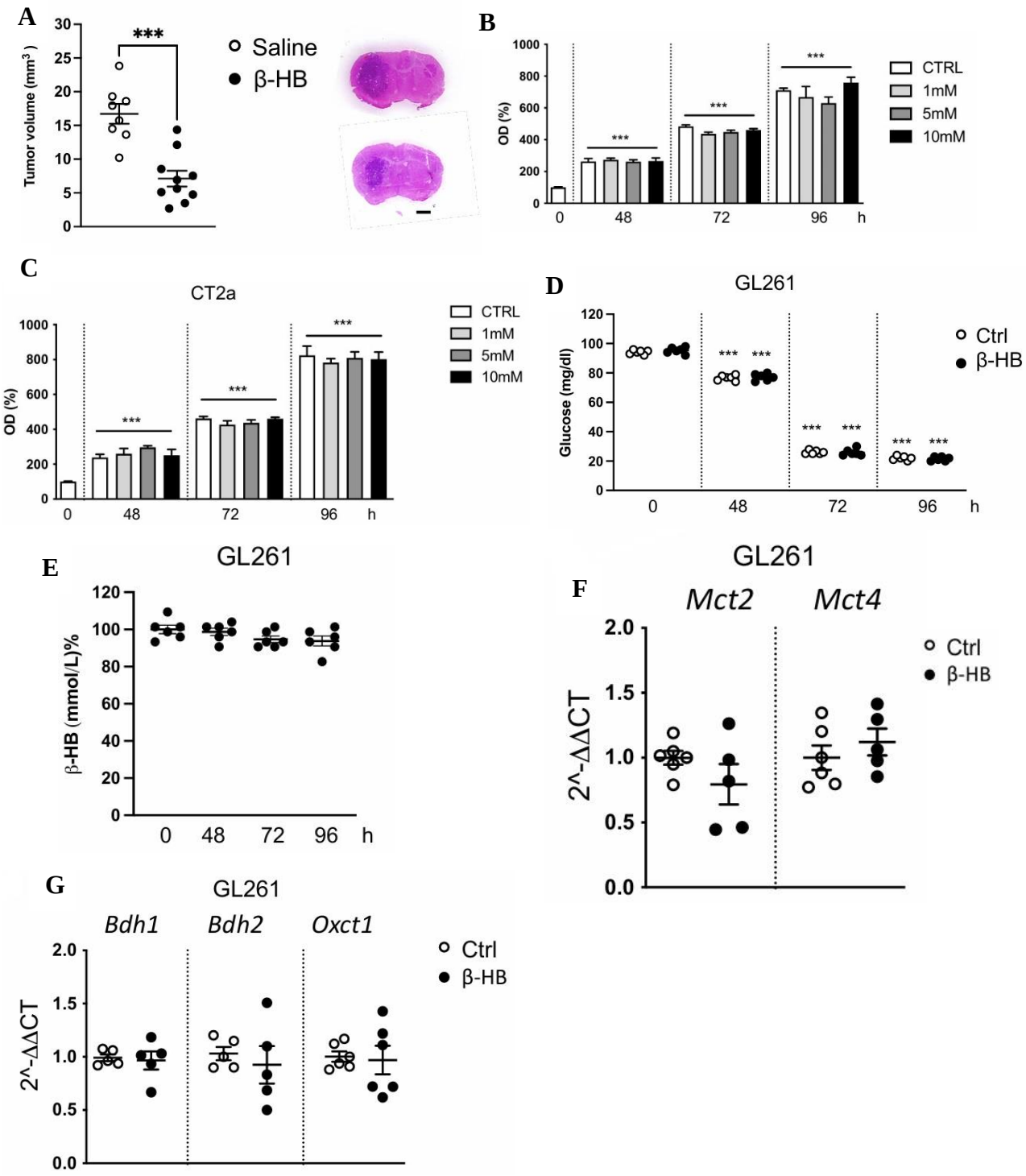

Figure 21: (A) Tumor size in saline and β-HB injected mice, *n* = 8-10 animals per group. Data are presented as the mean ± SEM ***p <0.001, Student's t-test. Right pictures: Representative images of brain coronal slices, scale bar = 1 mm. **(B)** Bar plot showing the MTT assay on GL261 cells stimulated with different β-HB concentrations. Data are presented as the mean ± SEM *** p < 0.001. One-way ANOVA - Dunnett's multiple comparison test versus time 0.

(C) Bar plot showing the MTT assay on CT2a cells stimulated with different β-HB concentrations Data are presented as the mean ± SEM *** p < 0.001. One-way ANOVA - Dunnett's multiple comparison test versus time 0. **(D)** Glucose consumption by GL261 cells without (white dots) or in the presence of β-HB (black dots). Data are presented as the mean ± SEM *** p <0.001. One-way ANOVA - Dunnett's multiple comparison test. **(E)** β-HB consumption by GL261 cells. Data are presented as the mean ± SEM. **(F)** RT-qPCR from GL261 mRNA. Gene expression of Mct2 and Mct4 is normalized to the housekeeping gene Gapdh, n = 6 to 7 samples pulled from 3 independent experiments. Data are presented as the mean ± SEM. **G)** RT-qPCR from GL261 mRNA. Gene expression of Bdh1, Bdh2, and Oxct1 is normalized to the housekeeping gene Gapdh, n = 6 to 7 samples pulled from 3 independent experiments. Data are presented as the mean ± SEM.

In the hypothesis that the effect observed in vivo could be mediated by non-tumor cells, we focused on astrocytes because these cells have important roles in shaping the glioma microenvironment [72], but their role during ketosis is still unexplored. We investigated the effect of β-HB on astrocyte proliferation and found that upon 72 and 96 h of treatment, astrocytes exhibit an increased proliferation that is further enhanced in the presence of glioma-conditioned medium (GCM) (Fig. 22A). Parallel to this increased astrocytic proliferation rate, we measured a significant reduction of β-HB level at 72 and 96 h of astrocyte cultures, already appreciable at 48 h when astrocytes were exposed to GCM (Fig. 22B). The transcriptional levels of monocarboxylate transporters (Fig. 22C) and β-HB converting enzymes (Fig. 22D), evaluated at 72 h of β-HB treatment, are not modulated.

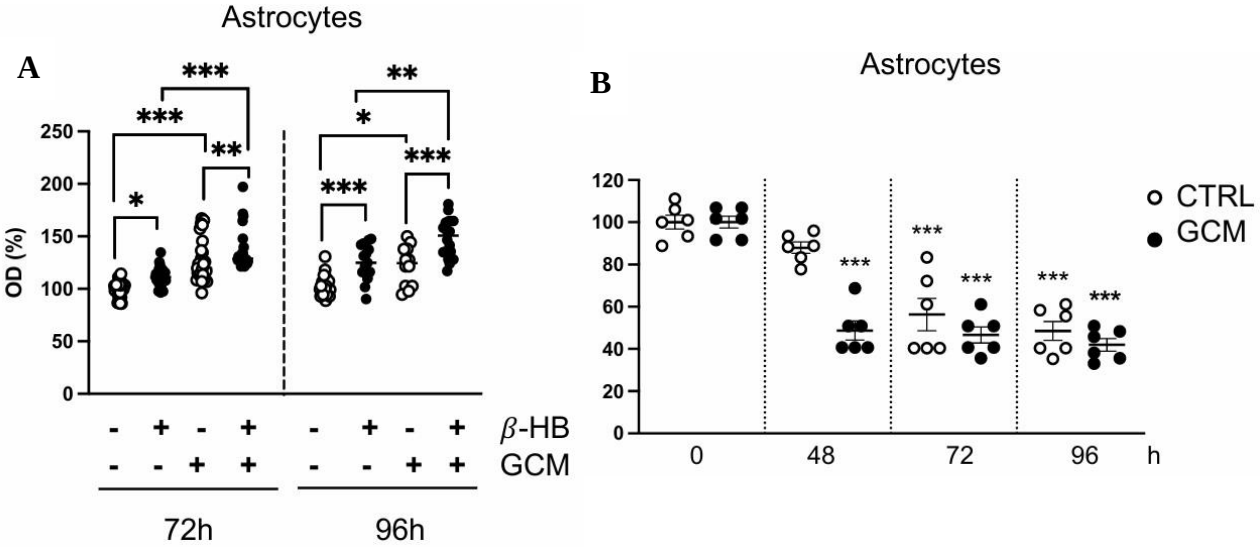

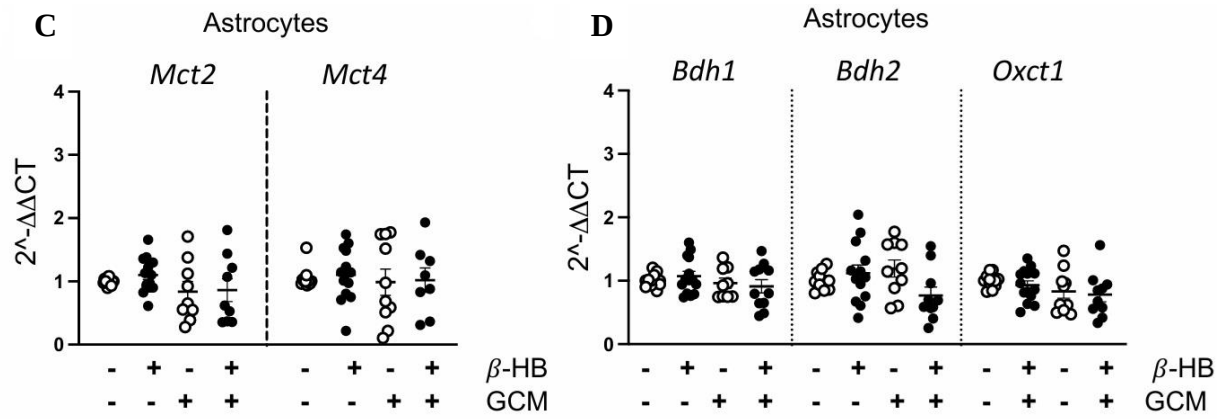

Figure 22: (A) MTT assay on astrocytes cultured with or without GCM and β-HB for 72 and 96 h of treatments. Data are presented as the mean ± SEM * $p < 0.05$ ** $p < 0.005$ *** $p < 0.001$ Two-way ANOVA. Fisher's LSD test. **(B)** β-HB consumption by astrocytes without (CTRL, white dots) or in the presence of GCM (black dots). Data are presented as the mean ± SEM *** $p < 0.001$. One-way ANOVA - Dunnett's multiple comparison test. **(C)** RT-qPCR from astrocytes mRNA. Gene expression of Mct2 and Mct4 and (**D)** Bdh1, Bdh2, and Oxct1 are normalized to the housekeeping gene Gapdh, n = 6 to 7 samples pulled from 3 independent experiments. Data are presented as the mean ± SEM.

We also tested the β-HB effect on microglia proliferation, appreciating a significant increase in proliferation only in the presence of GCM at 48 and 72 h of treatment (Fig. 23A), in addition to consumption of β-HB in the culturing medium (Fig. 23B), Paralleled by the increased transcriptional level of monocarboxylate transporters (Fig. 23C) and β-HB converting enzymes (Fig. 23D).

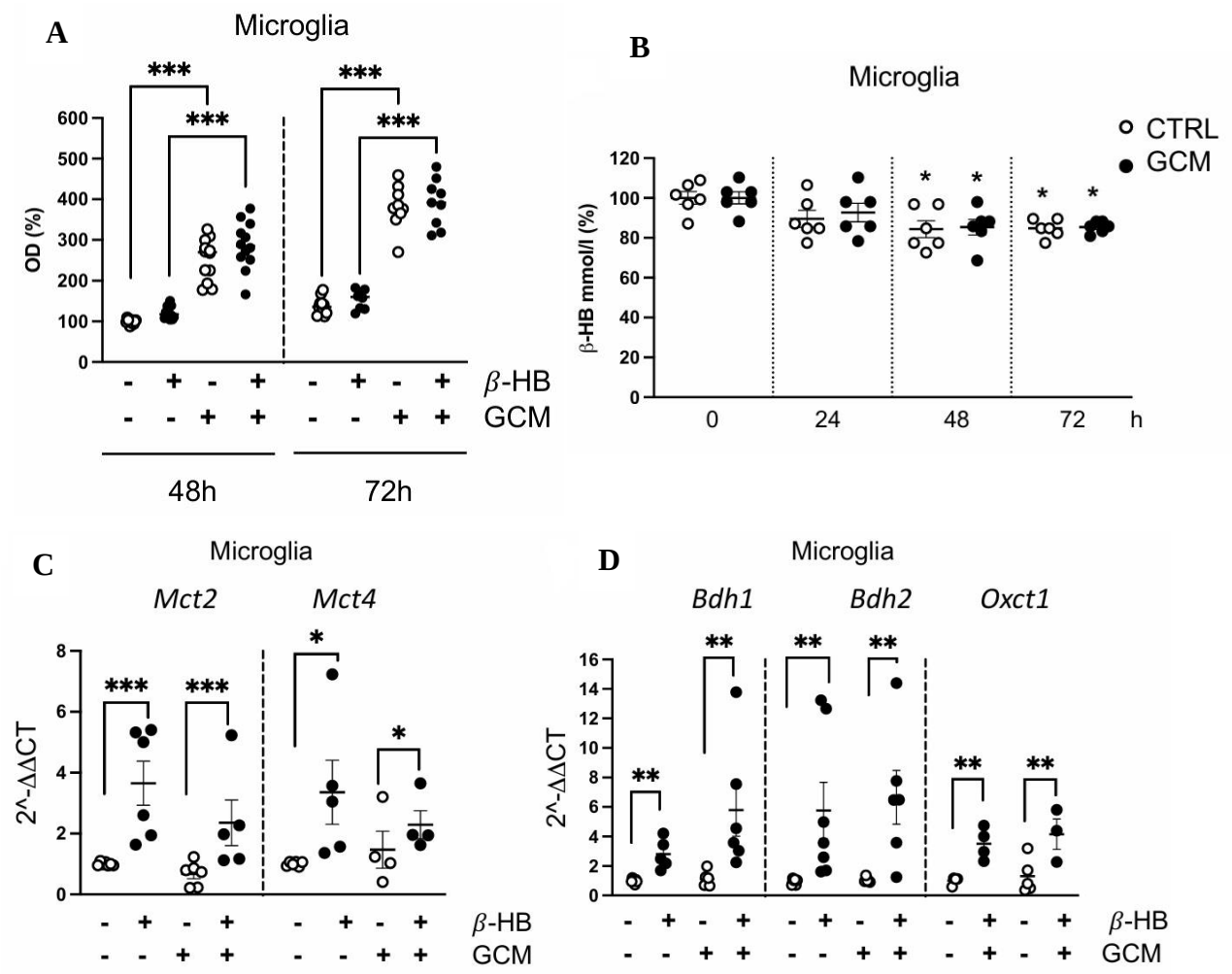

Figure 23: (A) MTT assay on microglia cultured with or without GCM and β-HB for 48 and 72 h of treatments. Data are presented as the mean ± SEM *** $p < 0.001$ Two-way ANOVA. Fisher's LSD test. **(B)** β-HB consumption by microglia without (CTRL, white dots) or in the presence of GCM (black dots). Data are presented as the mean ± SEM * $p < 0.05$. One-way ANOVA - Dunnett's multiple comparison test. **(C)** RT-qPCR from microglia mRNA. Gene expression of Mct2 and Mct4 and **(D)** Bdh1, Bdh2, and Oxct1 are normalized to the housekeeping gene Gapdh, n = 4 to 7 samples pulled from 3 independent experiments. Data are presented as the mean ± SEM * $p < 0.05$ ** $p < 0.005$ *** $p < 0.001$ Two-way ANOVA. Fisher's LSD test.

These data suggest that GCM is inducing an increased proliferation of astrocytes and microglia and that only in astrocytes β-HB treatment is further boosting the proliferation rate.

Astrocytes acquired a pro-inflammatory phenotype upon KD and β-HB administration:

Since astrocytes can consume β-HB in cultures and are responsive to this ketone body treatment by increasing the proliferation rate, we investigated the astrocyte reactivity in glioma-bearing mice treated with the KD. By immunofluorescence staining, we describe an increased GFAP staining in the peritumoral area of KD mice with respect to control mice (KD: 7.2 ± 0.6; CD: 5.1 ± 0.32) (Fig. 24A). We further investigated the phenotype of glioma-associated astrocytes, isolating them from the ipsilateral hemisphere of CD and KD mice. Quantitative real-time PCR showed that most of the pro-inflammatory signature genes analyzed (*C3*, *Amigo2*, *Srgn*, *Serping1*, *and Cd44*), exhibit increased levels of expression in KD mice with respect to CD mice (Fig. 24B) and only *S100a10* transcript is upregulated among the anti-inflammatory selected genes (Fig. 24C). Moreover, by immunofluorescence staining, we further validate the increased C3 expression in peritumoral astrocytes of KD mice with respect to CD mice (KD: 15.35 ± 0.95, CD: 9,36 ± 0.78) (Fig. 24D).

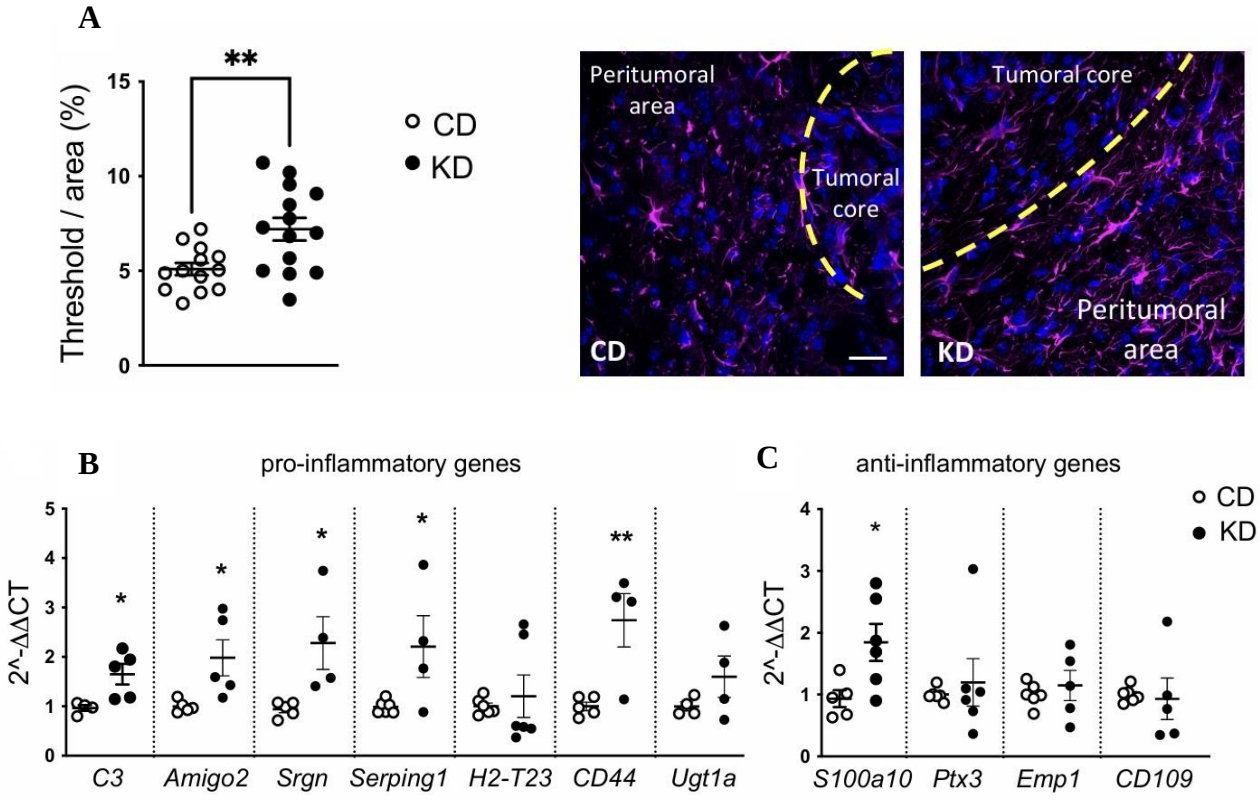

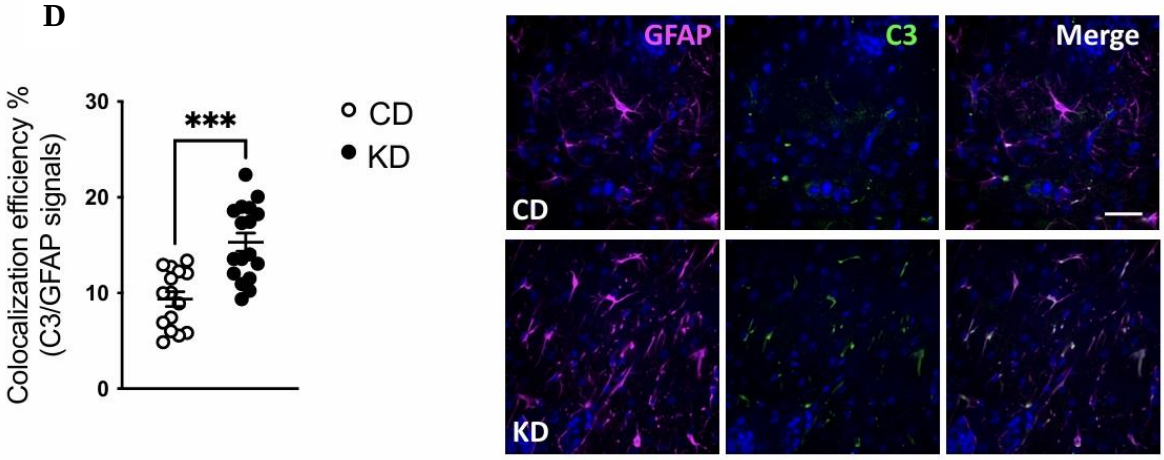

Figure 24: (A) Scatter dot plots showing quantification of GFAP$^+$ signal expressed as the percentual area occupied by fluorescent staining in CD (n=13/3 slices/mice) and KD (n=14/3 slices/mice) mice. Data are presented as the mean ± SEM **p <0.005, Student's t-test. Left: Representative z-projection confocal images of GFAP (magenta) in CD and KD tumoral and peritumoral area. Hoechst staining (blu) for nuclei visualization Scale bar: 50 μm. **(B)** RT-qPCR from ACSA$^+$ cells isolated from CD and KD tumoral hemisphere reveals expression of pro-inflammatory genes and **(C)** anti-inflammatory genes. Gene expression is normalized to the housekeeping gene Gapdh. Data are presented as the mean ± SEM n = 4 to 6 mice pulled from two independent experiments. ** p <0.01; *p <0.05, Student's t-test. **(D)** Scatter dot plots showing the percentual area of GFAP signal colocalizing with C3 staining (Ctrl n=15/3 slices/mice; KD n=17/3 slices/mice) Data are presented as the mean ± SEM *** p <0.001, Student's t-test. Left: Representative z-projection confocal images of GFAP (magenta) and C3 (green) colocalization in CD and KD peritumor area. Hoechst staining (blu) for nuclei visualization Scale bar: 50 μm.

We confirmed the increased transcription level of pro-inflammatory genes upon β-HB stimulation in primary astrocytes (Fig. 25A). None of the tested anti-inflammatory genes are modulated upon β-HB treatment and, notably, the GCM can polarize the astrocyte towards an anti-inflammatory phenotype, as shown by the significantly increased expression level of *S100a10*, *Ptx3*, and *Emp1* transcript (Fig. 25B). We tested also the microglia/macrophage phenotype by isolating the CD11b$^+$ cells from the ipsilateral hemisphere of CD and KD mice. Quantitative real-time PCR showed that most of the pro-inflammatory signature genes analyzed (Fig. 25C) are significantly upregulated except for *iNOS* whose expression is significantly reduced in parallel with the increased expression of *Arg1* and many other anti-inflammatory genes such as *Chil3*, *Cd206*, *Tgfβ* and *Il10* (Fig. 25D).

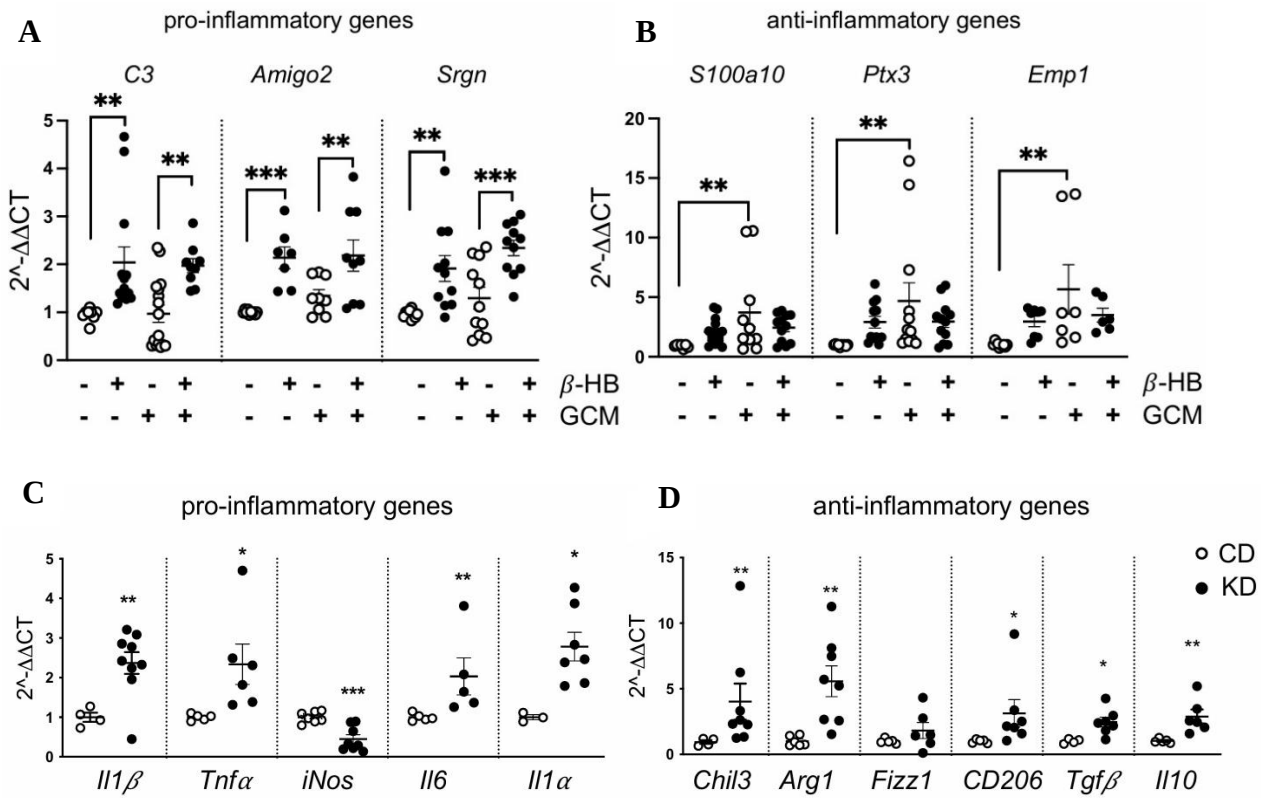

Figure 25: (A) RT-qPCR from astrocytes with or without β-HB and GCM administration showing the relative expression of pro-inflammatory and **(B)** anti-inflammatory genes. Gene expression is normalized to the housekeeping gene Gapdh. Data are presented as the mean ± SEM n = 7 to 16 mice pulled from 4 independent experiments. *** p <0.001** p <0.01; Two-way ANOVA, Fisher's LSD test. **(C)** RT-qPCR from $Cd11b^+$ cells isolated from CD and KD tumoral hemisphere reveals transcriptional expression levels of pro-inflammatory and (**D)** anti-inflammatory genes. Gene expression is normalized to the housekeeping gene Gapdh. Data are presented as the mean ± SEM n = 4 to 8 mice pulled from two independent experiments. ** p <0.01; *p <0.05, Student's t-test.

We further investigated the β-HB effect on primary microglia cells. Quantitative real-time PCR showed that β-HB is able to increase the transcriptional level of almost all the analyzed genes (Fig. 26A, B). Nevertheless, in the presence of the GCM, the pro-inflammatory genes *IL1β* and *iNOS* are not modulated while anti-inflammatory genes *Chil3* and *Arg1* are significantly up-regulated, thus suggesting that β-HB stimulated microglia acquire a more pronounced anti-inflammatory phenotype in the presence of GCM (Fig. 26B).

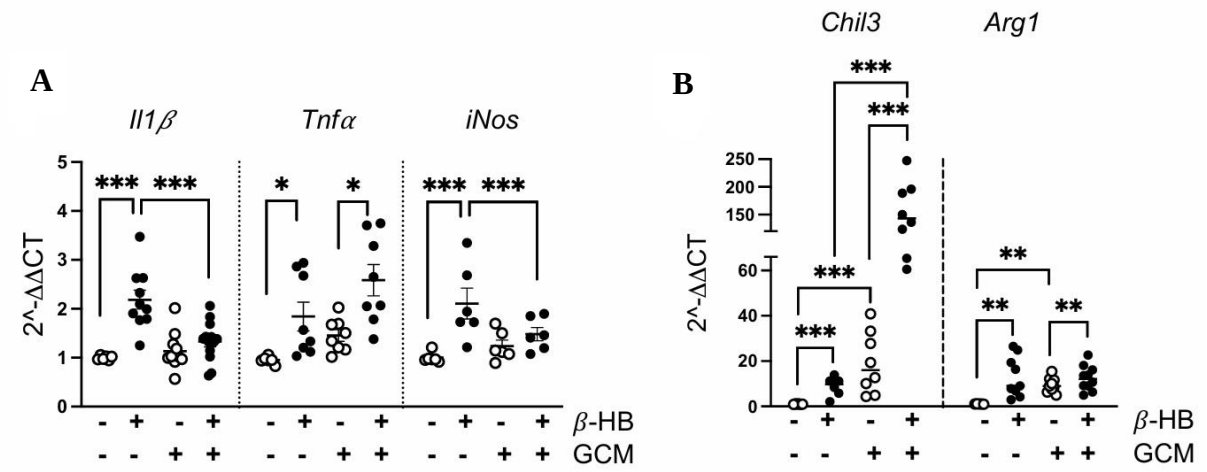

Figure 26: (A) RT-qPCR from primary microglia with or without β-HB and GCM administration showing the relative expression of pro-inflammatory and **(B)** anti-inflammatory genes. Gene expression is normalized to the housekeeping gene Gapdh. Data are presented as the mean ± SEM n = 4 to 9 samples pulled from 3 independent experiments. *** p <0.001** p <0.01 *p <0.05; Two-way ANOVA, Fisher's LSD test.

Altogether these data demonstrate that astrocytes, directly affected by the KD regimen, exert an anti-tumor function.

β-HB increases astrocytic glutamate uptake:

Since astrocytes can exert an antitumor effect by modulating glutamate levels in the tumor microenvironment, we analyzed the expression of glutamate transporters in astrocytes isolated from CD and KD mice. Quantitative real-time PCR showed that *Glast, Glt1* and *mGluR5* transcripts are upregulated in KD versus CD mice (Fig. 27A) and, *in vitro*, in GCM-primed astrocytes stimulated with β-HB (Fig. 27B). We further investigated the glutamate transporters functionality by analyzing the glutamate concentration in the astrocytic medium, showing a significant reduction in glutamate content upon β-HB treatment (astrocytes + GCM: 100 ± 5 nmol/mg; astrocytes + GCM + β-HB: 62 ± 12 nmol/mg) (Fig. 27C).

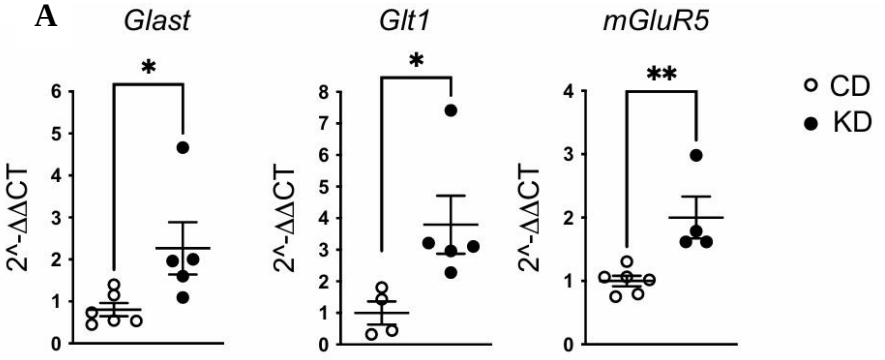

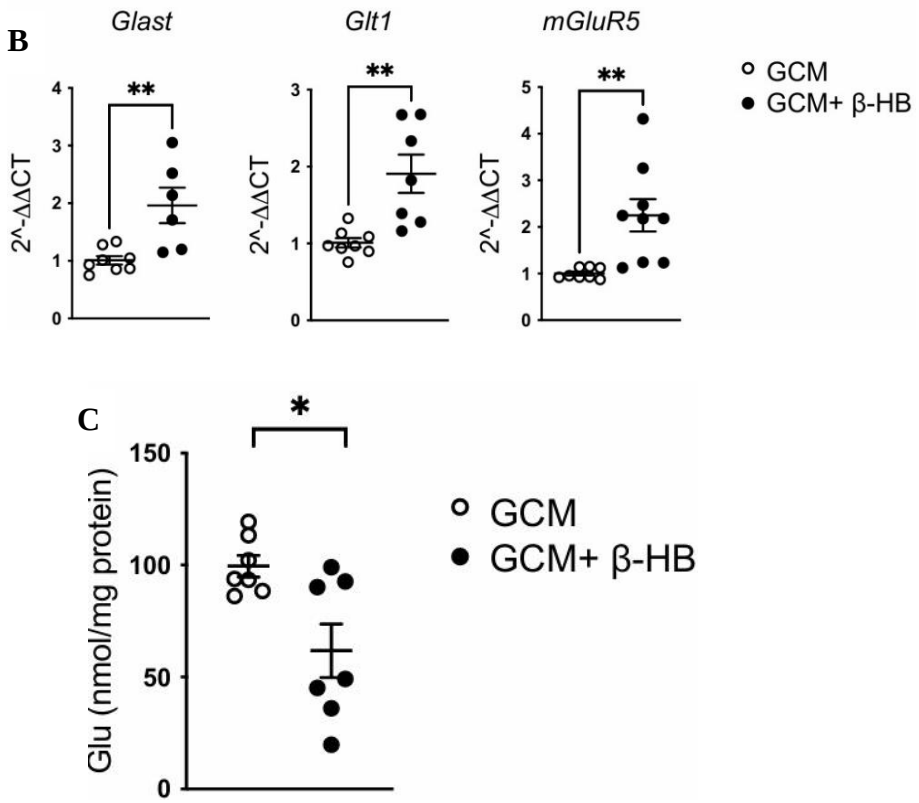

Figure 27: (A) RT-qPCR from ACSA^{+} cells isolated from CD and KD tumoral hemisphere reveals expression of glutamate transporters Glast, Glt1, and mGluR5 genes. Gene expression is normalized to the housekeeping gene Gapdh. Data are presented as the mean ± SEM n = 4 to 6 mice pulled from two independent experiments. ** p <0.01; *p <0.05, Student's t-test. **(B)** RT-qPCR from astrocytes cultured in GCM with or without β-HB administration showing the relative expression of glutamate transporters Glast, Glt1, and mGluR5 genes. Gene expression is normalized to the housekeeping gene Gapdh. Data are presented as the mean ± SEM n = 6 to 9 samples pulled from 3 independent experiments. ** p <0.01 Student's t-test. **(C)** Scatter dot plot showing the glutamate quantification in astrocytes cultured in GCM with or without β-HB. Data (nmol/mg of protein) are presented as the mean ± SEM n = 7 samples pulled from 3 independent experiments. * p <0.05 paired Student's t-test.

Pro-inflammatory astrocytes and β-HB slowdown GL261 proliferation and increase the basal intracellular Ca^{2+} levels:

To test whether β-HB treated astrocytes can counteract GL261 growth, we co-cultured astrocytes with glioma on a transwell® system and measured GL261 proliferation. The presence of astrocytes significantly reduced the GL261 proliferation rate and β-HB was able to further slowdown the in vitro glioma cell proliferation (Fig. 28A). We tested also the effect of microglia on GL261 proliferation: microglia-conditioned media (MCM) reduced the GL261 proliferation rate, but the effect could not be ascribed to β-HB (Fig. 28B).

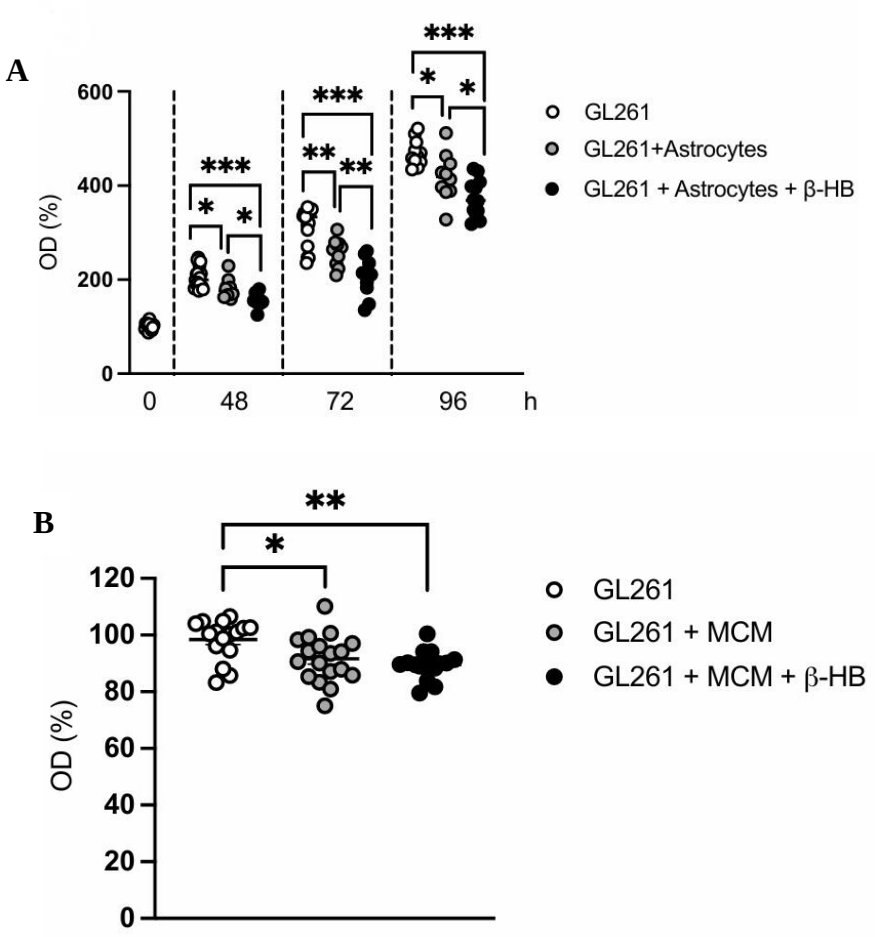

Figure 28: (A) Scatter dot plot showing the MTT assay on GL261 cells co-cultured with astrocytes and β-HB. Data are presented as the mean ± SEM n = 10 to 18 samples pulled from 3 independent experiments. *** p <0.001** p <0.01 *p <0.05; One-way ANOVA, Tukey's multiple comparison test. **(B)** Scatter dot plot showing the MTT assay on GL261 cells in the presence of MCM and β-HB. Data are presented as the mean ± SEM n = 16 to 18 samples pulled from 3 independent experiments. ** p <0.01 *p <0.05; One-way ANOVA, Tukey's multiple comparison test.

The presence of β-HB in the co-culture of GL261 cells and astrocytes changes their relative proportion: after 48 of co-culture in the presence of β-HB, the mixed $GL261^{rfp}$/astrocytes co-cultures showed a reduced percentage of $GL261^{rfp}$ and an increased percentage of astrocytes (Fig. 29A). Further evidence of the effect of β-HB-treated astrocytes on glioma cells came from the fluoresce-based analysis of intracellular free Ca^{2+} concentration ($[Ca^{2+}]_i$): β-HB produced a small but significant increase in the basal $[Ca^{2+}]_i$ of $GL261^{rfp}$ in monoculture. When glioma cells were co-cultured with astrocytes we measured a larger increase in $GL261^{rfp}$ basal $[Ca^{2+}]_i$, and this effect was further enhanced in the presence of β-HB (Fig. 29B left). β-HB increased basal $[Ca^{2+}]_i$ also in astrocyte monocultures (Fig. 29B right). Furthermore, astrocytes enhanced

the frequency of spontaneous Ca^{2+} transients in $GL261^{rfp}$, an effect strongly inhibited by β-HB treatment (Fig. 29C left panel). The same β-HB effect was also observed in astrocyte monoculture (Fig. 29C right panel), suggesting that spontaneous Ca^{2+} of astrocytes might regulate the same activity in GL261 cells. Taken together these data indicate that β-HB-treated astrocytes can modulate the Ca^{2+} homeostasis of GL261 cells.

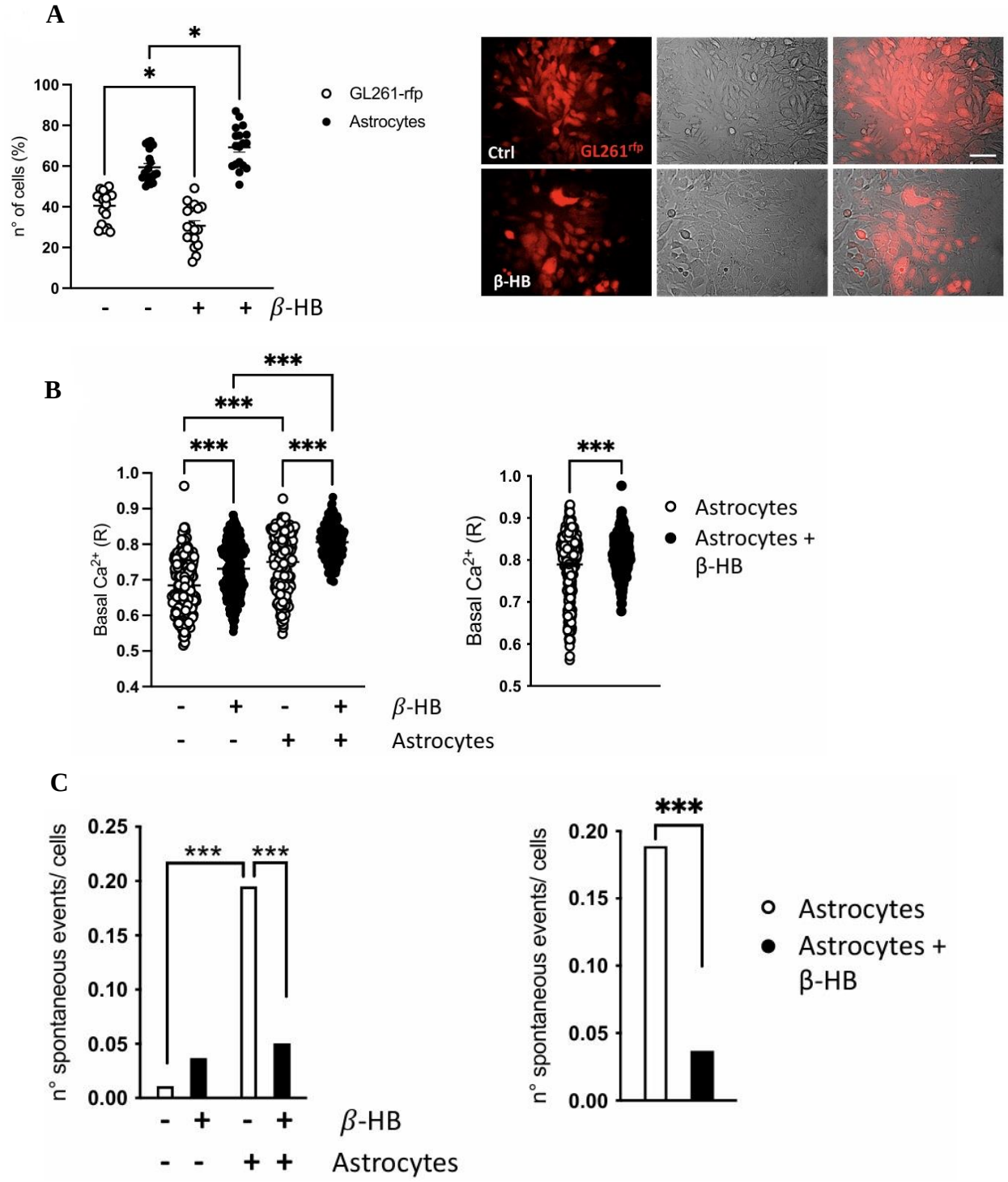

Figure 29: (A) Scatter dot plot showing the percentage of $GL261^{rfp}$ and astrocytes cultured with or without β-HB. Bottom panel: representative immunofluorescence pictures of the direct

co-culture between GL26^{rfp} and astrocytes (identified by phase contrast microscope acquisitions, scale bar: 50 μm). Data are presented as the mean ± SEM n = 18-19 analyzed fields of view pulled from n=3 independent experiments. *** p <0.001, *p <0.05; Two-way ANOVA, Fisher's LSD test. **(B)** Left panel: Scatter dot plot showing the effect of β-HB and astrocytes on the basal Ca^{2+} level of GL261^{rfp}. Data are presented as the mean ± SEM n = 178-260 cells analyzed from 3 independent experiments. *** p <0.001; Two-way ANOVA, Fisher's LSD test. Right panel) Scatter dot plot showing the basal Ca^{2+} level of astrocytes co-cultured with GL261^{rfp} and stimulated with β-HB. **(C)** Left panel: Bar graph showing the number of spontaneous events recorded in GL261^{rfp} co-cultured or not with astrocytes, with or without β-HB stimulation. (*** p<0.001) Right panel: Bar graph showing the number of spontaneous events recorded in astrocytes co-cultured with GL261^{rfp} and stimulated with β-HB. (*** p<0.001)

Discussion

In the last decade, the ketogenic diet represented a novel adjuvant approach to standard glioma treatment by targeting the altered metabolism characteristic of cancer cells.

While preclinical studies and some clinical case reports have shown promising results for the use of KD in glioma treatment, the effects on cancer and brain cells are still largely unknown. In addition to the complexities surrounding the metabolic interactions within glioma cells, the pieces of information regarding the role of glial cells in the context of the KD and its potential therapeutic effects are missing. Glial cells play critical roles in maintaining brain homeostasis and responding to pathological conditions such as cancer [73], influencing tumor progression and treatment responses through various mechanisms, including the immune-metabolic crosstalk and the remodeling of tumor microenvironment [74].

Here, we investigated how a restricted KD in adult mice can reduce tumor growth and increase mice survival. These data are in line with several research papers showing the efficacy of the KD in counteracting glioma growth [75]. We explored the role exerted by β-HB, the major ketone body produced during ketosis, in glioma-bearing mice. The reduced tumor volume observed in these mice not only reveals that β-HB is a potent mediator of KD but also poses it as a putative alternative to this restrictive diet, often poorly tolerated by patients.

Because glioma cells are not able to utilize ketone bodies for energy production, and since the peritumoral area, as part of the brain parenchyma after surgical resection, is the real target of adjuvant therapies, it is important to deepen our knowledge in the cellular and molecular mechanism of tumor-glia interplay.

Here we investigated the potential role played by glial cells in counteracting glioma progression upon KD or β-HB treatment on mice and β-HB in vitro administration. We first showed that GL261 cell proliferation is not affected by β-HB treatment and that these cells are not consuming the ketone bodies in vitro, evidence supported by the increased concentration of β-HB in the tumor tissue of KD mice. On the contrary, both astrocytes and microglial consume β-HB, which also differently promotes their metabolic reprogramming [76].

In addition to the effect on cellular metabolism, KD metabolic products can influence many different cellular functions such as gene expression, oxidative stress, and inflammation in physiological and pathological conditions.

We investigated the effect of KD and β-HB on the tumor-associated glial cells, describing the phenotype acquired by astrocytes and microglia. It has been reported that astrocytes surrounding gliomas upregulate GFAP expression and that tumor-associated astrocytes and

microglia acquire an anti-inflammatory/pro-tumoral state [65]. We characterized the transcriptional changes of the signature genes representative of pro-inflammatory and anti-inflammatory glial cells isolated from the tumoral hemisphere of KD respect to CD mice. Astrocytes isolated from the tumoral hemisphere of glioma-bearing mice revealed that KD up-regulated almost all the tested pro-inflammatory genes, together with C3, particularly enriched in inflammatory astrocytes [77].

We further showed the in vitro effect of β-HB on astrocytes, switching the anti-inflammatory phenotype induced by the presence of GCM towards a pro-inflammatory phenotype. This effect, mediated by the KD and its metabolic product, further underlines that tumor-associated anti-inflammatory astrocytes aid the evolution of an immunosuppressive environment in glioblastoma and that tumor-associated pro-inflammatory astrocytes are effective in counteracting glioma growth.

A crucial role of inflammatory mediators in glioma biology has been described for TNFα. In addition to TNFα, also microglial derived IL1α has been proposed as a potent inducer of pro-inflammatory astrocytes. In line with this evidence, we reported that the $CD11b^+$ cells isolated from KD mice exhibit increased levels of pro-inflammatory mediators potentially involved in the induction of pro-inflammatory astrocytes.

Although it has been shown that β-HB and the shift of microglial glucose metabolism from glycolysis to oxidative phosphorylation is associated with an anti-inflammatory phenotype, in glioma-bearing mice, the microglia/macrophages cell profiling reveals that KD is inducing a mixed activation state that is not ascribed to the classical pro-inflammatory or anti-inflammatory classification.

Glial cells play important roles during brain tumor progression influencing cancer invasion, aggressiveness, and resistance to therapies. In particular, peritumoral astrocytes balance the glutamate extracellular concentration thus orchestrating the peritumoral neuronal hyperexcitability and excitotoxic death [78].

Considering the beneficial effect mediated by the KD, we further investigated the functional role of astrocytes in buffering extracellular glutamate in the tumor microenvironment. We report an increased expression of the metabotropic glutamate receptor mGluR5 and of the glutamate transporters Glt-1 and Glast, which tightly regulate the concentration of the excitatory neurotransmitter in the extracellular space. Moreover, we observed that astrocytes, in the presence of β-HB, are functionally active in reducing the extracellular glutamate content. These data support the ability of KD to decrease neuronal hyperexcitability by acting on

various targets and suggest a commitment of peritumoral astrocytes to a neuroprotective effect on brain parenchyma.

To investigate the potential involvement of pro-inflammatory astrocytes in reducing tumor growth, taking advantage of a co-culture system, we observed that astrocytes mediate a reduction in glioma proliferation and that the presence of β-HB further enhances this effect. This supports the notion that astrocytes surrounding glioma can restrain tumor proliferation and that increased tumor cell apoptosis could be induced also by increasing astrocytes glutamate uptake capability.

In co-culture experiments, we observed an astrocyte-driven reduction in glioma proliferation along with an increase in GL261 basal $[Ca^{2+}]_{I,}$ and these effects were further increased by β-HB. β-HB-treated astrocytes dysregulate Ca^{2+} homeostasis of glioma cells, likely leading to glioma cell dysfunction, potentially linked to the observed inhibition of tumor growth [79].

In conclusion, we demonstrated that KD and β-HB induce a pro-inflammatory phenotype of glioma microenvironment reducing tumor cell proliferation, increasing intracellular basal Ca^{2+} level, and promoting neuroprotection by reducing the extracellular glutamate level.

Materials and methods

Animal husbandry

C57BL/6N mice were housed (two to four animals for each cage) under a 12-h light cycle in standard cages and fed ad libitum with a standard diet (4RF21 Mucedola s.r.l.). They were randomly allocated to the different experimental groups. All the experiments in this study were conducted seeing the ARRIVE guidelines [80], and were authorized by the local animal welfare body and by the Italian Ministry of Health (authorization No. 231/2015PR) following the EC Council Directive 2010/63/EU and the Italian d.lgs.26/2014. All the efforts were done to reduce animal suffering, and to reduce the number of animals, estimating the necessary sample size before starting the experiments.

Tumor Cell implantation and Diet composition and Administration

Glioma syngeneic mouse models (GM) are obtained by injecting glioma cells (GL261) 1×10^5 cells at 2 mm lateral, 1 mm anterior to the bregma, and 3 mm depth in the right striatum. Two days after tumor implantation, the mice are randomly assigned to two groups, the control group and the treated group (KD), and start to be fed two different diets (Mucedola s.r.l.) for three weeks after tumor implantation. The ketogenic diet and the relative control diet composition are reported in Table 4. The KD diet has a caloric density of 6,73 Kcal/gr and each animal was fed with 1-3 gr/day. The body weight is constantly monitored throughout the experimental setup to avoid a weight loss of 10-15% higher than the starting point of treatment. Control mice received an isocaloric amount of food compared to the ketogenic diet. For survival analysis glioma injected mice were daily monitored and the endpoints were determined by lack of physical activity or 20% weight loss. The mean survival time was calculated using the Kaplan–Meier method and statistical analysis was performed using a log-rank test.

Table 4. Diet composition and analytical components

Ctrl Diet (93M)	Ketogenic diet (93M-PF4590)
Composition: Maize starch, maltodextrin, casein, sucrose, hydrogenated vegetable fats (Crisco), corn oil, bicalcium phosphate, calcium carbonate, sodium chloride, potassium sulfate, magnesium oxide.	Composition: Hydrogenated vegetable fats (Crisco), casein, cocoa butter, corn oil, bicalcium phosphate, calcium carbonate, sodium chloride, potassium sulfate, magnesium oxide.

Analyticalcomponents:		Analyticalcomponents:	
Carbohydrates:		Carbohydrates:	
Form starch and sucrose	63%	Form starch and sucrose	0%
From cellulose	5%	From cellulose	6%
Crude protein	8,9%	Crude protein	15,9%
Crude oils and fats	5,10%	Crude oils and fats	67,7%
Crude fibers	3,5%	Crude fibers	4,5%
Crude ash	2,5%	Crude ash	4%
Antioxidants:		Antioxidants:	
t-butylhydroqinone	70mg	t-butylhydroqinone	130mg
Nutritional additives:		Nutritional additives:	
Vitamin A	U.I.6000	Vitamin A	U.I.10800
Vitamin D3	U.I.1500	Vitamin D3	U.I.2700
Fe	mg 40,3	Fe	mg 72,6
Mn	mg 10,5	Mn	mg 19,0
Zn	mg 33,5	Zn	mg 60,3
Cu	mg 6,0	Cu	mg 10,8
I	mg 0,21	I	mg 2,37
Se	mg 0,15	Se	mg 0,27
Mo	mg 0,15	Mo	mg 0,27

In-vivo β-HB administration

Two days after tumor implantation, the mice are intraperitoneally injected with 50 ul of saline or β-HB (120mg/kg; Fisher Scientific 150-83-4), every other day. Three weeks after tumor implantation mice are sacrificed and brains are analyzed for tumor volume evaluation. During the entire experiment mice are fed ad libitum with a standard diet.

Tumor volume evaluation

Sequential 20 μm coronal brain slices (one each 100 μm of the entire tumor length) were collected and stained by standard H&E protocol. Tumor volume was calculated via the formula (volume = $t \times \sum A$), where A is the tumor area/slice and t is the thickness by ImageTool3.0 software.

Isolation of mouse astrocytes, CD11b$^+$ cells, and RNA extraction

Glioma-bearing mice were anesthetized and perfused with PBS. Brains were removed, the tumor portion is isolated from the ipsilateral hemisphere and a single-cell suspension was obtained in Hank's balanced salt solution (HBSS) by mechanical dissociation using a glass wide-tipped pipette. The cell suspension was applied to a 30 µm cell strainer (Miltenyi Biotec). Cells were processed instantly for MACS MicroBead separation. ACSA2$^+$ cells or CD11b$^+$ cells were magnetically labeled with the respective MicroBeads (Miltenyi Biotec 130097678; 130049601). The cell suspension was loaded onto a MACS Column placed in the magnetic field of a MACS Separator and the negative fraction was collected. After removing the magnetic field, ACSA2$^+$ and CD11b$^+$ cells were eluted as a positive fraction. Total RNA was isolated with Tri-Reagent (Merck), and processed for real-time PCR. The quality and yield of RNAs were verified using the NANODROP One system (Thermo Scientific).

Immunofluorescence staining on brain tissue and image acquisition

By using 3% isofluorane mice were anesthetized and perfused transcardially with cold PBS and 4% PFA in 0.1 M PB. Brains were quickly removed, stayed overnight in PFA 4%, washed with PB, and cryoprotected in PB 30% sucrose solution. We then collected 20 µm- thick coronal sections by using cryostat microtome (Leica Microsystems) at 20°C. Briefly, slices were immersed for 30 min in a boiling citrate buffer solution for antigen retrieval, then incubated with blocking solution (0.5% Triton X-100, 5% BSA) for 1h at RT. Sections were incubated with primary antibodies (Ki67 M3063 SP6 clone Spring Bioscience 1:50; 1:100; GFAP MAB30060 Millipore 1:200; C3 A0063 Dako 1:50) in diluted blocking solution overnight at 4 °C and 1 h at RT with fluorophore-conjugated secondary antibodies (Alexa Fluor 594 goat anti-rat) and Hoechst for nuclei visualization. The sections were mounted with a fluorescence mounting medium (DAKO) or with a ProLong Glass Antifade Mountant (Thermo Fisher).

Images were collected with spinning disk confocal microscopy on an Olympus IX73 microscope equipped with X-Light V3 spinning disk (CrestOptics), LDI laser source, and a Prime BSI Scientific CMOS (sCMOS), 6.5 µm pixels (Photometrics) with a 60x/1.4 PlanApo l oil objective and 10x objectives. The Z step size was 1 µm and 0.5 µm respectively for 10X and 60X objectives. All the images were acquired by using Metamorph software version 7.10.2. (Molecular Devices, Wokingham, UK) and then analyzed with ImageJ or Metamorph software.

Cell lines and primary glial culture

Glioma cells GL261, and CT2-a are maintained in DEMEM 20% FBS and DMEM 10% FBS respectively. Cortical primary glial cells were prepared from 0- to 2-d-old mice: cerebral cortices were chopped and digested in 30 U/ml papain for 40 min at 37°C followed by gentle trituration. The dissociated cells were washed, suspended in DMEM with 10% FBS (Invitrogen) and 2 mM L-glutamine, and plated at a density of 9–10 x 10^5 in 175 cm2 cell culture flasks. At confluence (10 –14 DIV), glial cells were shaken for 2 h at 37°C to detach and collect microglia and astrocyte cells. After seeding, cells were cultured in DMEM low glucose (D6064, Sigma-Aldrich) treated for the indicated time point with β-HB (Sigma Aldrich, H6501, 10mM) in the presence of a glioma-conditioned medium (GCM), or co-cultured with GL261 cells. In co-culture experiments, GL261 cells (1,5x10^4 cells) were seeded in the lower compartment of a 24-well transwell® system (Sigma Aldrich, 3413, 0.4µm pore size) containing astrocytes (3x10^4 cells). For direct co-culture, GL261 RFP cells (1,5x10^4) were mixed with astrocytes (3x10^4 cells), and seeded on tissue culture dishes (Corning Falcon, 353001, 35mm). In all these experiments β-HB is administered at a final concentration of 10 mM.

Conditioned medium preparation

GCM is collected from GL261 (1x10^6 cells in 1 ml of DMEM -FBS). Microglia cells were also treated with β-HB (10mM) in the presence of a glioma-conditioned medium (GCM) and microglia-conditioned medium (MCM) was also collected (2x10^4 cells in 1 ml of DMEM -FBS).

Glucose and β-HB Measurement

The evaluation is performed through a detection device (Wellion-Galileo) that uses strips for the detection of glucose and β-HB in blood and from GL261, microglia, and astrocyte cell medium treated with β-HB.

MTT assay

MTT assays have been performed on: GL261 murine glioma and CT2a cells treated with different concentrations of β-HB, GL261 cells co-cultured with astrocytes or in the presence of microglia-conditioned media (MCM), astrocytes and microglia alone or in the presence of GCM. After being treated with β-HB (10mM) for 24, 48h, 72h, and 96h, as specified for each experiment, MTT (dissolved in PBS with a final density of 0.5 mg/ml) was added to the

medium culture. After 90 min incubation, the MTT solution was extracted, mixed with DMSO, and shaken for 20 min. Finally, the absorption of the samples was read by regulating the 570-nanometer filter as the main wavelength and the 630-nanometer filter as the referenced wavelength. Blank was subtracted from all samples to obtain pure cellular absorption.

Real-time PCR

Samples were lysed in TRYzol reagent to isolate total RNA. The quality and yield of RNAs were verified using NANODROP One (Thermo Scientific). For RT-PCR one microgram of total RNA was reverse transcribed by using ThermoScript RT-PCR System. RT-PCR was carried out using Sybr Green (Bio-Rad) according to the manufacturer's instructions. The PCR protocol consisted of 40 cycles of denaturation at 95◦C for 30s and annealing/extension at 60◦C for 30s. For quantification, the comparative Threshold Cycle (Ct) method was used. The Ct values from each gene were standardized to the Ct value of GAPDH in the same RNA samples. Relative quantification was performed using the $2^{-\Delta\Delta Ct}$ method and expressed as fold change in arbitrary values. The Ct values for the housekeeping gene did not vary between the control (20.6 ± 0.2) and treated groups (20.4 ± 0.3), it confirms that the housekeeping gene's expression is not influenced by the treatment or experimental condition. Oligos used for gene expression are listed in Table 5.

Table 5- List of oligoes

GAPDH_forward	TCG TCC CGT AGA CAA AAT GG
GAPDH_reverse	TTG AGG TCA ATG AAG GGG TC
AMIGO2_forward	GAGGCGACCATAATGTCGTT
AMIGO2_reverse	GCATCCAACAGTCCGATTCT
Arg-1_forward	CTCCAAGCCAAAGTCCTTAGAG
Arg-1_reverse	AGGAGCTGTCATTAGGGACATC
BDH1_forward	GCTTCCTTGTATTTGCTGGC
BDH1_reverse	TTCTCCACCTCTTCACTGTTG
BDH2_forward	CAAAGCATTCCTTCCCAAAA
BDH2_reverse	ATGCCCTGTTGGATGAAGTC
CD109_forward	CACAGTCGGGAGCCCTAAAG
CD109_reverse	GCAGCGATTTCGATGTCCAC
C3_forward	AGCAGG TCATCAAGTCAGGC
C3_reverse	GATGTAGCTGGTGTTGGGCT
Emp1_forward	GAGACACTGGCCAGAAAAGC
Emp1_reverse	TAAAAGGCAAGGGAATGCAC
FIZZ1_forward	CCCCTTCTCCAGCTGATCAA
FIZZ1_reverse	GAACATCCCACGAACCACAG
H2-T23_forward	GGACCGCGAATGACATAGC
H2-T23_reverse	GCACCTCAGGGTGACTTCAT

IL-1β_forward	GCAACTGTTCCTGAACTCAACT
IL-1β_reverse	ATCTTTTGGGGTCCGTCAACT
IL6_forward	AGTCCTGATCCAGTTCCTGC
IL6_reverse	CTACATTTGCCGAAGAGCCC
IL10_forward	GTTCTTTGGGGAGCCAACAG
IL10_reverse	GCTCCCTGGTTTCTCTTCCT
iNOS_forward	ACATCGACCCGTCCACAGTAT
iNOS_reverse	CAGAGGGGTAGGCTTGTCTC
MCT2_forward	GTTTGCTCGGCCTTCTGTAG
MCT2_reverse	TCCAAATCCCAATCCAAAAA
MCT4_forward	ACGGCTGGTTTCATAACAGG
MCT4_reverse	CCAATGGCACTGGAGAACTT
OXCT1_forward	CTGCCTTCTACACCAGCACA
OXCT1_reverse	CATGCTTTCACCAGAGCAAA
Ptx3_forward	AACAAGCTCTGTTGCCCATT
Ptx3_reverse	TCCCAAATGGAACATTGGAT
SERPING1_forward	ACAGCCCCCTCTGAATTCTT
SERPING1_reverse	GGATGCTCTCCAAGTTGCTC
SRGN_forward	GCAAGGTTATCCTGCTCGGA
SRGN_reverse	TGGGAGGGCCGATGTTATTG
S100a10_forward	CCTCTGGCTGTGGACAAAAT
S100a10_reverse	CTGCTCACAAGAAGCAGTGG
TGFb_ forward	TTGCTTCAGCTCCACAGAGA
TGFb _ reverse	TGGTTGTAGAGGGCAAGGAC
TNF-α_forward	GTGGAACTGGCAGAAGAG
TNF-α_reverse	CCATAGAACTGATGAGAGG
YM-1_forward	CAGGTCTGGCAATTCTTCTGAA
YM-1_reverse	GTCTTGCTCATGTGTGTAAGTGA

Glutamate assay

Primary murine astrocytes were plated in 24-well plates (2×10^5 cells/well) and treated with GCM or with GCM + β-HB (10mM). After 72h, the cell medium was collected and centrifuged at 10 000 *g* x 15' to remove insoluble material. Glutamate concentration was measured by a colorimetric assay, according to the manufacturer's instructions (Sigma-Aldrich). The cells were lysed in RIPA buffer and the protein content of each well was quantified by BCA assay (Pierce) and used for normalization.

Calcium imaging

Changes in free intracellular Ca^{2+} concentration $[Ca^{2+}]_i$ was quantified by time-resolved digital fluorescence microscopy using the Ca^{2+} indicator Fura-2 (excitation 340 nm and 380 nm, emission 510 nm). The changes of $[Ca^{2+}]_i$ were expressed as $R=F_{340}/F_{380}$. GL261 and astrocyte cultures were incubated with the cell-permeant Fura-2 acetoxymethyl ester (2 μM; Molecular

probes, Life technologies) for 1 h at 37 ◦C in culture medium. Cells were then washed and placed in normal external solution (NES) for fluorescence microscopy experiments. $[Ca^{2+}]_i$ variations with $\Delta R>0.01$ were considered as spontaneous activity. Cells were continuously perfused during the experiment. $[Ca^{2+}]_i$ variations were measured separately from each individual cell, using the MetaFluor 7.0 software (Molecular Devices, USA). NES contained (in mM): 140 NaCl, 2.8 KCl, 2 CaCl2, 2 MgCl2, 10 glucose, and 10 HEPES; pH value adjusted with NaOH at 7.3.

Statistical analysis

The repeat (n) for each experiment and details of statistical analyses are described in the figure legends or main text. Data are reported as mean ± SEM. Statistical analysis, normality tests, and non-parametric tests were performed, when appropriate, with GraphPad Prism 9 software. The exact p-values are indicated in the text where available and the multiplicity-adjusted p-values are indicated in the corresponding figures (*$p < 0.05$, **$p < 0.01$, ***$p < 0.001$). Paired T-test is used to compare tumor volume and glutamate measurement, and an unpaired T-test is used for immunofluorescence analysis. For real-time PCR an unpaired T-test or a Two-way ANOVA, Fisher's LSD test was run to determine significant differences for the considered genes. For MTT assays a Mann–Whitney U test was run to determine significant differences for the considered experimental conditions.

Basal Ca^{2+} values were expressed as basal R values (means ± S.D.) and analyzed using one-way ANOVA test. When necessary, the non-parametric Dunn's one-way ANOVA on ranks was used. In case of significance, all pairwise multiple comparison procedure was used (Holm-Sidak, or Dunn's method for non-parametric tests). Responsive cells data were expressed as number of spontaneous events/cells. The minimum power of statistical tests was set at 0.8. The significance for all tests was set at $p < 0.05$.

Personal contribution to the project

To provide clarity, I'll summarize the details of my contribution to this project by categorizing all conceptual, experimental, and analytical tasks into two distinct levels, as follows:

I was the main contributor:

- Animal handling & feeding
- Tumor cell implantation & diet administration
- Intraperitoneal β-HB administration

- Tumor volume evalution
- RNA extraction
- Immunofluorescence staining on brain tissue
- Cell lines and primary glial culture
- MTT Assay
- Real time PCR

I collaborated on the tasks:

- Isolation of mouse astrocytes, $CD11b^+$ cells
- Image acquisition
- Glucose and β-HB Measurement
- Calcium imaging
- Glutamate Assay

References

1. Hernández A, Domènech M, Muñoz-Mármol AM, Carrato C, Balana C. Glioblastoma: Relationship between metabolism and immunosuppressive microenvironment. *Cells*. 2021;10(12). doi:10.3390/cells10123529
2. Kao TJ, Lin CL, Yang W Bin, Li HY, Hsu TI. Dysregulated lipid metabolism in TMZ-resistant glioblastoma: pathways, proteins, metabolites and therapeutic opportunities. *Lipids Health Dis*. 2023;22(1):1-13. doi:10.1186/s12944-023-01881-5
3. D'Alessandro G, Antonangeli F, Marrocco F, et al. Gut microbiota alterations affect glioma growth and innate immune cells involved in tumor immunosurveillance in mice. *Eur J Immunol*. 2020;50(5):705-711. doi:10.1002/eji.201948354
4. Virtuoso A, Giovannoni R, De Luca C, et al. The glioblastoma microenvironment: Morphology, metabolism, and molecular signature of glial dynamics to discover metabolic rewiring sequence. *Int J Mol Sci*. 2021;22(7):1-20. doi:10.3390/ijms22073301
5. Chu X, Tian W, Ning J, et al. *Cancer Stem Cells: Advances in Knowledge and Implications for Cancer Therapy*. Vol 9. Springer US; 2024. doi:10.1038/s41392-024-01851-y
6. Esemen Y, Awan M, Parwez R, et al. Molecular Pathogenesis of Glioblastoma in Adults and Future Perspectives : A Systematic Review. Published online 2022.
7. Mattei V, Santilli F, Martellucci S, et al. The Importance of Tumor Stem Cells in Glioblastoma Resistance to Therapy. Published online 2021.
8. Wang S, Yin F, Guo Z, et al. Association between gut microbiota and glioblastoma: a Mendelian randomization study. *Front Genet*. 2023;14(January):1-11. doi:10.3389/fgene.2023.1308263
9. Hou K, Wu ZX, Chen XY, et al. Microbiota in health and diseases. *Signal Transduct Target Ther*. 2022;7(1). doi:10.1038/s41392-022-00974-4
10. Cryan JF, O'riordan KJ, Cowan CSM, et al. The microbiota-gut-brain axis. *Physiol Rev*. 2019;99(4):1877-2013. doi:10.1152/physrev.00018.2018
11. Fröhlich EE, Farzi A, Mayerhofer R, et al. Cognitive impairment by antibiotic-induced gut dysbiosis: Analysis of gut microbiota-brain communication. *Brain Behav Immun*. 2016;56:140-155. doi:10.1016/j.bbi.2016.02.020
12. Woolf EC, Syed N, Scheck AC. Tumor metabolism, the ketogenic diet and β-hydroxybutyrate: Novel approaches to adjuvant brain tumor therapy. *Front Mol*

Neurosci. 2016;9(NOV2016):1-11. doi:10.3389/fnmol.2016.00122

13. Martuscello RT, Vedam-Mai V, McCarthy DJ, et al. A supplemented high-fat low-carbohydrate diet for the treatment of glioblastoma. *Clin Cancer Res*. 2016;22(10):2482-2495. doi:10.1158/1078-0432.CCR-15-0916
14. Jaraíz-Rodríguez M, del Prado L, Balsa E. Metabolic remodeling in astrocytes: Paving the path to brain tumor development. *Neurobiol Dis*. 2023;188(June):106327. doi:10.1016/j.nbd.2023.106327
15. Ahmed H, Leyrolle Q, Koistinen V, et al. Microbiota-derived metabolites as drivers of gut–brain communication. *Gut Microbes*. 2022;14(1). doi:10.1080/19490976.2022.2102878
16. Ma Q, Xing C, Long W, Wang HY, Liu Q, Wang R fu. Impact of microbiota on central nervous system and neurological diseases : the gut- brain axis. Published online 2019:1-14.
17. Carabotti M, Scirocco A, Maselli MA, Severi CT gut brain axis. interactions between enteric microbiota, central and enteric nervous systems. *Ann Gastroenterol*. 2015;28(2):203-209.
18. Cordella F, Sanchini C, Rosito M, et al. Antibiotics treatment modulates microglia–synapses interaction. *Cells*. 2021;10(10):1-19. doi:10.3390/cells10102648
19. Loh JS, Mak WQ, Tan LKS, et al. Microbiota–gut–brain axis and its therapeutic applications in neurodegenerative diseases. *Signal Transduct Target Ther*. 2024;9(1):29-39. doi:10.1038/s41392-024-01743-1
20. Zhang D, Jian YP, Zhang YN, et al. Short-chain fatty acids in diseases. *Cell Commun Signal*. 2023;21(1):1-20. doi:10.1186/s12964-023-01219-9
21. Bauermeister A, Mannochio-Russo H, Costa-Lotufo L V., Jarmusch AK, Dorrestein PC. Mass spectrometry-based metabolomics in microbiome investigations. *Nat Rev Microbiol*. 2022;20(3):143-160. doi:10.1038/s41579-021-00621-9
22. Castonguay-paradis S, Veilleux A. Allam-Ndoul_2020_gutmicrobiota and intestinal barrier.pdf. Published online 2020.
23. Jiang H, Zeng W, Zhang X, Pei Y, Zhang H, Li Y. The role of gut microbiota in patients with benign and malignant brain tumors: a pilot study. *Bioengineered*. 2022;13(3):7847-7859. doi:10.1080/21655979.2022.2049959
24. Prinz M, Jung S, Priller J. Microglia Biology: One Century of Evolving Concepts. *Cell*. 2019;179(2):292-311. doi:10.1016/j.cell.2019.08.053
25. Borst K, Dumas AA, Prinz M. Microglia: Immune and non-immune functions.

Immunity. 2021;54(10):2194-2208. doi:10.1016/j.immuni.2021.09.014

26. Erny D, de Angelis ALH, Jaitin D. et al., Host microbiota constantly control maturation and function of microglia in the CNS, Nat. *Neurosci*. 2015;18(7):965-977.
27. Rothhammer V, Borucki DM, Tjon EC, et al. Microglial control of astrocytes in response to microbial metabolites. *Nature*. 2018;557(7707):724-728. doi:10.1038/s41586-018-0119-x
28. Hambardzumyan D, Gutmann DH, Kettenmann H. The role of microglia and macrophages in glioma maintenance and progression. *Nat Neurosci*. 2015;19(1):20-27. doi:10.1038/nn.4185
29. Szulzewsky F, Pelz A, Feng X, et al. Glioma-associated microglia/macrophages display an expression profile different from M1 and M2 polarization and highly express Gpnmb and Spp1. *PLoS One*. 2015;10(2):1-27. doi:10.1371/journal.pone.0116644
30. Arcuri C, Fioretti B, Bianchi R, et al. Microglia-glioma cross-talk: A two way approach to new strategies against glioma. *Front Biosci - Landmark*. 2017;22(2):268-309. doi:10.2741/4486
31. Liu H, Sun Y, Zhang Q, et al. Pro-inflammatory and proliferative microglia drive progression of glioblastoma. *Cell Rep*. 2021;36(11):109718. doi:10.1016/j.celrep.2021.109718
32. Jiang Y, Zhao J, Xu J, et al. Glioblastoma-associated microglia-derived exosomal circKIF18A promotes angiogenesis by targeting FOXC2. *Oncogene*. 2022;41(26):3461-3473. doi:10.1038/s41388-022-02360-4
33. Hardee ME, Zagzag D. Mechanisms of glioma-associated neovascularization. *Am J Pathol*. 2012;181(4):1126-1141. doi:10.1016/j.ajpath.2012.06.030
34. Tabatabai G, Herrmann C, Von Kürthy G, et al. VEGF-dependent induction of CD62E on endothelial cells mediates glioma tropism of adult haematopoietic progenitor cells. *Brain*. 2008;131(10):2579-2595. doi:10.1093/brain/awn182
35. Tso CL, Shintaku P, Chen J, et al. Primary glioblastomas express mesenchymal stem-like properties. *Mol Cancer Res*. 2006;4(9):607-619. doi:10.1158/1541-7786.MCR-06-0005
36. Fang J, Lu Y, Zheng J, et al. Exploring the crosstalk between endothelial cells, immune cells, and immune checkpoints in the tumor microenvironment: new insights and therapeutic implications. *Cell Death Dis*. 2023;14(9). doi:10.1038/s41419-023-06119-x

37. Rosito M, Maqbool J, Reccagni A, et al. Antibiotics treatment promotes vasculogenesis in the brain of glioma-bearing mice. *Cell Death Dis*. 2024;15(3). doi:10.1038/s41419-024-06578-w
38. Garofalo S, Alessandra Porzia, Fabrizio Mainiero, Silvia Di Angelantonio, Barbara Cortese, Bernadette Basilico. Environmental stimuli shape microglial plasticity in glioma. *Elife*. 2017;6:1-28.
39. Mao J ming, Liu J, Guo G, Mao X gang, Li C xin. Glioblastoma vasculogenic mimicry: signaling pathways progression and potential anti-angiogenesis targets. *Biomark Res*. 2015;3(1):1-10. doi:10.1186/s40364-015-0034-3
40. Jain RK, Di Tomaso E, Duda DG, Loeffler JS, Sorensen AG, Batchelor TT. Angiogenesis in brain tumours. *Nat Rev Neurosci*. 2007;8(8):610-622. doi:10.1038/nrn2175
41. Ricci-Vitiani L, Pallini R, Biffoni M, et al. Tumour vascularization via endothelial differentiation of glioblastoma stem-like cells. *Nature*. 2010;468(7325):824-830. doi:10.1038/nature09557
42. Guo D, Murdoch CE, Xu H, et al. Vascular endothelial growth factor signaling requires glycine to promote angiogenesis. *Sci Rep*. 2017;7(1):1-10. doi:10.1038/s41598-017-15246-3
43. Förstera B, Dzaye OD a., Winkelmann A, et al. Intracellular glycine receptor function facilitates glioma formation: In vivo. *J Cell Sci*. 2014;127(17):3687-3698. doi:10.1242/jcs.146662
44. Seano G, Jain RK. Vessel co-option in glioblastoma: emerging insights and opportunities. *Angiogenesis*. 2020;23(1):9-16. doi:10.1007/s10456-019-09691-z
45. Mou Y, Yue Z, Zhang H, et al. High quality in vitro expansion of human endothelial progenitor cells of human umbilical vein origin. *Int J Med Sci*. 2017;14(3):294-301. doi:10.7150/ijms.18137
46. Rosenbrock H, Desch M, Kleiner O, et al. Evaluation of Pharmacokinetics and Pharmacodynamics of BI 425809, a Novel GlyT1 Inhibitor: Translational Studies. *Clin Transl Sci*. 2018;11(6):616-623. doi:10.1111/cts.12578
47. Cenit MC, Sanz Y, Codoñer-Franch P. Influence of gut microbiota on neuropsychiatric disorders. *World J Gastroenterol*. 2017;23(30):5486-5498. doi:10.3748/wjg.v23.i30.5486
48. Wang L, Zhang C, Zhang Z, et al. Specific clinical and immune features of CD68 in glioma via 1,024 samples. *Cancer Manag Res*. 2018;10:6409-6419.

doi:10.2147/CMAR.S183293

49. Haq RA, Schlachetzki JCM, Glass CK, Mazmanian SK. Microbiome – microglia connections via the gut – brain axis. 2018;216(1):41-59.
50. Wang R, Chadalavada K, Wilshire J, et al. Glioblastoma stem-like cells give rise to tumour endothelium. *Nature*. 2010;468(7325):829-835. doi:10.1038/nature09624
51. Lu IN, Dobersalske C, Rauschenbach L, et al. Tumor-associated hematopoietic stem and progenitor cells positively linked to glioblastoma progression. *Nat Commun*. 2021;12(1). doi:10.1038/s41467-021-23995-z
52. Scully S, Francescone R, Faibish M, et al. Transdifferentiation of glioblastoma stem-like cells into mural cells drives vasculogenic mimicry in glioblastomas. *J Neurosci*. 2012;32(37):12950-12960. doi:10.1523/JNEUROSCI.2017-12.2012
53. Pellegatta S, Poliani PL, Corno D, et al. Neurospheres enriched in cancer stem-like cells are highly effective in eliciting a dendritic cell-mediated immune response against malignant gliomas. *Cancer Res*. 2006;66(21):10247-10252. doi:10.1158/0008-5472.CAN-06-2048
54. Griveau A, Seano G, Shelton SJ, et al. A Glial Signature and Wnt7 Signaling Regulate Glioma-Vascular Interactions and Tumor Microenvironment. *Cancer Cell*. 2018;33(5):874-889.e7. doi:10.1016/j.ccell.2018.03.020
55. Nowak A, Grzegrzółka J, Kmiecik A, Piotrowska A, Matkowski R, Dzięgiel P. Role of nestin expression in angiogenesis and breast cancer progression. *Int J Oncol*. 2018;52(2):527-535. doi:10.3892/ijo.2017.4223
56. Pagani F, Paolicelli RC, Murana E, et al. Defective microglial development in the hippocampus of Cx3cr1 deficient mice. *Front Cell Neurosci*. 2015;9(March):1-14. doi:10.3389/fncel.2015.00111
57. Mukherjee P, Augur ZM, Li M, et al. Therapeutic benefit of combining calorie-restricted ketogenic diet and glutamine targeting in late-stage experimental glioblastoma. *Commun Biol*. 2019;2(1):1-14. doi:10.1038/s42003-019-0455-x
58. Elsakka AMA, Bary MA, Abdelzaher E, et al. Management of Glioblastoma Multiforme in a Patient Treated With Ketogenic Metabolic Therapy and Modified Standard of Care: A 24-Month Follow-Up. *Front Nutr*. 2018;5(March):1-11. doi:10.3389/fnut.2018.00020
59. Review AS. Effects of the Ketogenic Diet in the Treatment of Gliomas : A Systematic Review. Published online 2022:1-17.
60. Bello SD, Valdemarin F, Martinuzzi D, Filippi F, Gigli GL, Valente M. Ketogenic

Diet in the Treatment of Gliomas and Glioblastomas. Published online 2022:1-14.

61. Virtuoso A, Giovannoni R, Luca C De, et al. The Glioblastoma Microenvironment : Morphology , Metabolism , and Molecular Signature of Glial Dynamics to Discover Metabolic Rewiring Sequence. Published online 2021:1-13.
62. Thevenet J, De Marchi U, Domingo JS, et al. Medium-chain fatty acids inhibit mitochondrial metabolism in astrocytes promoting astrocyte-neuron lactate and ketone body shuttle systems. *FASEB J*. 2016;30(5):1913-1926. doi:https://doi.org/10.1096/fj.201500182
63. Beard E, Lengacher S, Dias S, Magistretti PJ, Finsterwald C. Astrocytes as Key Regulators of Brain Energy Metabolism: New Therapeutic Perspectives. *Front Physiol*. 2022;12(January). doi:10.3389/fphys.2021.825816
64. Thau-Zuchman O, Svendsen L, Dyall SC, et al. A new ketogenic formulation improves functional outcome and reduces tissue loss following traumatic brain injury in adult mice. *Theranostics*. 2020;11(1):346-360. doi:10.7150/thno.48995
65. Henrik Heiland D, Ravi VM, Behringer SP, et al. Tumor-associated reactive astrocytes aid the evolution of immunosuppressive environment in glioblastoma. *Nat Commun*. 2019;10(1). doi:10.1038/s41467-019-10493-6
66. Jurga AM, Paleczna M, Kadluczka J, Kuter KZ. Beyond the GFAP-astrocyte protein markers in the brain. *Biomolecules*. 2021;11(9). doi:10.3390/biom11091361
67. Sultana S, Sernett S, Bellin R, Robson R, Skalli O. Intermediate filament protein synemin is transiently expressed in a subset of astrocytes during development. *Glia*. 2000;30:143-153. doi:10.1002/(SICI)1098-1136(200004)30:23.0.CO;2-Z
68. Newman JC, Verdin E. β-Hydroxybutyrate: A Signaling Metabolite. *Annu Rev Nutr*. 2017;37:51-76. doi:10.1146/annurev-nutr-071816-064916
69. Shang S, Wang L, Lu X. β-Hydroxybutyrate enhances astrocyte glutamate uptake through EAAT1 expression regulation. *Mol Cell Neurosci*. 2024;131(August). doi:10.1016/j.mcn.2024.103959
70. Leite M, Frizzo JK, Nardin P, et al. β-Hydroxy-butyrate alters the extracellular content of S100B in astrocyte cultures. *Brain Res Bull*. 2004;64(2):139-143. doi:10.1016/j.brainresbull.2004.06.005
71. Dedkova EN, Blatter LA. Role of β-hydroxybutyrate, its polymer poly-β-hydroxybutyrate and inorganic polyphosphate in mammalian health and disease. *Front Physiol*. 2014;5 JUL(July):1-22. doi:10.3389/fphys.2014.00260
72. Perelroizen R, Philosof B, Budick-Harmelin N, et al. Astrocyte immunometabolic

regulation of the tumour microenvironment drives glioblastoma pathogenicity. *Brain*. 2022;145(9):3288-3307. doi:10.1093/brain/awac222

73. Lawrence JM, Schardien K, Wigdahl B, Nonnemacher MR. Roles of neuropathology-associated reactive astrocytes: a systematic review. *Acta Neuropathol Commun*. 2023;11(1):1-28. doi:10.1186/s40478-023-01526-9
74. Radin DP, Tsirka SE. Interactions between tumor cells, neurons, and microglia in the glioma microenvironment. *Int J Mol Sci*. 2020;21(22):1-17. doi:10.3390/ijms21228476
75. Abdelwahab MG, Fenton KE, Preul MC, et al. The ketogenic diet is an effective adjuvant to radiation therapy for the treatment of malignant glioma. *PLoS One*. 2012;7(5):1-7. doi:10.1371/journal.pone.0036197
76. Cells CG. [2 , 4- 13 C] b -hydroxybutyrate Metabolism in Astrocytes. 2011;(123):1566-1573. doi:10.1007/s11064-011-0485-3
77. Guttenplan KA, Weigel MK, Prakash P, et al. Neurotoxic reactive astrocytes induce cell death via saturated lipids. *Nature*. 2021;599(7883):102-107. doi:10.1038/s41586-021-03960-y
78. Villeneuve J, Tremblay P, Vallières L. Tumor necrosis factor reduces brain tumor growth by enhancing macrophage recruitment and microcyst formation. *Cancer Res*. 2005;65(9):3928-3936. doi:10.1158/0008-5472.CAN-04-3612
79. Osswald M, Jung E, Sahm F, et al. Brain tumour cells interconnect to a functional and resistant network. *Nature*. 2015;528(7580):93-98. doi:10.1038/nature16071
80. Kilkenny C, Browne WJ, Cuthill IC, Emerson M, Altman DG. Improving bioscience research reporting: The ARRIVE guidelines for reporting animal research. *J Pharmacol Pharmacother*. 2010;1(2):94-99. doi:10.4103/0976-500X.72351